Low Voltage Large Stroke Bipolar Tri-electrode Electrostatic Actuator for Deformable Mirrors in Adaptive Optics

by

Mohammadmehdi Allameh

A Thesis submitted to the Faculty of Graduate Studies
of
The University of Manitoba

In partial fulfilment of the requirement of the degree of

DOCTOR OF PHILOSOPHY

Department of Electrical and Computer Engineering
University of Manitoba
Winnipeg, MB

Low Voltage Large Stroke Bipolar Tri-electrode Electrostatic Actuator for Deformable Mirrors in Adaptive Optics

Mohammadmehdi Allameh

2023

Abstract

Image distortion is one of the most common problems of optical receivers. Adaptive Optics (AO) technology was invented to solve that issue for ground-based telescopes. The deformable mirror (DM) is the corrector which is being used to correct the aberrated received image in an AO system. The arrays of actuators and the flexible mirror face sheet are the two main elements of a DM.

In this thesis, a tri-electrode electrostatic actuator was studied which is comprised of one moving MEMS electrode and two fixed controlling electrodes. The actuator is primarily beneficial for usage in an array of actuators for DMs, since only one common high-voltage electrode is employed as the background electrode for all actuators in the array, and the movement of each individual actuator can be controlled by an individual low voltage electrode. The tri-electrode topology, and the additionally presented extended electrode tri-electrode configurations, are designed such that they can be utilized for other applications such as MEMS switches.

In this work, all the design parameters of the tri-electrode actuator were studied in simulation using the finite element method and restoring spring force method, as well as experimentally. The design studies were dimensionless. Therefore, the optimizations can be used for an actuator of any size. The studies showed that the controlling voltage of the actuator can be decreased significantly. For one specific design, it was shown that the controlling voltage is almost four times smaller than for a conventional parallel plate electrostatic actuator. The maximum displacement of the actuator can be enhanced significantly compared to that of the conventional configuration. The increased range of motion can be bidirectional, and for one specific case it was 2.5 times larger than for the conventional actuator using the extended electrode design. Two silicon MEMS actuators were

designed in order to experimentally verify the simulation studies. The measurements showed a close agreement between the simulations and the demonstrated prototype designs.

Secondary research was also performed to study the issues in building a tri-layer flexible mirror that can be utilized as the face sheet for DMs. The conducted stress analysis investigations result in valuable conclusions and a fabrication recipe was developed to enable tensile stress mirrors. The recipe was used to build tensile stress metal-polymer-metal tri-layer structures to enable wrinkle free mirrors, and a high level of smoothness as it is necessary for a flexible mirror face sheet.

Acknowledgements

First and foremost, I would like to express my whole-hearted gratitude to my advisor Dr. Cyrus Shafai for his outstanding and unforgettable guidance and enthusiasm for this academic endeavour. I appreciate his endless support and patience. It has been an honour and privilege to work under and learn from him not only as an intelligent scientist but also as a true teacher. Thank you.

I would like to appreciate my committee members Dr. Arkady Major and Dr. Gerald Gwinner for their valuable knowledge, comments, and encouragement during the course of this thesis.

I would like to thank Dr. Douglas Thomson for his helpful advice and the great course that he offered. I learned a lot from him.

Special Thanks go to Dr. Byoungyoul Park for his support and advice during my Ph.D. He was always available and thanks for the valuable feedback received.

I'm very thankful to Dwayne Chrusch helped me in the cleanroom and for teaching me the technical skills and his guidance and valuable ideas in microfabrication.

I would like to express my appreciation to my senior group members, especially Dr. Tao Chen for his great technical guidance and kind advice.

Last but not least, I would like to thank my family, my wife, my parents and my brother, who stood by me during the long journey. Special appreciations go to them for their countless support.

Contents

List of Tables

List of Figures

Notations and Abbreviations

The abbreviations below are used in this thesis.

List	Descriptions
Al	Aluminum
AO	Adaptive Optics
BHF	Buffered Hydrofluoric
BMC	Boston Micromachines Corporation
CMOS	Complementary Metal Oxide Semiconductor
Cr	Chromium
Cu	Copper
DC	Direct Current
DI	Deionized
DM	Deformable Mirror
DRIE	Deep Reactive Ion Etch
FEM	Finite Element Method
FOM	Figure Of Merit
HB	Hard Bake
HF	Hydrofluoric acid
HI	High Impedance
HMDS	Hexamethyldisilane

HV	High Voltage
IC	Integrated Circuits
ICP	Inductively Coupled Plasma
IPA	Isopropyl alcohol
JPL	Jet Propulsion Laboratory
KOH	Potassium Hydroxide
LDMOS	Laterally Diffused Metal Oxide Semiconductor
MEMS	Micro-Electro-Mechanical Systems
MMAs	Micromirror Arrays
N_2	Nitrogen
NSFL	Nano System Fabrication Laboratory
PEB	Post Exposure Bake
PETS	Plasma Equipment Technology System
PolyMUMPS	Polysilicon Multi-user Micromachining Process
PR	Photoresist
PWM	Pulse Width Modulation
RF	Radio Frequency
RIE	Reactive Iron Etching
ROC	Radius Of Curvature
RSFM	Restoring Spring Force Method
SCCM	Standard Cubic Centimeter per Minute
SF_6	Sulfure Hexafluride
SOI	Silicon On Insulator

SU-8	A high contrast, epoxy-based photoresist designed for microfabrication
THT	Temperature Holding Time
UV	Ultraviolet
VLT	Very Large Telescope
XeF_2	Xenon Difluoride

1

Introduction

Contents

1.1 Background: Adaptive Optics

Adaptive Optics (AO) technology has been employed in various areas of vision science. However, it was used in astronomy for the first time. The earliest AO systems were built based on Babcock's idea [1] of compensating atmospheric turbulence [2]. An AO system consists of three main elements: a wavefront sensor, a wavefront corrector, and a wavefront control system. The wavefront sensor measures the detected wavefront, including its distortion [3]. The wavefront corrector, which can be a segmented mirror or a deformable mirror (DM), corrects the aberrated wavefront [4,5]. The aberration could be from atmospheric or non-atmospheric sources affecting the received wavefront at every moment [6]. Therefore, a rapid real-time controlling system is needed to compensate for the distortion, particularly in ground-based telescopes where atmospheric turbulence is the primary source of aberration. Specifically, the wind speed at a specific height is the main parameter that significantly influences the AO temporal response and turbulence strength [7]. The schematic of an AO system is illustrated in figure 1.1a [8].

The wavefront corrector is the key element in the AO systems. As the corrector, DMs are generally preferred due to the segmented mirrors' light loss and diffraction issues [9]. It should be considered that the DMs also have drawbacks, such as crosstalk between the adjacent actuators [10]. DM consists of two parts of a flexible mirror (mirror face sheet) and a collection of actuators. The actuators are in close contact with the mirror and are to control the deformation of the DM. The reflective bending face sheet can be made with flexible materials such as SU-8 negative photoresist to help make it easier to deform the mirror. A cross-section schematic of the DM is shown in figure 1.1b. Figure 1.2 shows the Neptune images taken by the VLT (very large telescope) telescope with and without using the AO system [11].

There are various types of primary conventional DM technologies, such as the stacked array DMs [12] or the voice coil actuators (figure 1.3a). However, the MEMS DMs (figure 1.3b) are more popular due to the miniaturization and their lower manufacturing costs using batch fabrication of the IC manufacturing [13].

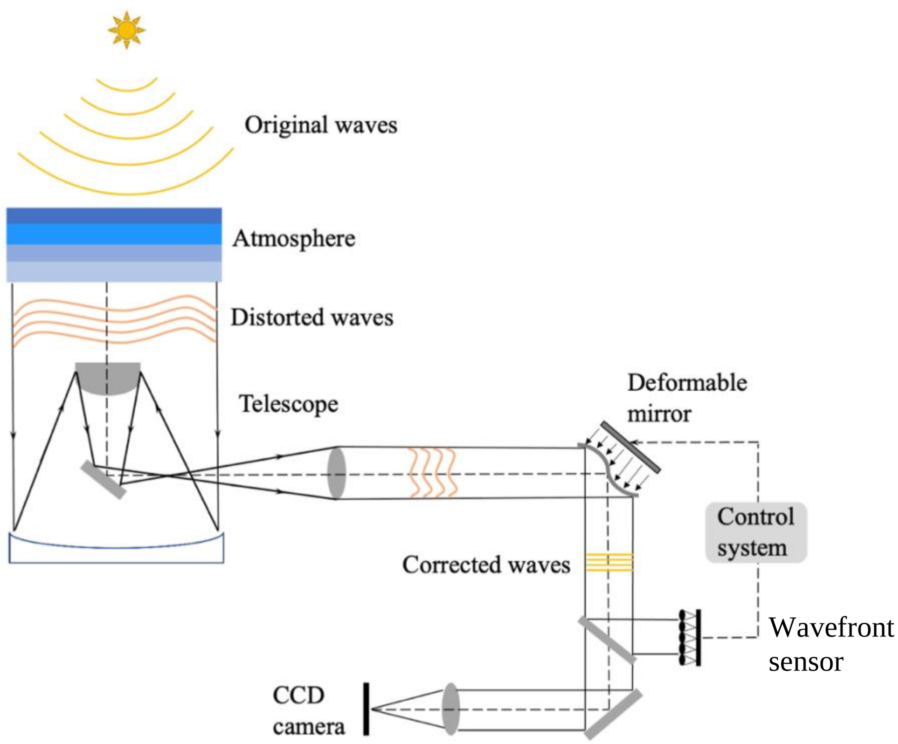

(a)

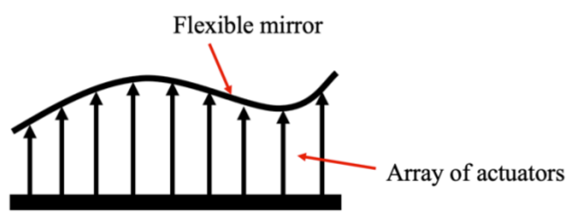

(b)

Figure 1.1. (a) Schematic of an AO system for ground-based telescopes. (b) Schematic of a DM composed of a flexible mirror and an array of actuators.

Figure 1.2. Neptune images were taken by the VLT telescope before and after correction using AO system. Reproduced from [P. Weilbacher "Neptune from the VLT with MUSE/GALACSI Narrow Field Mode adaptive optics," eso.org. https://www.eso.org/public/images/eso1824a (accessed Nov.30, 2022)].

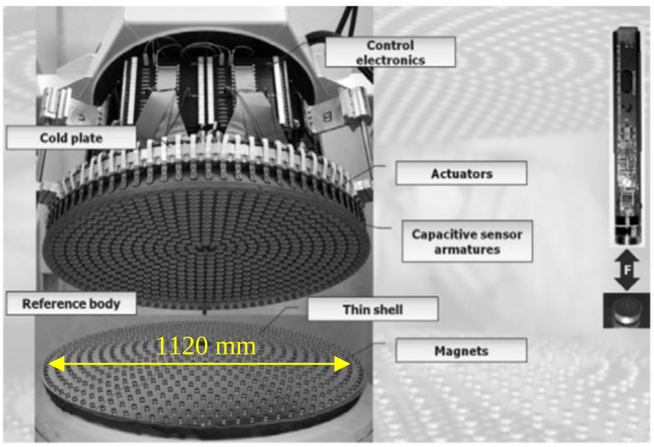

(a)

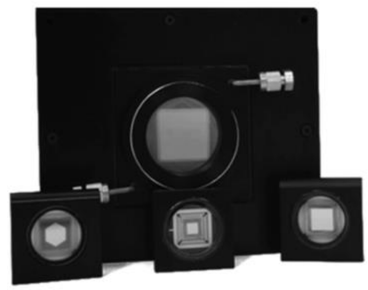

(b)

Figure 1.3. (a) Microgate and ADS conventional DM with 1172 voice coil actuators and 1120 mm diameter thin shell flexible mirror. (b) Boston Micromachines MEMS DM with different numbers of 140, 1020 and 4092 square and 331 segments HEX array actuators.Reproduced from [Y. P. Madec, "Overview of deformable mirror technologies for adaptive optics and astronomy," Proc. SPIE, vol. 8447, Sep. 2012, Art. no. 844705], with permission of SPIE.

1.2 Motivation

Most functional MEMS DMs use electromagnetic, piezoelectric, thermal, and electrostatic actuators. However, the usage of each technology for DMs can be highly dependent on the specific characteristics of the DM. For example, MEMS piezoelectric DMs have low current and power consumption, and a high enough deflection range, but batch fabrication of piezoelectric material can be expensive and less common as compared to an electrostatic actuator. The thermal actuators require high electric power, and their switching speed is lower than of the electrostatic actuators. Electromagnetic actuators have a high switching speed (high frequency). However, their power consumption is still higher than the electrostatic actuators due to their need of a steady state current.

Comparing all the mentioned actuators that are used for manufacturing the DMs, the electrostatic actuators have low power consumption and simple fabrication which is more compatible with the existing batch fabrication micromachining methods. Therefore, the electrostatic actuator was selected to study as the appropriate actuator for developing a DM.

Iris AO is one of the leading companies building DMs with electrostatic actuators. They have been successful in developing electrostatic actuator DMs with a displacement range of almost 3.5-7.5 µm for a voltage range of around 60-130 V [14-17]. However, the DM is designed based on using segmented mirrors which comes with limitations such as diffraction as compared to a DM with a continuous mirror face sheet. Furthermore, the displacement range is not significant compared to the relatively high controlling voltage. Meng-Ju Lin et al. designed and tested an electrostatic actuator DM using bulk micromachining. The DM consists of two top and bottom silicon substrates attached together via SU-8. The experiments showed that the mirror displacement is about 2.5 µm for an excitation voltage of 55 V [18]. Eui-Hyeok (EH) Yang et al. introduced a 4 × 4 array of electrostatic actuators for DMs. The actuator membrane was developed at NASA Jet Propulsion Laboratory (JPL) using membrane transfer technology. The DM was designed for a large and lightweight segmented space telescope to operate in visible and near-IR spectrum. The maximum displacement of the DM was about 0.37 µm and the exciting voltage was as high as 55 V [19]. Weimin Wang et al. designed and fabricated a 45-element continuous face sheet DM using PolyMUMPS (polysilicon multi-user micromachining process). In this DM, 45 electrostatic actuators were utilized to deform the flexible face sheet and correct the received distorted images. The experiments showed that each actuator can travel about 0.6 µm requiring an excitation voltage of almost 15 V [20]. OKO technologies company designed and built different DMs including an electrostatically actuated DM with 37 actuators [21,22]. The DM was manufactured using bulk micromachining consisting of a silicon nitride continuous membrane coated with Al. The continuous layer was suspended over a silicon substrate. The maximum displacement at the center of the mirror was 9 µm while each actuator required an excitation voltage as high as 260 V. Boston Micromachines Corporation (BMC) is another famous company that has pioneered the use of electrostatic actuators for commercialized DMs. The company used surface micromachining to manufacture thousands of polysilicon double cantilever actuators for their DMs. Each actuator is attached to the continuous face sheet mirror via a small attachment post. In a BMC 12 × 12 actuator array DM, the actuators could reach the maximum deflection of 2.5 µm by applying a minimum excitation voltage of 267 V [23].

Looking at the aforementioned electrostatically actuated DMs, we see that the high control/exciting voltage is a serious problem even for commercialized DMs. The deflection range is also an issue, as for a higher displacement range, a higher controlling voltage is required. Therefore, the primary purpose of this project was to develop a low-voltage electrostatic actuator with an enhanced travel range to be used for DMs. As the high voltage and limited deflection range are the two basic issues of the electrostatic actuators, the low-voltage electrostatic actuator presented in this thesis can also be employed for other applications, such as micro switches. Therefore, other electrostatic actuator applications are investigated in chapter 2.

The tri-electrode actuator configuration introduced for the first time by Yu Zhou [24,25] can enable a longer controllable travel range compared to conventional parallel plate electrostatic actuators, while offering a greatly reduced control voltage. This topology employs a novel electrostatic actuator configuration to reduce the actuator varying voltage. However, the studies regarding the actuator’s performance were limited, and many aspects of the actuator's behaviour were not looked at. As shown in figure 1.4, the tri-electrode actuator consists of one moving

MEMS electrode (cyan), one fixed perforated “intermediate” electrode underneath, and a third fixed “primary” electrode placed under the middle electrode. It was shown that this topology improves the actuator performance according to the intermediate electrode’s modulation of the primary electrode’s electric field, and also due to the fact that the intermediate electrode’s effective area reduces as the MEMS electrode approaches, essentially providing a negative feedback effect. However, the impact of the design parameters (such as the spacing between electrodes, or the size of electrodes and perforations in the intermediate electrode) and the effect of one parameter on another were not studied.

The design parameters of the various elements in the tri-electrode actuator are interrelated, and each one affects another. Therefore, each parameter must be studied separately, which was not considered in the previous work. Also, the represented studies highly depend on the moving MEMS electrode design, which limits the results to a specific technique, while it is desired to find a more generalized solution. For example, the interaction between the springs supporting the moving MEMS platform and the underlying electrodes can affect the pulling force. Also, the extended underlying electrode fringing fields (which can couple to the top side of the MEMS platform and the supporting springs) will have an effect on the electrostatic pulling forces and may alter the performance. However, in this work, each design parameter of the tri-electrode actuator topology was studied independently. Studies were performed in order to understand their individual performance characteristics. FEM analysis alongside the restoring spring force methods was used to achieve higher accuracy in simulations, in comparison to solving partial differential equations of multiple physics using COMSOL Multiphysics.

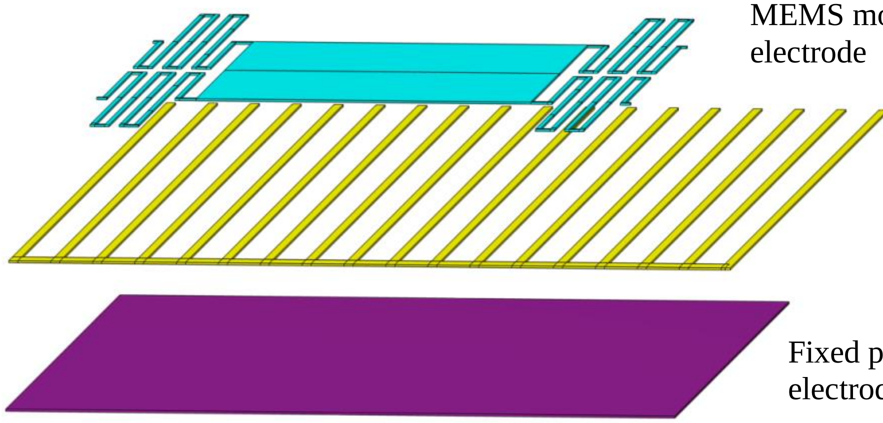

Figure 1.4. Schematic of the tri-electrode topology including two fixed electrodes and one moving electrode.

The goal of this thesis was to study the design parameters appropriate for the highest-performing tri-electrode electrostatic actuator for DM and array-based applications. The research included the study (through simulation) of the impact of each geometric feature parameter for the most optimum device performance. It also included the fabrication of prototype actuators to test and validate the simulation studies.

This research also included the development and thermal stress analysis of a tri-layer flexible mirror face sheet which can be utilized for DMs. This mirror was designed and developed by Byounyoul Park, a fellow member of our research group [26]. SU-8 was used as the flexible material of the face sheet as compared to the common stiffer materials already used in other work such as silicon and silicon nitride. Xiao-Hui Xu et al. utilized SOI silicon as the flexible face sheet along with piezo-electric actuators [27]. However, silicon's Young’s modulus is relatively high and may affect the overall stiffness of the DM resulting in a higher controlling voltage. A highly flexible mirror face sheet would additionally help in reducing the needed actuation voltage for the electrostatic actuator. One solution is using a softer material such as polymers. Po-Yu Lin et al. used polyimide polymer as the structural flexible layer of the mirror face sheet [28]. However, SU-

8 can be a better polymer in terms of its flexibility having a lower Young's modulus of around 2-3 GPa compared to the polyamide used in this work (PI-2610). The Young's modulus of polyamide is almost 8.5 GPa [29]. Therefore, SU-8 might be a better material for building a more flexible mirror face sheet. However, the early SU-8 manufactured face sheet explored by B. Park [26] had a series of issues such as non-flatness and undesired wrinkles. Therefore, in this thesis stress material analysis studies were performed to develop a fabrication process that will enable a mirror phase sheet with a flat surface.

Experimental testing:

The schematic of the designed tri-electrode used in this work for experimental testing is illustrated in figure 1.5. As shown, the tri-electrode consists of one moving MEMS platform and two stationary controlling intermediate and primary electrodes. The intermediate electrode is at a closer distance with respect to the moving MEMS electrode as compared to the lower primary electrode. The lower primary electrode is designed to provide a background electric field, that is modulated by the electric field generated by the perforated intermediate electrode. With this set of electrode configurations, the displacement of the MEMS electrode can be controlled with a smaller voltage range of the intermediate electrode. The lower controlling voltage is in comparison to a conventional parallel plate electrostatic actuator which has only one solid electrode below the MEMS electrode that is used to control the actuator displacement, when considered at the same distance of the perforated intermediate electrode of the tri-electrode configuration.

Two tri-electrode MEMS actuators (with square and narrow rectangular platforms) were designed and fabricated to experimentally test the tri-electrode actuator performance. The moving MEMS electrodes are shown in figures 1.6a (square) and 1.6b (rectangular). The intermediate and primary electrodes of both square and narrow rectangular actuators are displayed in figures 1.6c and 1.6d. The electrodes are coated on both sides of a quartz substrate. The quartz was used as a spacer material between the stationary electrodes to simplify the fabrication. The tri-electrode actuator (with square moving platform) after attaching all the electrodes is shown in figure 1.6e. The complete process of design and fabrication of the two actuators are reported in chapter 4.

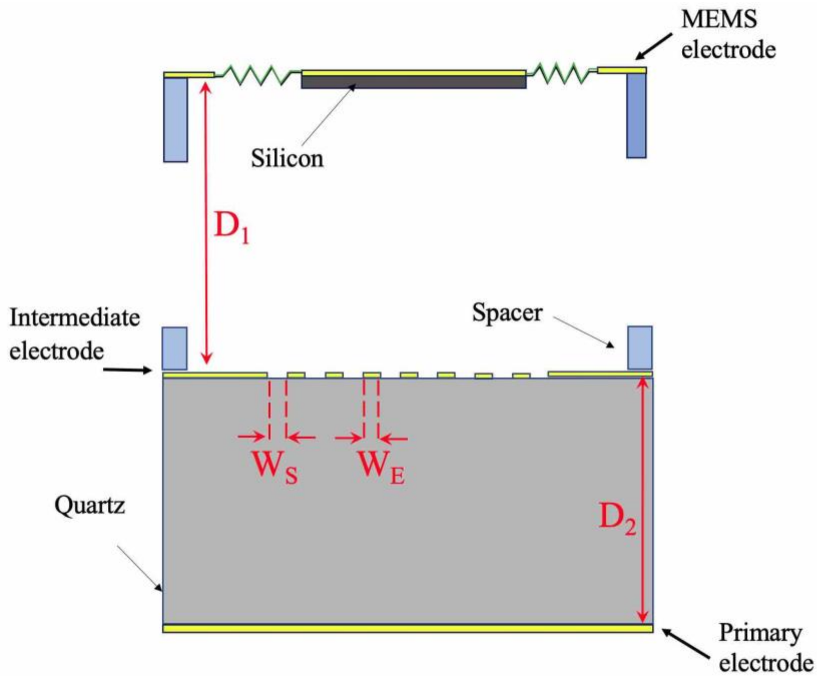

Figure 1.5. Schematic of a tri-electrode actuator.

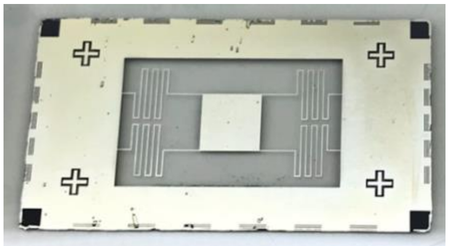

(a)

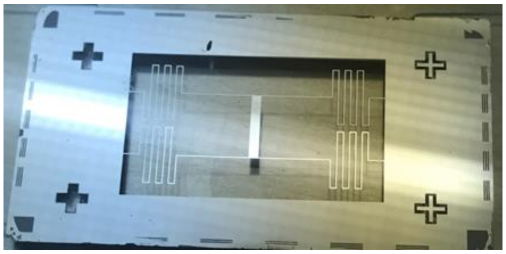

(b)

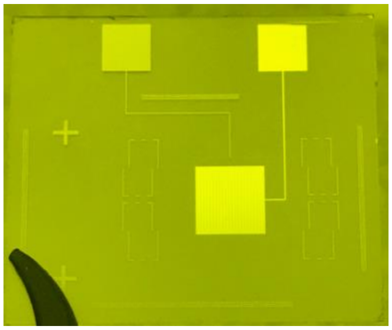

(c)

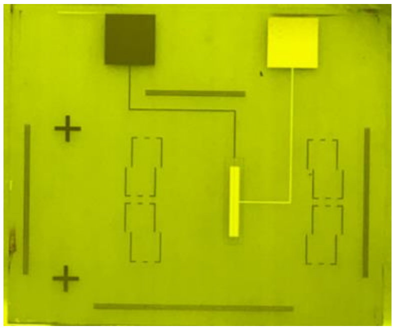

(d)

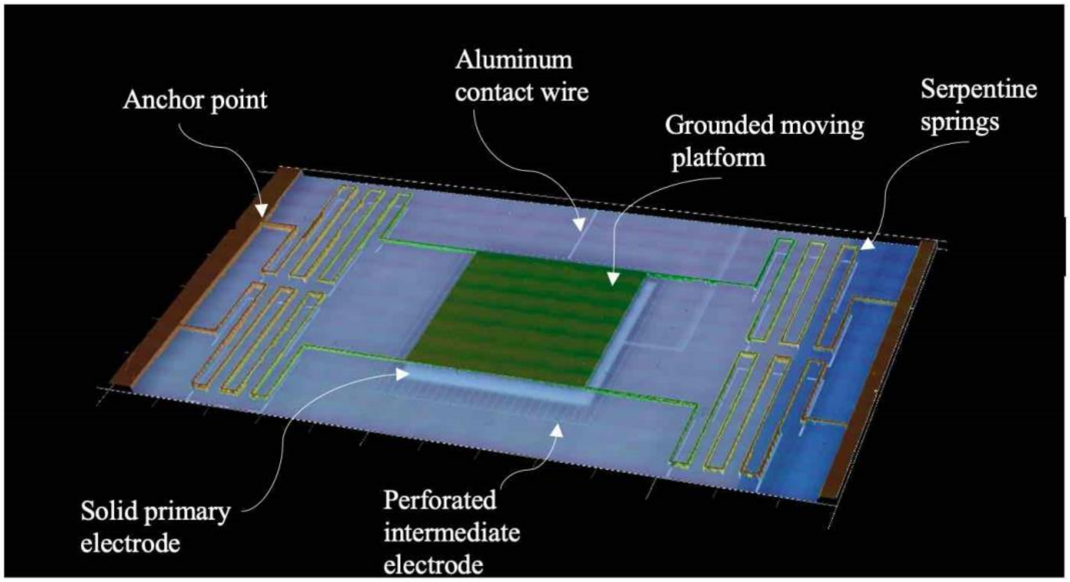

(e)

Figure 1.6.(a) Silicon MEMS moving electrode with the square suspended platform. (b) Silicon MEMS moving electrode with the narrow rectangular suspended platform. (c), (d) Fixed perforated and solid electrodes coated on quartz substrates. (e) Assembled silicon and quartz substrates to form the tri-electrode actuator.

1.3 Research Contributions

The contributions reported here include the results of the studies of the tri-electrode electrostatic actuator for array applications and particularly for DMs, including design, analysis, fabrication, and test experiments as explained in detail as follows:

- Exploration of how the tri-electrode actuator design parameters affect its performance, with the goal to find optimized designs to enable minimum controlling voltage and the highest control movement range. Studies included analysis of the effects of primary background voltage, gap spacing between electrodes, and intermediate electrode sizes and perforation spacings.
- Developing the restoring spring force method to study the tri-electrode electrostatic actuator. The method was employed to extract the response curves of the tri-electrode actuator models under various situations at different boundary conditions, and near the snap-down point of the actuator. The method was utilized along with FEM analysis solving partial differential equations. For this study, a 2D unit-cell model was developed employing the symmetric tri-electrode configuration to increase the accuracy of the analysis and reduce the time of convergence in FEM studies and simulations.
- Design and analysis of the extended electrode tri-electrode electrostatic actuator to enhance the range of motion and convert the unidirectional actuator to a bidirectional actuator. This bidirectional capability extends the applications where the tri-electrode topology can be employed.
- Study of the impact of using solid materials (other than air) as the spacer between the driving electrodes of the actuator. The use of solid materials helps significantly to simplify the

fabrication method of the actuator, and consequently, the actuator can be utilized for a higher number of applications.

- Design and fabrication of two MEMS actuators with square and narrow rectangular platforms of 6.7 × 6.7 mm^2 and 6.7 × 0.95 mm^2 as moving electrodes. They were designed to test the tri-electrode topology in different intermediate electrode gap spacings. The moving platforms were designed such that the springs saw the minimum electrostatic force from the underlying electrodes. The built tri-electrode actuators were utilized to demonstrate the performance of the tri-electrode actuator with intermediate gap spacings of 300 and 450 µm.
- Development of a low tensile stress tri-layer metal-polymer flexible mirror for use in DMs by Nanotechnology Research Centre, National Research Council of Canada (Edmonton). An issue with the polymer-based mirror is stress, and thermal stability, which can cause wrinkles (non-flat surface), in part due to the high-temperature steps during microfabrication. This study developed the microfabrication processes to minimize the residual stress, ensure thermal stability, and make the mirror flat enough to be able to be used in DMs.

1.4 Research Publications

The following publications are the results of the research of this thesis and a result of studying electrostatic actuators and flexible mirrors for the application of DMs.

1. **M. Allameh**, and C. Shafai, "Tri-electrode MEMS electrostatic actuator with lower control voltage and higher stroke for actuator array implementations,". Journal of Electrostatics, vol. 114, p. 103635, 2021.
2. **M. Allameh**, Y. Zhou, T. Chen, D. Chrusch, B. Park and C. Shafai, "Experimental analysis of a low controlling voltage tri-electrode MEMS electrostatic actuator for array applications," *J. Micromech. Microeng*, vol. 33, no. 3, p. 035008, 2023.
3. **M. Allameh**, B. Park and C. Shafai, "Enhanced travel range bipolar tri-electrode electrostatic actuator using extended background electrode," MOEMS and Miniaturized Systems XXI Conf. p. 120130, 2022.
4. **M. Allameh**, B. Park and C. Shafai, "Performance study of MEMS tri-electrode electrostatic actuator with glass and SU-8 between intermediate and primary electrodes," MNE euro-sensors conference, Leuven, 2022.
5. **M. Allameh**, S. Ramezanzadehyazdi, B. Park, C. Shafai, "Thermal Stress Analysis and Stabilization of Metal and SU-8 Coatings for Tri-Layer Mirror," IEEE Canadian Conf. on Elec. and Comp. Eng. 2021.

1.5 Thesis Overview

This thesis is organized into seven chapters, also including the appendices and the references.

Chapter 1

This chapter describes a brief background about the AO and the elements of the system to correct the received aberrated waveforms. It also includes the motivation of the thesis, contributions, and the list of publications.

Chapter 2

This chapter begins with the theory of electrostatic actuators and describes how they work according to the equilibrium between the attractive electrostatic and the restoring spring forces. Various applications of electrostatic actuators are introduced in this chapter and show how widely they can be utilized. Different approaches to solving the pull-in effect are reported according to the literature. Then, applications that use arrays of electrostatic actuators are represented, and their issues are briefly reported. Since electrostatic actuators require high voltage, a few most common methods to reduce the voltage are reported, and their limitations are briefly discussed.

Chapter 3

The developed restoring spring force method, which is used to analyze the tri-electrode topology, is described in this chapter. After introducing the tri-electrode actuator and all the controlling parameters, FEM analysis is used to study the performance of the actuator. Design parameters are studied and optimized based on the definitions. The impact of each parameter is investigated on the final response curve of the actuator. All the dimensions are normalized. Therefore, the results are dimensionless and generalized to be able to use in any design. The extended electrode design is also introduced, which is a new approach to extending the travel range of the tri-electrode actuator. Its design parameters are also studied, and the results are reported in this chapter. The impact of using different materials as a spacer is also investigated.

Chapter 4

Two MEMS moving electrodes which were designed to test the tri-electrode topology, are introduced in this chapter. Fabrication of the tri-electrode actuator is described in this chapter. Steps of building two tri-electrode actuators including mask preparation and the fabrication trials are reported. The trial and the corresponding solutions are very helpful for the future work of building arrays of the actuator for DMs.

Chapter 5

The experiment setup is presented in this chapter. The fabricated tri-electrode actuators with square and narrow rectangular shape platforms of 6.7 × 6.7 mm and 6.7 × 0.95 mm are tested and the results are reported here. The response curves of the built actuators are also plotted to compare the agreement between the numerical studies and the measurements.

Chapter 6

The experimental tests of a polymer-based tri-layer Metal/SU-8/Metal flexible mirror are presented in this chapter. The thermal stress analysis of that mirror with various metals are studied and the impact of different physical disposition method on the ultimate residual stress of the mirror are reported. The results of studies are valuable in the fabrication of a smooth and wrinkle-free flexible mirror of DMs.

Chapter 7

This chapter provides a summary of this thesis and the conclusions from the research. The future work is also described that can be performed as further research, which can be directed towards building an array of actuators.

2

Electrostatic Actuators: Background

Contents

2.1 Introduction

Micro-Electro-Mechanical Systems (MEMS) have been used in different areas to build sensors and actuators since the 1980s [30]. The traditional macroscale transducers have been replaced with micro-size devices for several purposes. This is due to the various advantages of miniaturization. The MEMS technology originated from the IC industry, and there has been many advanced studies on transduction mechanisms and micromachining processes for micro sensors and micro actuators [31]. Several studies on micro-size sensors and actuators showed that MEMS sensors can be superior to traditional ones in resolution and frequency while offering the special features of low-cost manufacturing and miniaturization packaging [32]. One breakthrough achievement of MEMS technology is the capability of integrating all sensors, actuators, signal processing, and power supplies on a single chip. Specifically, the MEMS actuators can be replaced with macro-size actuators for the same or in some case even a higher performance.

There are very different types of MEMS actuators depending on their applications and the purposes that they have been designed for. An actuator transforms a form of energy into mechanical movement. The commonly used MEMS actuators can be classified as magnetic, thermal, piezoelectric, and electrostatic. Magnetic actuators can have high speed, force, displacement, and low voltage, but the required power is not insignificant compared to an electrostatic actuator. Furthermore, it requires a relatively high external magnetic field, which is always a problem for on-chip integration and fabrication [33]. Thermal actuators do not need substantial voltages like electrostatics; however, they often require high-power dissipation and generally suffer from slower switching speeds due to thermal cooling speeds [34,35]. The piezoelectric actuators have low power dissipation and consumption and can be excited with low driving voltage at an acceptable high speed. However, these actuators employ nontrivial piezoelectric materials that are often not easily compatible with IC microfabrication. In comparison, electrostatic actuators have been one of the most common actuators used for on-chip integration due to their conventional materials [36]. They offer low-temperature operation, potential high-frequency operation, compact size, and generally easy fabrication. However, they can require high voltages for high-power and/or long-stroke applications. Therefore, studying their limitations is worthwhile.

2.2 Electrostatic actuator theory

An electrostatic actuator can be represented as two parallel electrodes as one of its simplest forms. The applied voltage across the electrodes controls the actuator displacement. A schematic of an electrostatic actuator with one fixed controlling voltage and one moving electrode is depicted in figure 2.1. The moving electrode is considered the MEMS element. The electrostatic force between the oppositely charged electrodes attracts the moving electrode toward the stationary electrode [37,38]. In this actuator, the two opposing forces control the actuator movements, one is the attractive electrostatic force (F_{es}) and the other is the spring force (F_{spring}) resisting the electrostatic force. The movement of the MEMS element is a result of overall opposing forces. Therefore, the movement starts when the attraction force overcomes the resisting spring force. The applied potential between the electrodes can vary according to the MEMS spring constant. The stiffer the spring, the higher voltage is required. However, if the spring performs in its linear range, the actuator spring constant effect can be easily predicted.

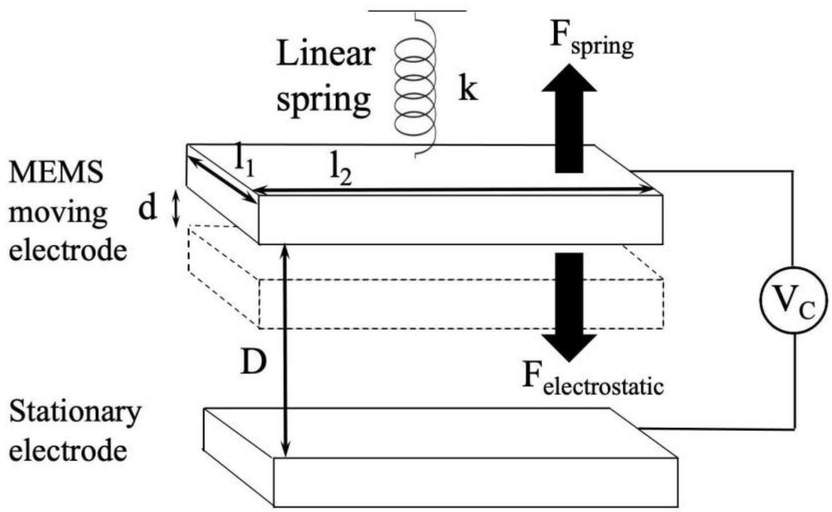

Figure 2.1. Conventional parallel plate electrostatic actuator schematic.

The capacitance between the electrodes is represented by $C = \frac{\varepsilon_0 l_1 l_2}{D-d}$ where $l_1 \times l_2$ is the area of each electrode, *D-d* is the distance between electrodes, and ε_0 is permittivity. The developed electrostatic force is the first derivative of the stored energy between the electrodes neglecting the fringing field [39] as shown in equation (2.1) below:

$$F_{es} = \frac{\partial w}{\partial x} = \frac{\partial}{\partial x}\left(\frac{1}{2} C V_C^2\right) = \frac{\partial}{\partial x}\left(\frac{1}{2}\frac{\varepsilon_0 l_1 l_2}{D-x} V_C^2\right)\Big|_{x=d} = -\frac{\varepsilon_0 l_1 l_2}{2}\left(\frac{V_C}{D-d}\right)^2, \tag{2.1}$$

where w is the energy stored between the electrodes, V_C is the voltage across the electrodes, l_1 and l_2 are the dimensions of the electrodes, *D* is the initial gap between the electrodes, and *d* is the travelled distance after applying V_C. Considering the moving MEMS electrode with linear spring constant, each time we apply the V_C potential across the electrodes, the MEMS element starts moving and stops when the generated electrostatic force becomes equal to the spring force (equilibrium). Thus, the amount of movement of the MEMS elements can be calculated by having the opposing forces equal, as shown below:

$$F_{es} = F_{spring}\,, \tag{2.2}$$

$$\frac{\varepsilon_0 l_1 l_2}{2}\left(\frac{V_C}{D-d}\right)^2 = -kd, \tag{2.3}$$

where k is the MEMS element spring constant. This equation is plotted in figure 2.2, and the performance of an electrostatic actuator is explained based on the curves in this figure.

As the MEMS displaces, the attractive force also increases. With sufficient displacement, no stable position of the MEMS may exist, and a snap-down of the MEMS to the other electrode can occur. The voltage at which that occurs (V_S) is the maximum possible voltage that can be applied to an electrostatic actuator while performing in a stable region, and for larger voltages, there is no equilibrium point. Figure 2.2 illustrates the motion of a simple electrostatic actuator. The red cross points in figure 2.2 are when restoring force, and electrostatic force is equal, and the moving MEMS electrode stop moving at these force equilibrium points. Electrostatic actuators perform in the stable region for the specific voltage range smaller than V_S. For the larger voltages, the electrostatic force overcomes the restoring force, and the MEMS moving electrode snaps down. The snap-down (pull-in) voltage which resulted from solving equation (2.3), is shown below, and depicted in figure 2.3. It is worth mentioning here that the displacement vs. voltage (d vs. V) part of the curve, for the values that the displacements are larger than snap-down (D_S), does not happen in practice and is only the mathematical representation of solving the equations. It is shown to display the turning point (snap-down) more clearly as

$$V_S = \frac{2}{3\sqrt{3}}\sqrt{\frac{2kD_S{}^3}{\varepsilon_0 l_1 l_2}}\,. \tag{2.4}$$

The turning point on the curve at voltage V_S is the snap-down point and represents the maximum displacement of the moving electrode before being unstable. It occurs at one-third of the initial gap size ($D_S = 1/3\ D$) between the electrodes.

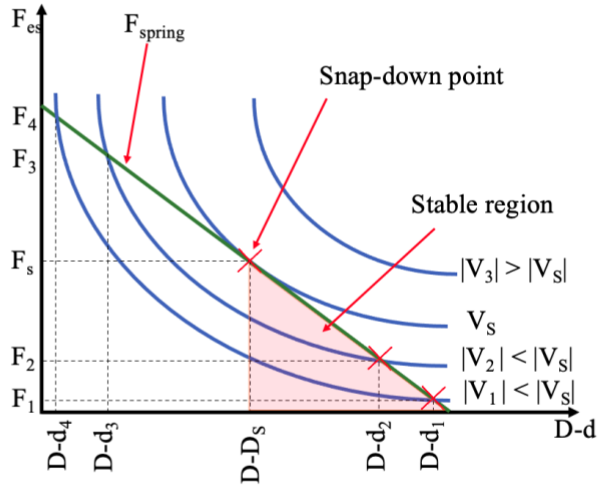

Figure 2.2. Electrostatic and spring forces vs. moving electrode displacement at three voltages (V_1, V_2 and V_S). The red crosses show the equilibrium points and for the voltages larger than V_S, and for displacements more than D_S the actuator is unstable.

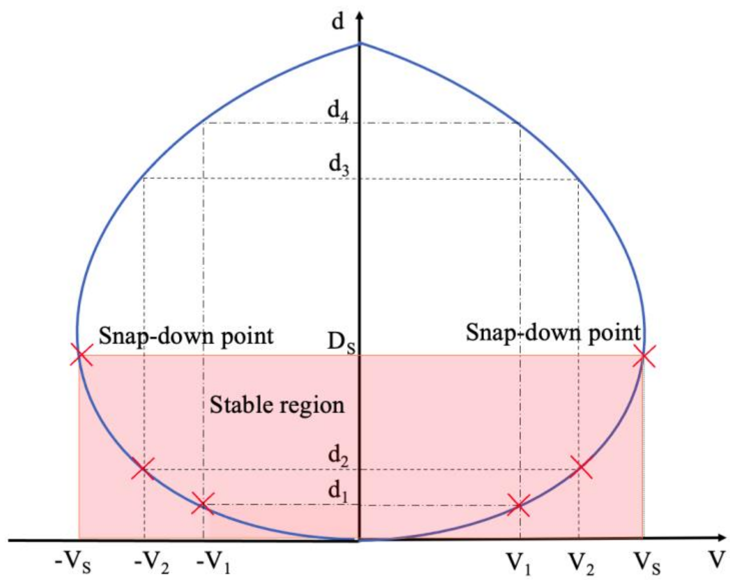

Figure 2.3. Displacement (d) vs. the controlling voltage. The red crosses show the equilibrium points and for the voltages larger than V_S, the actuator is unstable.

2.3 Electrostatic actuator applications

Electrostatic actuators have been used in many different applications. Examples include microvalves, micropumps, switches, and micromirrors.

Microvalves are one of the most functional elements in microfluidic systems. The inherent properties of electrostatic actuators make this actuator very suitable for biological applications due to their high-energy efficiency, high moving range, and relatively low temperature. A basic electrostatic microvalve consists of two parallel plates at two squeezable opposite sides of a microchannel. At least one of the plates (moving electrode) must be flexible to be squeezed under the electric field produced by a relatively high exciting voltage applied across the channel. The flexible plate restricts the channel and prevents the fluid from moving. In [40], the applied voltage to close the 2 µm height channel is approximately 150 V.

Micropumps are another application that commonly uses electrostatic actuators. The micropump, which is represented in [41], has a flow rate of 1-10 µl/min that was achieved by applying a voltage of 50-100 V. By applying this voltage across the moving diaphragm (moving electrode) and the top electrode, the fluid is sucked inside the chamber. In the next step by applying a voltage across diaphragm and the bottom electrode, the fluid is pushed out. Figure 2.4 shows the micropump schematic pumping in and out.

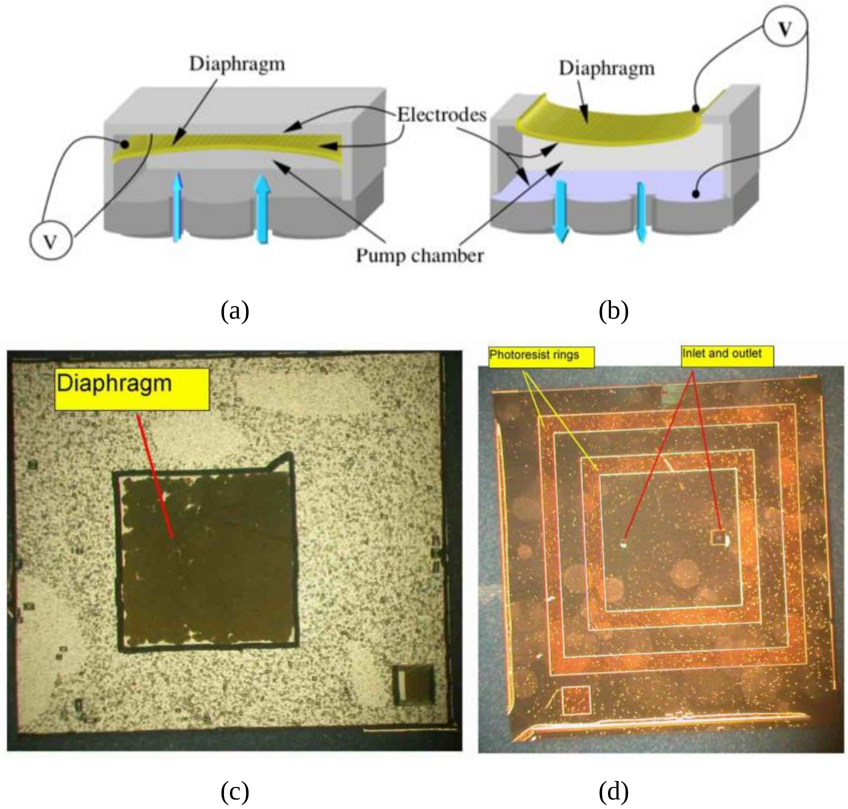

Figure 2.4. Micropump configurations. (a) Applying a voltage across the air gap above the chamber. (b) Applying a voltage across the pump chamber. (c) A 5 mm diaphragm on a MEMS chip. (d) A valve chip showing inlet and outlet. Reproduced from [A. Machauf, Y. Nemirovsky, "A membrane micropump electrostatically actuated across the working fluid.," *J. Micromech. Microeng*. vol. 15, pp. 2309-2316, 2005], with permission of IOP Publishing.

RF switches are another application that often use electrostatic actuators to operate. There are two types of metal contact and capacitive coupling RF switches, and each is designed to perform for a different frequency range. Texas Instruments built one example of a capacitive coupling switch [42]. The top flexible membrane (moving electrode) is about 120 μm in width and 280 μm in length and is suspended almost 4 μm above the bottom fixed electrode. The 1 μm thick membrane requires at least 50 V to snap down and close the switch. After actuating the switch, the metallic membrane comes in contact with the dielectric layer coated on the bottom electrode, producing a low ac impedance path to the surrounding electrical ground. Therefore, it prevents the signal from traversing the switch (figure 2.5). Capacitive coupling can be preferred to metal contact to prevent stiction and micro-welding. However, capacitive coupling requires the switch to operate at higher frequencies. This switch has a switching speed of lower than 6 μs [43].

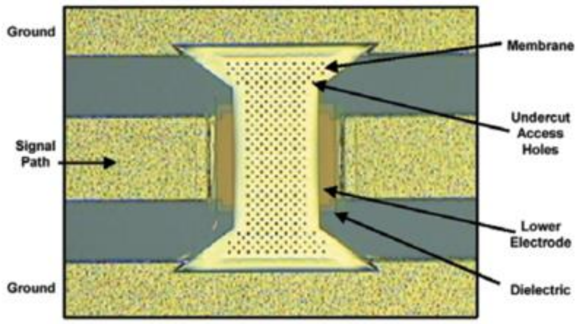

(a)

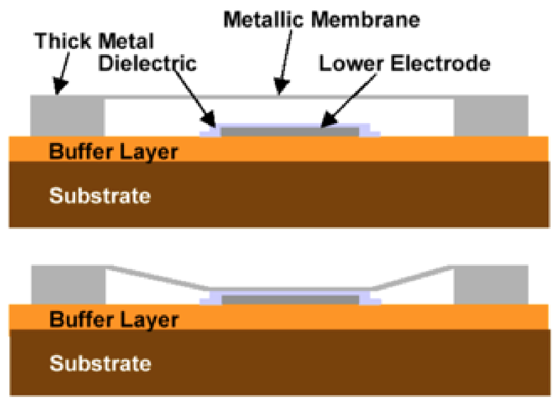

(b)

Figure 2.5. (a) Raytheon capacitive shunt switch micrograph. (b) Illustration from top to bottom: non-actuated and actuated switch. Reproduced from [J. J. Yao, ''RF MEMS from a device perspective,'' *J. Micromech. Microeng*., vol. 10, pp. R9–R38, Dec. 2000], with permission of IOP Publishing.

Micromirrors are another application using MEMS electrostatic actuators for optical devices. A DM system employs an array of actuators to deform a micromirror surface. It is often applied to correct the aberration caused in an optical system. The process of compensation of aberration is called phase conjugation, and in the case of a changing optic path (such as due to atmospheric turbulence), many segments of the mirror are required to be controlled in real-time [44]. Figure 2.6a shows a schematic of two actuators attached to a flexible mirror to deform the mirror membrane. The picture of a single actuator is shown in figure 2.6b, with the deflected mirror shown on the left and undeflected mirror on the right.

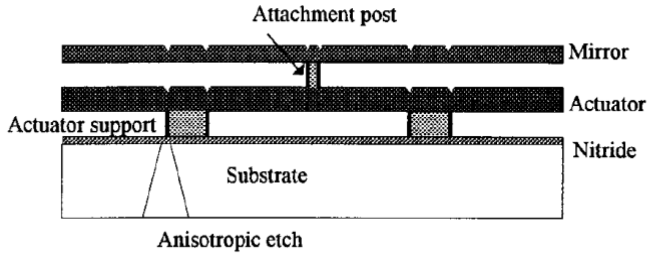

(a)

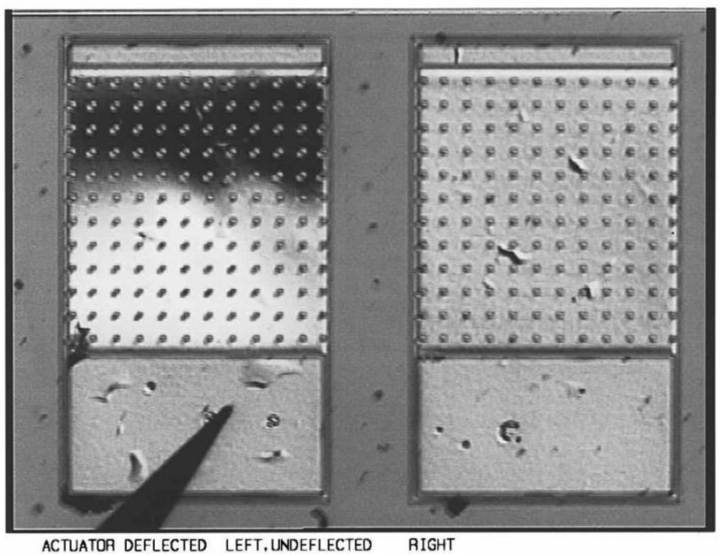

(b)

Figure 2.6. (a) Schematic of a deformable mirror with actuators attached to the flexible mirror. (b) A deflected (left) and non-deflected (right) actuator. Reproduced from [R. K. Mali, T. G. Bifano, and M. N. Horenstein, "Development of microelectromechanical deformable mirrors for phase modulation of light," *Opt. Eng.*, vol. 36, no. 2, pp. 542–548, 1997], with permission of SPIE.

The electrostatic actuator of figure 2.6 is a double cantilever beam (fixed–fixed beam) that can be deflected down due to the voltage between the substrate and the cantilever beam. The primary parameters of the DM are the number of actuators, control bandwidth, and maximum actuator stroke. The wavefront phase error is the parameter that determines the required stroke in design. In [44], the maximum stroke of 0.9 µm is measured by applying 60 V.

As summarized previously, electrostatic actuators are employed in various applications. The applications above are of the most relevant categories electrostatic actuators can be used. According to [39], RF switches are the application used by electrostatic actuators most. Comparing the applications, the static controlling voltage and the moving range are the common controlling parameters in all the applications. Therefore, studying and improving them makes the most sense to improve the performance of this actuator. Table 2.1 shows the voltage and moving range (The range is one third of the gap size between electrodes) in each application, and as can be seen, the voltages are relatively high depending on the actuator's performance parameters. Therefore, various groups have studied different approaches in the literature to enhance the characteristics of the electrostatic actuator.

Table 2.1. Voltage and geometrical features of the electrostatic actuator utilized in applications.

Application	Actuating voltage [V]	Gap size between electrodes [μm]	Electrode size [mm^2]	Ref.
Microvalve	150	2	0.9	[39]
Micropump	50 - 100	85 - 90	9	[40]
RF Microswitch	50	4	0.0336	[41,42]
Deformable Mirror (DM)	300	5.5	0.1225	[43]

2.4 Higher performance electrostatic actuators (methods to solve the electrostatic actuator pull-in effect)

Section 2.2 described an electrostatic actuator in its simplest configuration form, which consists of two oppositely charged plates located in parallel. The applied voltage across the parallel electrodes generates the pulling electrostatic force and attracts the electrodes toward each other. Since no continual electric current is required for the actuator operation, the electrostatic force-based actuator requires low power. Also, its switching speed can be reasonably high [45] since there are no thermal effects to consider. Another significant advantage of an electrostatic actuator is that it can be commonly compatible with standard CMOS processes. Therefore, batch fabrication is possible, which has cost-benefit and is more straightforward for bulk manufacturing [46]. Looking closely at equation (1), we realize that the force is inversely proportional to the gap between the electrodes. Therefore, as the electrodes move toward each other, the electrostatic force increases.

The pull-in effect results in limited control of actuator motion to only 1/3 of the spacing between the electrodes [47], as was explained earlier. Several studies were conducted to improve the electrostatic actuator's travel range and the actuating voltage. Employing a charge storage capacitor is one of the first electrical solutions used to prevent the snap-down. This uses a capacitor in series with the actuator. Seeger et al. proposed this electrical technique to elevate the controllable range of motion. However, tip-in instability is the problem of this design which is due to the rotation of the actuator [48]. Toshiyuki et al. designed a bidirectional actuator putting driving electrodes above and below the MEMS electrode [49]. This electrical method was useful to extend the range of motion, but the MEMS element is blocked by both electrodes (figure 2.7). Even though the design helps to improve the actuator performance, the application of this actuator is limited due to the MEMS obstruction on top and bottom. Employing an offset electrode is another electrical method that has been used to extend the travel range (figure 2.8). Su et al. utilized offset electrodes to improve the electrostatic actuator using the fringing fields to control the movement and avoid the electrodes' engagement as shown in figure 2.9 [50].

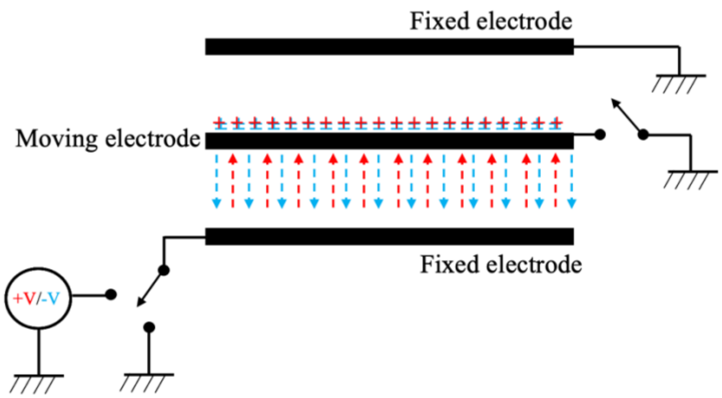

Figure 2.7. Bidirectional actuator schematic, including one moving electrode between two fixed electrodes.

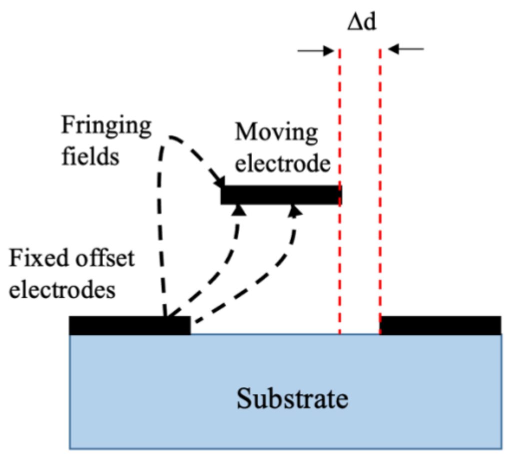

Figure 2.8. Offset electrode actuator schematic (front view), including one moving electrode and the fixed offset electrodes.

They also showed that this electrode configuration helps to increase the range of motion. In the same fashion, an external electrode was also employed by Rosa et al. [51] to avoid the snap-down using cantilever beams with one free end. In both cases, the lateral gap between the MEMS and the electrodes should be larger than a certain value, otherwise, the actuator snaps down. More importantly, in all cases employing offset electrodes, the wide size of adjacent electrodes makes the actuator size non-compact as can be seen in figure 2.9.

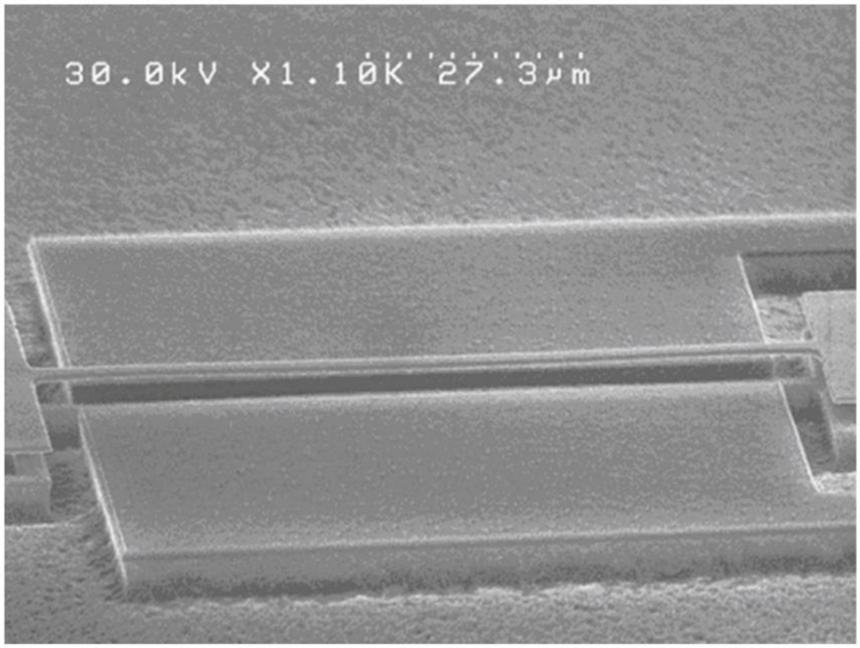

Figure 2.9. Offset electrode method to solve the pull-in effect and preventing the snap-down. Reproduced from [J. Su, H. Yang, P. Fay, W. Porod, and G. H. Bernstein, "A surface micromachined offset-drive method to extend the electrostatic travel range," *J. Micromech. Microeng*., vol. 20, no. 1, Jan. 2010], with permission of IOP Publishing.

Employing non-linear springs that offer increasing restoring spring force with increasing displacement is another way to delay the snap-down (pull-in) and helps to improve the actuator's performance. Hung et al. designed an actuator using leverage bending and strain to stiffen to increase the travel range but it also comes with a relatively large control voltage [52]. Qiao et al. proposed a parallel actuator with a four-set of springs called a two-beam spring. In this strategy, the controlling ranges are extended by 50% increasing the spring constant four times the initial value at the beginning of the operation, but the voltage is not increased dramatically compared to the parallel plate design [53]. Pre-stressed actuators [54] are another solution to raise the movement range of the actuator before snap-down. In this method, the initial gap spacing between MEMS and the fixed electrode is provided by designing the MEMS element being stressed after the releasing step. In this method, heat treatment can help to increase the gap and the moving range.

However, the controlling voltage is still high in this method and the actuator performance is highly sensitive to the fabrication and post-fabrication parameters.

The various delaying pull-in feedback are listed in table 2.2 according to their achievement in developing a higher-performance electrostatic actuator. As can be seen, in most cases, the exciting voltage is still relatively high.

Table 2.2. Methods for improving travel distance and actuating voltage of electrostatic actuators.

Method	Initial gap [μm]	Maximum displacement	Actuating voltage [V]	Disadvantage	Ref.
Series capacitor-Charge control	N/A	100%	N/A	Tip-in instability	[48]
Bi-directional	1.12 mm	<60%	~140	Obstructed MEMS by electrodes	[49]
Offset-drive electrode	2	80%	80	Non compact design	[50]
External electrode	68	~92%	160	Lateral gap between electrodes – large voltage	[51]
Leverage bending & strain stiffening	2	100%	200	Large voltage	[52]
Two-beam structure	2	50%	4	Limited range of motion	[53]
Pre-stressed actuator	110	82%	200	Relatively high voltage	[54]

2.5 Electrostatic actuator arrays

Electrostatic actuators have been employed in very various applications in very wide research fields. The common applications that use electrostatic actuators were studied. Also, there have been many approaches to solve the actuator limitations as listed in section 2.4. The strategies are mostly solving the problem of a single actuator. However, if we want to use arrays of actuators, some other problems arise. Therefore, the applications where multiple actuators are needed were also studied.

Fukushige et al. designed an array of conical spring actuators for the micro-optical systems as shown in figure 2.10 [55]. The array consists of a 10 by 10 actuator array. The actuators were designed primarily to have a driving voltage of 162 V for a maximum stroke of 180 μm. The packing density of the arrays was also high since the actuator electrode and the interconnections were in the same layer. A multilayer interconnection design was used to make the array more compact. For the smaller controlling voltage and for lowering its stroke (81 V for 200 µm), a thinner dielectric material was utilized. However, a thinner dielectric material might not be the best solution as the breakdown voltage is smaller for a thinner layer.

Another application of an array of electrostatic actuators is for automated telecommunication networks. A reconfigurable array of MEMS electrostatic switches can be used in copper-wire telecommunication systems to reduce the cost of reconfiguration for different systems with different customizations. Braun et al. designed two arrays of 5 × 5 and 20 × 20 MEMS electrostatic switches for automating telecommunication networks [56]. The switches were designed based on an S-shaped actuators. According to the design and measurements, the actuation voltage for closing the switches of a 5 × 5 array was 20 V while it was 93.2 V for the 20 × 20 array. The reason of the higher actuating voltage is having a smaller area allocated to each electrode due to the higher need for signal lines. As the number of actuators increases the required area for the signal lines are higher. The higher voltage is also due to the non-optimized fabrication process. Therefore, in this case also the higher number of actuators is a significant reason for the higher actuating voltage. The arrays of switches are illustrated in figure 2.11. Another application of using arrays of MEMS electrostatic actuators is for an airflow distributed micromanipulation. The array is basically for controlling the air-flow force for microscopic manipulation, micro conveyance and sorting small objects.

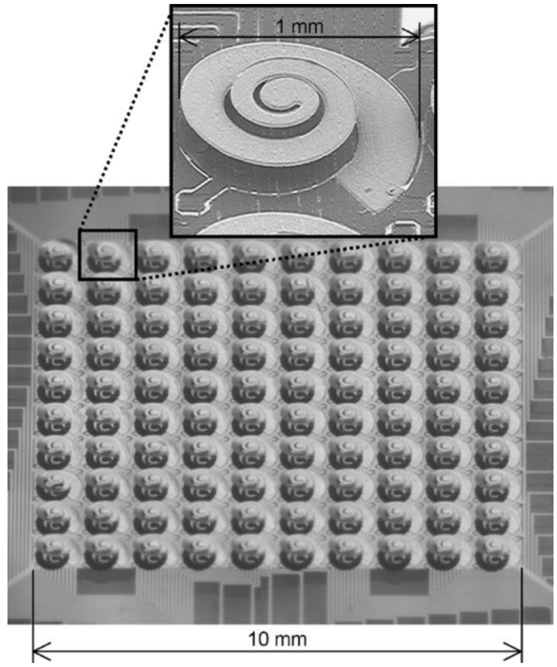

Figure 2.10. An array of 10 × 10 conical spring actuators and one enlarged actuator. Reproduced from [T. Fukushige, S. Hata, and A. Shimokohbe, "A MEMS conical spring actuator array," *J. Microelectromech. Syst*., vol. 14, no. 2, pp. 243–253, Apr. 2005], with permission of IOP Publishing.

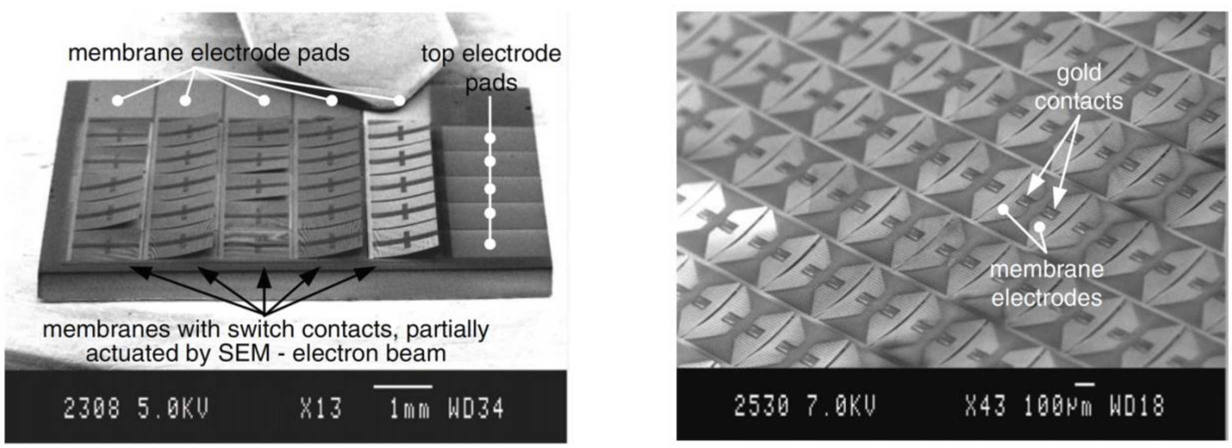

(a) (b)

Figure 2.11. Arrays of electrostatic MEMS switches with (a) 5 × 5 number of arrays and (b) 20 × 20 number of arrays of double-switch membrane. Reproduced from [S. Braun, J. Oberhammer, and G. Stemme, "Single-chip MEMS 5 × 5 and 20 × 20 double-pole single-throw switch arrays for automating telecommunication networks," *J. Micromech. Microeng.*, vol. 18, no. 1, p. 015 014, Dec. 1–11, 2007], with permission of IOP Publishing.

Fukuta et al. designed a 560 micro actuator array of 35 × 35 mm^2, as shown in figure 2.12 [57]. Therefore, employing an array of micromanipulators provides the intelligent motion control. However, the pull-in voltage is still relatively high and about 123 V. They employed a fabrication method using thermal oxidation to reduce the voltage by changing the rectangular movable electrode to a trapezoidal shape in the first stage. Therefore, the voltage was reduced to 106.1 V. By sharpening the electrode having higher thickness of the silicon oxidized, the pull-in was reduced even more down to 91.2 V for the displacement of almost 15 µm. We also see in this application that the relatively high controlling voltage is an issue and even though there have been efforts to decrease the voltage, each single actuator still needs that high voltage and its own controlling circuits.

Aravelo et al. designed an array of hexagonal shaped electrostatic actuators in a chip size of 2.3 × 2.3 cm^2 [58]. The array was utilized for digital sound reconstruction and parametric directional loudspeakers. In this case, the actuator excitation voltage was as high as 95 V. Bohringer et al. used an array of more than 15000 electrostatic actuators for manipulation of small, flat objects [59]. However, only 30% of the actuators were utilized due to the existing constraints for the fabrication releasing structures. The actuators were tested by lifting glass pieces for several µm within the actuator moving range. Each actuator required almost 60 V to provide 1.2 mN/mm^2 when the gap between the electrodes is 5 µm. Theoretically, the maximum displacement can't be more than one third of the gap, which can't be more than almost 2 µm.

MEMS electrostatic actuators also can be used for multi-object spectroscopy for space and ground-based telescopes. Canonica et al. designed, fabricated, and tested multiple prototype tilting micromirror arrays for this purpose [60]. They tested a 5 × 5 array and had an array of 64 × 32 actuators under development. However, the actuation voltage for the actuator is less than 100 V for tilting of 20°.

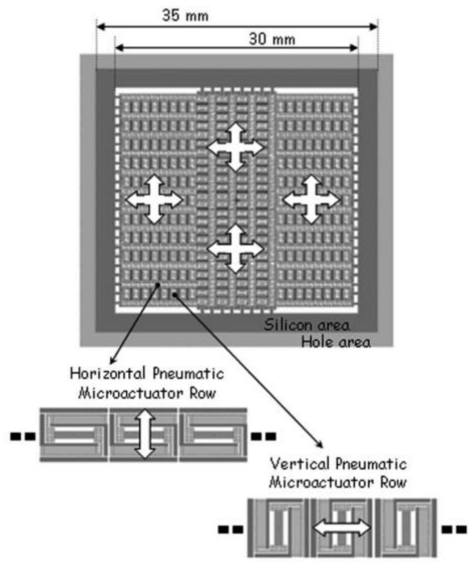

Figure 2.12. Mask design of pneumatic 560 micro actuator array for motion surface a 35 × 35 mm^2 area. Reproduced from [Y. Fukuta, Y.-A. Chapuis, Y. Mita, and H. Fujita. "Design, fabrication and control of mems-based actuator arrays for airflow distributed micromanipulation," *IEEE Journal of Microelectromechanical Systems*, 15(4):912–926, 2006], with permission of IEEE.

The two other applications in that arrays of actuators are commonly used, are micromirror arrays (MMAs) and DMs. Cornelissen et al. introduced an array of 68 × 68 (4096) actuators for a MEMS DM with a 4 µm stroke [61]. The device performance showed an operation voltage of 210 – 260 V for a stroke of 3.5 µm. It is evident that the voltage is very high given the very small range of motion. The external drive electronics for the 4096 elements are shown in figure 2.13. We see that the electronics are not truly compact as it is desired to design the MEMS to be small. However, the driving circuits are bulky especially when an array of hundreds of actuators is required.

Table 2.3 shows the applications that employ arrays of electrostatic actuators. As the voltage of the electrostatic actuator is high, many DMs use external driving circuits. However, for arrays of more than 10000 actuators, an integrated address circuitry is necessary. As an example of integrated circuitry, an active address matrix can be used, and this technology is implemented preferably using a CMOS backplane. However, the small-scale generated voltage by CMOS circuitry can be used only for DMs with small strokes and CMOS cannot be so helpful [62].

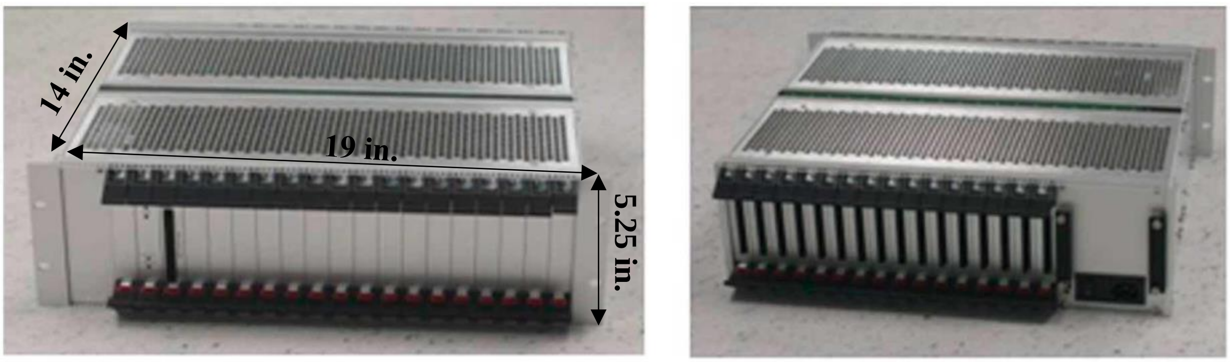

(a) (b)

Figure 2.13. (a) A compact drive electronics for 4096 elements showing the inputs and (b) the high voltage outputs. Reproduced from [S. A. Cornelissen, "4096-element continuous face-sheet MEMS deformable mirror for high-contrast imaging," *J. Micro/Nanolithography, MEMS, MOEMS*, vol. 8, no. 3, p. 031308, 2009.], with permission of SPIE.

Table 2.3. Different applications of using arrays of electrostatic actuators with high actuating voltage.

Actuator	Number of arrays	Actuating voltage	Displacement / Angle	Ref.
Conical spring actuator array	100 (10 × 10)	81 V	200 μm	[55]
Double-pole single-throw switch arrays	400 (20 × 20)	93.2 V	-	[56]
Actuator array for air-flow micromanipulation	560 (35 ×35)	91.2 V	15 μm	[57]
MEMS digital Loudspeaker	64 (8 × 8)	95 V	-	[58]
Actuator array for micromanipulation	15000	60 V	5 μm	[59]
Multi-object spectroscopy	2048 (64 × 32)	100 V	20°	[60]
MEMS deformable mirror	4096 (68 ×68)	210 – 260 V	3.5 μm	[61]

The actuator arrays may need digital (switches) or analog (DMs) electronic controlling circuits, depending on applications. Deformable mirrors are the main applications in need of analog control. The controlling circuit regularly consists of a digital control system, a digital-to-analog converter, and a high voltage (HV) amplifier. To achieve precise control over the DMs, the voltage circuits that control them must be highly accurate and have sufficient resolution. However, in certain situations, the cost of building the control circuit can be higher than that of the MEMS, which is counterintuitive. The purpose of using MEMS is to lower manufacturing costs and enhance batch fabrication efficiency, but the increased circuit cost could result in a higher overall product price [62]. Pulse width modulation (PWM) is one method that can be used to lower the price, as C. Pollock showed that PWM could be used as a low-cost method for controlling the MEMS electrostatic actuators [63,64]. However, the voltage range can still be relatively high, and the circuitry is not necessarily integrated. Dai et al. designed an integrated 300 V LDMOS analog drive circuit for MEMS DMs [65]. As can be seen, integrated high-voltage drive circuits can be created. However, these circuits have very different issues in their performance. The HV circuits consist of multiple three-stage levels. The final stage amplifies the low voltage generated in the second stage. One of the prevalent problems is the over-voltage stress reliability that mainly occurs at the time of power on/off during the transition time. The middle-stage circuit voltage should always be kept below a certain threshold to avoid this issue. Furthermore, overshoot voltage at the output of the final stage is another issue using the HV circuitry that can destabilize the actuator's performance.

It can be concluded that, on one hand, using integrated circuits for extensive stroke applications such as DMs is challenging, considering recent advances and obstacles briefly indicated. On the other hand, there might be better solutions than external circuitry, as compact drive electronics or on-chip drive circuitry is desired in many applications. Also, in the application with a single actuator or in the array-based applications, the literature solutions for voltage reduction are based only on reducing one single actuator voltage. There is no low-voltage solution for arrays of actuators addressing the effect of arrays. In contrast, the tri-electrode topology presented in this work is an array-based solution to reduce the actuating voltage. In this method, the controlling voltage of an array of the electrostatic actuator can be reduced such that a low voltage integrated circuit can drive them, and only one common external larger voltage circuit link is used for the entire array. It will precisely resolve the high voltage wiring issues in compact driving systems. The tri-electrode topology and the work carried out in our research group are briefly presented in the following section.

3

Tri-electrode Topology

Contents

3.1 Introduction

As explained in the previous chapter, the MEMS conventional electrostatic actuator is excellent in terms of power consumption and simple microfabrication. However, the actuator's pull-in effect limits the range of motion and the controlling voltage. Therefore, a MEMS-based tri-electrode electrostatic actuator is introduced to solve the issue so that we can have more control over the controlling voltage and the moving range.

3.2 RSFM (Restoring Spring Force Method) Methodology

Finite element method (FEM) was primarily employed in the actuator design and analysis using COMSOL Multiphysics. The FEM interface provides the Multiphysics feature for solving different physics equations. However, in electrostatic physics, the response curves can be unstable at the snap-down point, and Multiphysics was found to have difficulties in solving exact solutions around the snap-down point. Therefore, a method was explored called restoring spring force method (RSFM), to extract the response curves more precisely. The RSFM method is based on the electrostatic actuator theory previously described in section 2.2. In RSFM, the electrostatic force applied to the moving MEMS electrode can be characterized using COMSOL FEM analysis for a range of controlling voltage and gap spacings between electrodes. For example, for the conventional actuator, both electrodes are considered fixed at the distance D from each other, then the forces are determined using FEM at a specific voltage range. The study is repeated for the desired range of D. Eventually, there are all the possible force values at given applied voltages and gap spacings. According to this fact that at equilibrium, the electrostatic and restoring spring forces are equal, the displacement corresponding to each applied voltage can be characterized for a specific linear spring constant. In order to find a general solution, the results are all normalized to the gap between the moving and the adjacent fixed controlling electrode. The numerical studies were carried out using MATLAB software and the Livelink COMSOL module linking these two platforms. Using this method for a conventional parallel plate actuator might not be advantageous as the problem was already studied, and its analytical equation is extracted. However, in the case of a new unknown actuator, such as the tri-electrode, the RSFM method helps us to extract and plot the tri-electrode response curves.

3.3 Tri-electrode configuration (definition)

The tri-electrode electrostatic actuator schematic is illustrated in figure 3.1. The actuator consists of a stationary solid electrode called the primary electrode, a perforated stationary electrode called the intermediate electrode, and a moving MEMS electrode. The new stationary perforated electrode is the difference between the conventional topology and the tri-electrode. In the conventional topology, the operating voltage was applied across the electrodes. However, in the tri-electrode, voltages are applied to both the intermediate and primary electrodes, with the MEMS electrode electrically grounded. The voltage applied to the primary electrode (V_P) is fixed, and the voltage on the intermediate electrode (V_I) is a varying controlling voltage, which controls the movement of the MEMS electrode. Therefore, the primary electrode provides a background electric field by applying V_P, and the intermediate electrode controls the MEMS's movement with a modulating controlling voltage. As we know, the conventional actuator generates the attractive force if the voltage is either positive or negative. However, for the tri-electrode topology, depending on the primary electrode voltage polarity, the intermediate electrode can provide a supporting (when the intermediate and the primary electrodes are supplied with the same voltage polarity) or opposing (when the intermediate and the primary electrodes are supplied with the opposite voltage polarities) attractive force.

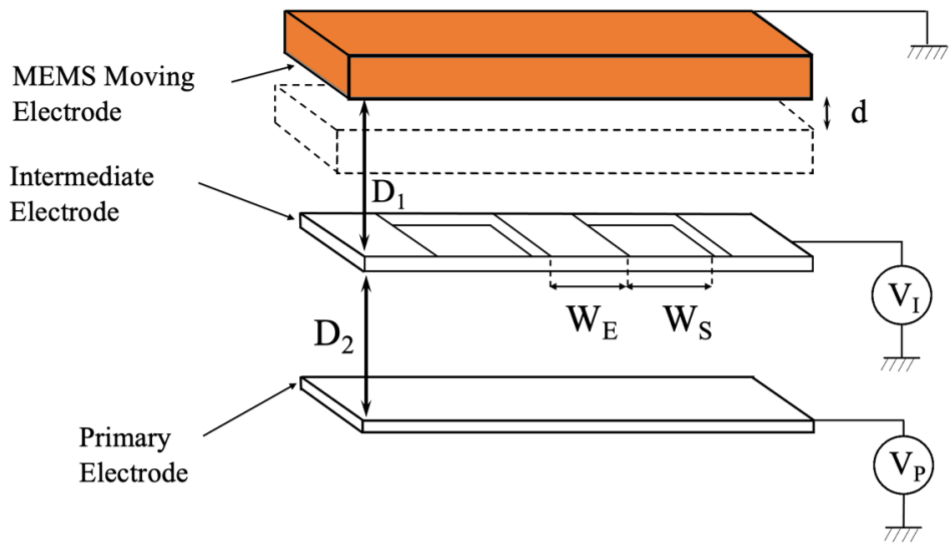

Figure 3.1. Tri-electrode electrostatic actuator topology, including one grounded MEMS moving electrode and two stationary electeodes. The stationary electrodes are one perforated intermediate and one solid primary electrode.

Detailed numerical simulations were performed for an arbitrary controlling voltage and geometrical sizes, in order to see the nature of the tri-electrode performance for all design parameters. The numerical simulations were performed by solving equation (3.1) which is a representation of Gauss' law. It is solved using the potential condition in the static situation and continuity equation [66]. The equation is as

$$-\nabla . (\varepsilon_0 \nabla V - P) = \rho, \tag{3.1}$$

where P is the electric polarization vector, ρ is the space charge density, V is the voltage, and ε_0 is absolute vacuum permittivity. In the simulations undertaken in COMSOL Multiphysics, zero charge was assigned to the exterior boundaries as the boundary conditions prevent any displacement fields from reaching inside the boundary. The electrode material was aluminum, and all the electrodes were biased at their specific voltages. Following these, in the COMSOL the MEMS moving electrode electrostatic force is characterized for a range of gaps between MEMS and intermediate electrodes (D_1) and at a range of controlling voltage (V_I) for a fixed primary electrode voltage (V_P). In the FEM simulations, it was considered that the MEMS element is a fixed electrode, and the electrostatic force is determined at all possible D_1 and V_I values. Following this, using the RSFM method defined earlier, the restoring spring force is calculated for a linear spring. The required voltage for a moving electrode displacement can be determined when the restoring spring and electrostatic forces are equal (equilibrium). It was assumed that the actuator performs in the mechanically stable range in these studies.

Due to the need for numerous numerical studies, 2D simulations were employed to study the tri-electrode performance. The tri-electrode configuration is illustrated in figure 3.2.

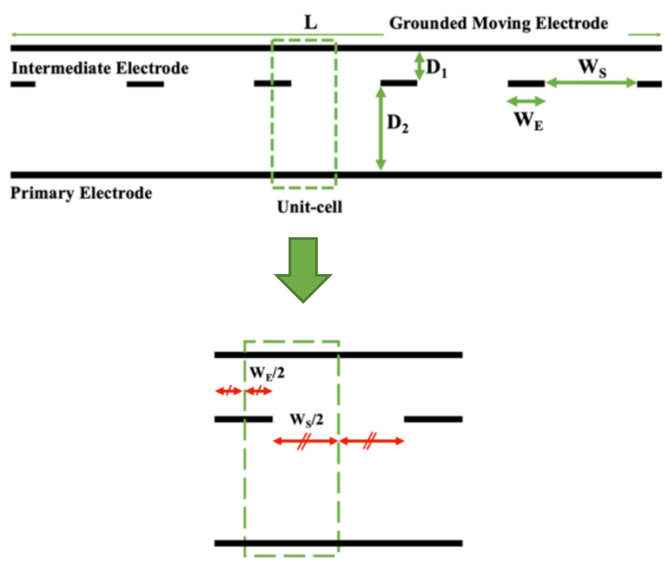

Figure 3.2. The 2D schematic of the tri-electrode actuator configuration and the unit-cell used in the numerical studies.

The essential parameters of the topology are also highlighted in the figure and are indicated as follows:

- Spacing between the MEMS moving electrode and the intermediate electrode (D_1)
- Spacing between the primary and the intermediate electrode (D_2)
- Width of the solid elements of the intermediate electrode (W_E)
- Gap spacing between solid elements of the intermediate electrode (W_S)
- Controlling voltage of the intermediate electrode (V_I)
- Background voltage of the primary electrode (V_P)

The tri-electrode is confined in an air-box, in order to remove the fringing fields. The airbox refers to the space surrounding the specified geometry that is filled with air. It is necessary to define the material between the electrodes, which in this case is air. All the dimensions are also normalized to D_1 spacing to make the results dimensionless. Therefore, the results can be utilized for any actuator with any size. Looking at the 2D schematic, we realize that the geometry is a repeating product of the smallest unit cells shown in figure 3.2. Thus, the studies were carried out on the unit-cell to reduce the entire time of the simulations. In the following studies, the parameters D_2, W_S and W_E were swept at a specific range summarized in table 3.1. The parameters are normalized with D_1.

Table 3.1. The parameters and their values utilized in the numerical simulations.

Parameters	Values
W_S	$(1.0 – 4.0)\ D_1$
W_E	$(0.167 – 2.5)\ D_1$
D_2	$(1.0 – 2.67)\ D_1$

3.4 Tri-electrode performance analysis

In this section, the impact of different parameters, including the polarity of the controlling voltage, intermediate electrode gap spacings, the electrode width and the spacing between the stationary electrodes on the actuator's performance, is investigated. The results were published in [67].

3.4.1 Controlling voltage (V_I) polarity effect

The electrostatic force generated in a conventional parallel plate actuator is not a function of the applied voltage polarity. In both cases of the positive and negative voltages, the generated force is pulling. However, in the tri-electrode, the intermediate electrode voltage should have the same polarity as the primary voltage to reinforce the background field, as an opposing voltage would reduce the background force. Therefore, numerical studies were performed to see this impact, and the results are depicted in figure 3.3.

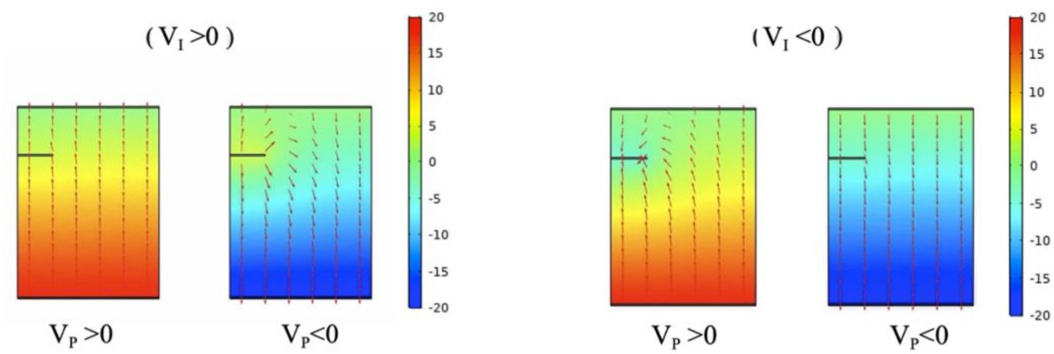

Figure 3.3. The potential and the electric field distribution between the tri-electrode topology (unit-cell) electrodes. The electric fields are more uniform when V_I and V_P have the same polarity. The legend unit is the voltage shown on the unit-cells.

As shown in figure 3.3, the electric field distributions are almost uniform in either direction when both voltages are positive or negative ($V_P > V_I > 0$ or $V_P < 0$ and $V_I < 0$). However, when the polarity of V_I and V_P are not identical, each intermediate and primary electrode provides opposing forces, with the primary and the intermediate electrodes generating pulling and lifting forces, respectively. The lifting force can be employed if we want to control the actuator in the opposite direction.

3.4.2 Solid/perforated conventional actuator

A perforated conventional actuator was designed, and its response curve compared with a solid conventional at different perforations (figure 3.4), in order to understand the role of the intermediate electrode on the tri-electrode actuator performance. The RSFM method extracted the displacement vs. voltage response curve of the two solid and perforated electrostatic actuators. This comparison was carried out to provide a baseline for the tri-electrode topology performance. The controlling voltage here is V_C, yet it is normalized to the snap-down voltage as:

$$V_S = \sqrt{\frac{8kD_1^3}{27\varepsilon_0 L^2}} \tag{3.2}$$

where D_1 is the conventional gap spacing, L is the actuator moving electrode dimension and k is the spring constant. The displacement axis is normalized to the distance value that the conventional actuator travels before snap down ($D_S = 1/3\ D_1$).

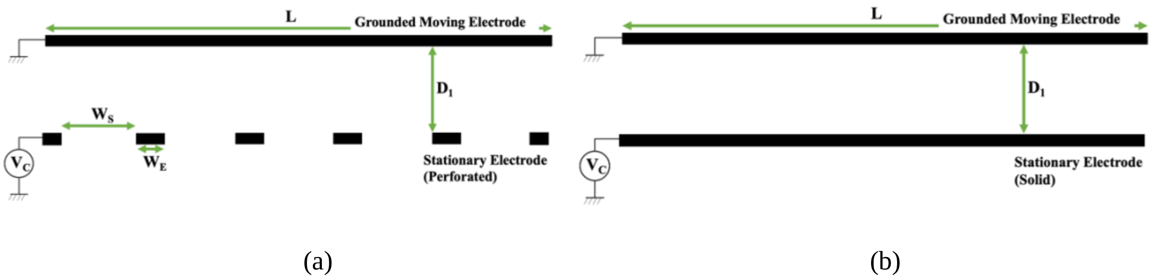

Figure 3.4. The 2D cross section schematic of a (a) perforated and (b) solid conventional actuator.

The displacement vs. controlling voltage response curve is depicted in figure 3.5 for three different intermediate electrode perforation ratios (W_S:W_E = 1:1, 3:1 and 9:1). Looking closely at this figure, the significant critical effects of the tri-electrode topology are shown. It can be seen that the larger the gap spacing (W_S), the larger the snap-down voltage is. This is due to the smaller intermediate electrode effective area, which results in reduced electrostatic force (thus requiring larger voltage), and consequently larger snap-down voltage for almost the same displacement. In this example, the displacement is almost *1.05* D_S for both 1:1 and 1:3 ratios and *1.1* D_S for 1:9. The larger displacement and delay in snap-down is due to the effect that as the MEMS moves closer to the stationary electrode, the coupling electrostatic force becomes more localized (negative feedback). This is the one of the main effects of the tri-electrode topology used to increase the travel range.

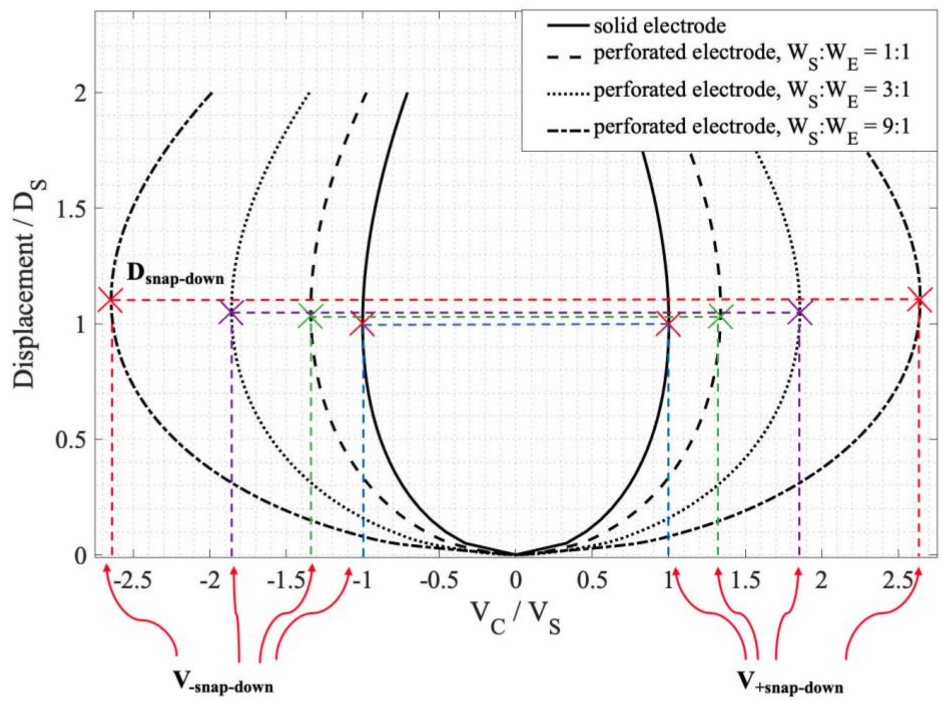

Figure 3.5. Displacement vs. controlling voltage response curves of the solid and perforated electrode (W_S:W_E = 1:1, 1:3 and 1:9) conventional actuators.

3.4.3 Tri-electrode – primary electrode

The perforated conventional actuator helps delay the snap-down and increase the range of motion, but the snap-down voltage is also significantly higher than the increase in the range. In order to solve this issue, another fixed solid electrode (primary electrode) is added under the perforated electrode forming the tri-electrode configuration. The primary electrode helps to increase the overall electrostatic force. The amount of electrostatic force is a function of intermediate electrode spacing (W_S). The larger the spacing, the more electrostatic force couples with the moving MEMS. Therefore, a smaller controlling voltage (V_I) is required. On the other hand, the intermediate electrode's control ability on the actuator's movement is less for that larger spacing. An arbitrary perforation size of W_S:W_E = 3:1 ($W_S = 2.5\ D_1$, $D_2 = 1.67\ D_1$, $V_P = 4.37\ V_S$,

W_E = 0.83 D_1) was chosen to show the tri-electrode and displacement vs. controlling voltage response curve of the tri-electrode topology. The response curves of the tri-electrode and the conventional topologies are shown in figure 3.6.

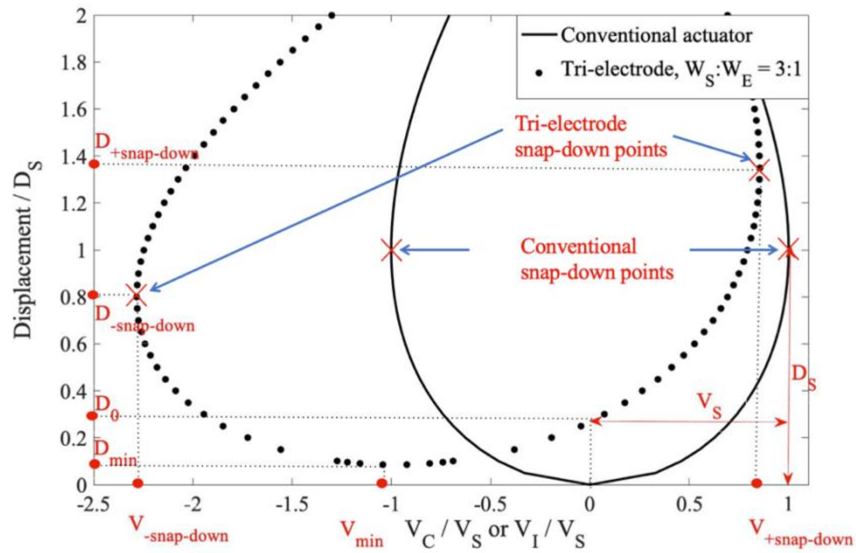

Figure 3.6. Displacement vs. voltages (V_C or V_I) curves of the conventional and tri-electrode topologies for W_S:W_E = 3:1.

Looking at the tri-electrode, some noteworthy points were observed about its response curve as follows. In contrast to conventional, the response curve is not symmetric with the controlling voltage, and the positive and negative snap-down voltages ($V_{+/- \, snap\text{-}down}$ at $D_{+/- \, snap\text{-}down}$) are not equal in magnitude. In positive voltage range, the controlling voltage (V_I) is smaller than the conventional actuator for the same given displacement. This means that adding the primary electrode helps reduce the voltage, while the displacement before snap-down is also larger than in the perforated conventional actuator. When the intermediate electrode voltage is zero (V_I = 0), there is a non-zero displacement (D_0) due to the primary electrode voltage (V_P). Also, at the beginning of increasing the negative V_I, the non-zero displacement reduces to a specific minimum value (D_{min} and V_{min} as the corresponding voltage) since this V_I opposes the V_P, but still, the V_P is dominant. At higher negative V_I values, the displacement again increases. The tri-electrode case, shown in figure 3.6, has a higher controllable displacement range. The maximum controllable displacement ($\Delta d_{max} = D_{+snap\text{-}down} - D_{min}$) is almost 25% ($\Delta d_{max} = 1.25\ D_S$) more than the conventional actuator.

3.4.4 Tri-electrode parameters

In order to study the tri-electrode parameters, some definitions are used to make the explorations easier and more understandable. Some parameters are summarized in table 3.2.

Table 3.2. The displacement and the parameters of the corresponding voltage shown on figure 8 to describe the tri-electrode performance.

Displacement		Voltage on intermediate electrode (V_I)
D_0	Displacement when V_I = 0 V	$V_I = 0$
D_{min}	Minimum displacement	$V_I = V_{min}$
Δd_{max}	Maximum travel range from $D_{+snap\text{-}down} - D_{min}$	$\Delta V_{max} = V_{+snap\text{-}down} - V_{min}$
$D_{+snap\text{-}down}$	Positive V_I snap-down position	$V_I = V_{+snap\text{-}down}$
$D_{-snap\text{-}down}$	Negative V_I snap-down position	$V_I = V_{-snap\text{-}down}$

A parameter is defined to show the reduction in controlling voltage called the Figure of Merit (*FOM*). This parameter indicates the required voltage for the same displacement range equal to the displacement of the conventional displacement before snap-down (D_S), as shown below:

$$FOM = D_S / V_{snap\text{-}down} \quad (3.3)$$

Therefore, the larger the *FOM*, the smaller the controlling voltage required for each specific tri-electrode topology. Since the spacing in tri-electrode (D_1) is always compared to a conventional topology with the same D_1 gap spacings, the displacement value in the *FOM* definition is always equal to D_S. In the same way, the *FOM* for the conventional actuator (FOM_S) is:

$$FOM_S = D_S / V_S \quad (3.4)$$

As discussed earlier, the controlling voltage (V_I) can be either positive or negative. As opposed to the conventional topology, the behaviour of the actuator is not similar in the same positive and negative voltage values. Therefore, three different voltage situations are considered to study the tri-electrode performance, as defined below:

- Unipolar situation: In this case, the controlling voltage is entirely in the positive range from zero to $V_{+snap\text{-}down}$. The unipolar is shown in figure 3.7a for arbitrary parameter values of different gap spacings and electrode sizes. The non-filled circles show the actuator response in the unstable range and after the snap-down occurrence. They were kept in the curve to show the snap-down turning point more clearly. The controlling voltage (V_I) is called V_u, and the *FOM* is defined as $FOM = D_S / V_u$ when $V_I = V_u$.
- Bipolar situation: In this case, the controlling voltage is for when using a bipolar power supply of $\pm V_b$ voltage range (figure 3.7b). The *FOM* is defined as $FOM = D_S / V_b$ when $V_I = V_b$. The negative voltage helps us to reduce the absolute value of the controlling voltage of V_I. Furthermore, the other benefit of the bipolar power supply is neutralizing the trapped charges in the dielectric material close to the intermediate electrode [68].
- Maximum displacement situation: This case is for having a bipolar power supply for the maximum possible travel range from D_{min} to the D_{snap_down}. As shown in figure 3.7c, the maximum displacement is shown with Δd_{max}, and its corresponding required voltage is V_{max}.

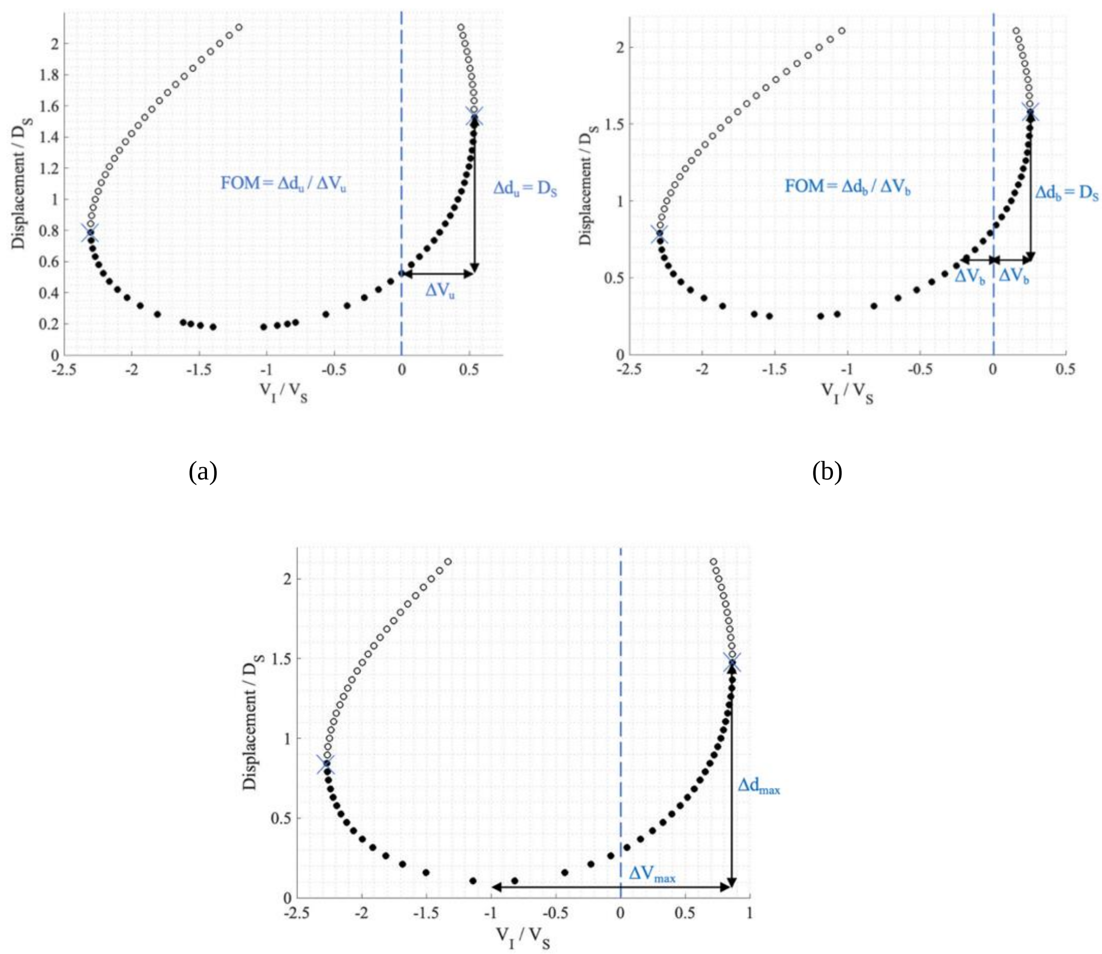

(a) (b)

(c)

Figure 3.7. The three different tri-electrode controlling voltage cases of (a) unipolar, (b) bipolar and (c) maximum displacement for an arbitrary tri-electrode configuration. All the three curves are also plotted in figure 3.8a to show the differences in displacements and voltages at snap-down.

The numerical simulations were performed to acquire the response curve of the tri-electrode for different parameters of W_S, W_E, and D_2 with respect to D_1 and also at different V_P and V_I. In all the cases of unipolar and bipolar, as mentioned the Δd is equal to D_S, to be able to compare with the conventional and discuss the progress in voltage reduction. However, there is only one V_P for each W_S, W_E and D_2 that the displacement is equal to D_S. Therefore, several simulations were performed repeatedly by sweeping V_I and V_P at each specific W_E, W_S and D_2 to find the required controlling voltage when the actuator travelled equal to D_S before snap-down. In each series of studies, the D_1 is fixed, and other parameters are determined with respect to that. The simulations continue to find the bias (V_P) needed for the actuator deflection equal to D_S. However, since sweeping the voltage to find the exact V_P for when the displacement is D_s, might be very time-consuming (performing with very small voltage steps), the simulations of finding V_P, stopped when the actuator reached $D_S \pm 2\%$.

In order to show the method of studies, the three cases are shown in figure 3.8a for an arbitrary tri-electrode configuration. In this case, the unipolar and bipolar displacements (Δd_u and Δd_b) are equal to D_S. The response curves were calculated for several V_P values, and the maximum possible displacement of the case is shown in figure 3.8b. This figure shows the displacements vs. V_P, and as highlighted, there is only one V_P for unipolar and bipolar cases, when the displacements are equal to D_S. Each value in figure 3.8b is shown with a 2% error bar, and the fitted curves using three different fitting functions are depicted in figure 3.8c.

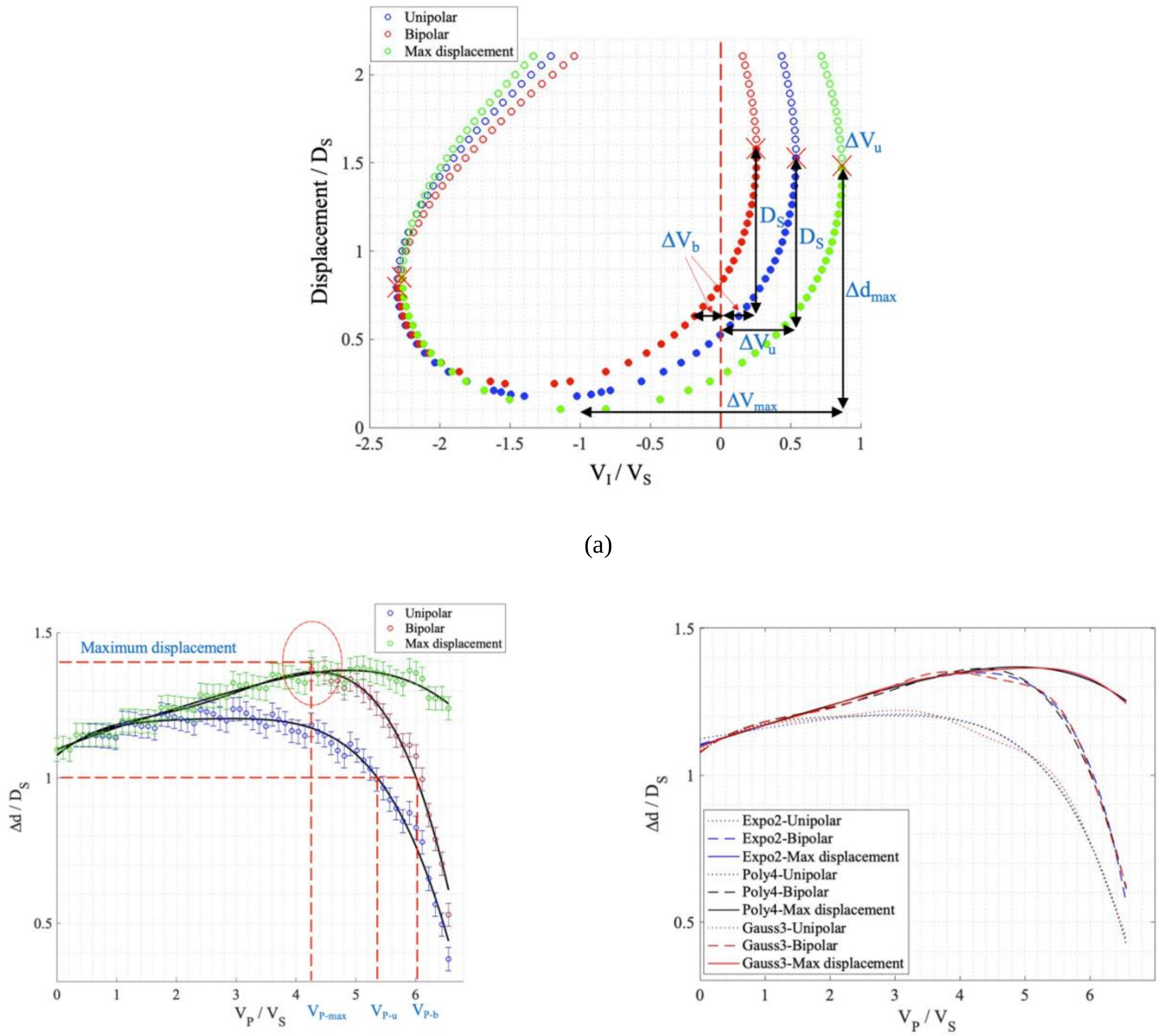

(b) (c)

Figure 3.8. The unipolar, bipolar and maximum modes of (a) displacement vs. V_I curves, (b) maximum travelled range vs. V_P, and (c) the fitted maximum travelled range vs. V_P curves using three different fitting functions.

3.4.5 Intermediate electrode width (W_E)

In this section, the effect of the intermediate electrode width on the actuator's performance is studied. During the studies, all the parameters are normalized to D_1 in order to be able to have a dimensionless solution. W_E was swept from 0.0167 D_1 to 2.5 D_1. The gap spacing (W_S) is fixed and equal to 2.5 D_1 and D_2 = 1.67 D_1. It was not desired to increase the W_E higher than 2.5 D_1 since, according to our initial studies, the gap spacing (W_S) smaller than the electrode width (W_E) mostly blocks the electric fields generated by the primary electrode and minimizes the overall electric field on the moving electrode. The studied response curves of unipolar, bipolar and maximum displacement are depicted in figure 3.9. Looking at the responses, the electrode width change mostly impacts the negative V_I range, while the positive voltages show slight changes. Also, the higher the V_P, the larger D_{min} is. Since, as we know, the larger V_P generates higher electric forces in the absence of V_I controlling voltage.

The *FOM* for both unipolar and bipolar vs. W_E are illustrated in figure 3.10. The *FOM* is normalized to FOM_S. We see that the *FOM* in tri-electrode is larger than FOM_S about two times for unipolar and about four times for bipolar. The improvement in FOM is mostly at $W_E < D_1$, and V_P increases by increasing the W_E for a fixed value of W_S.

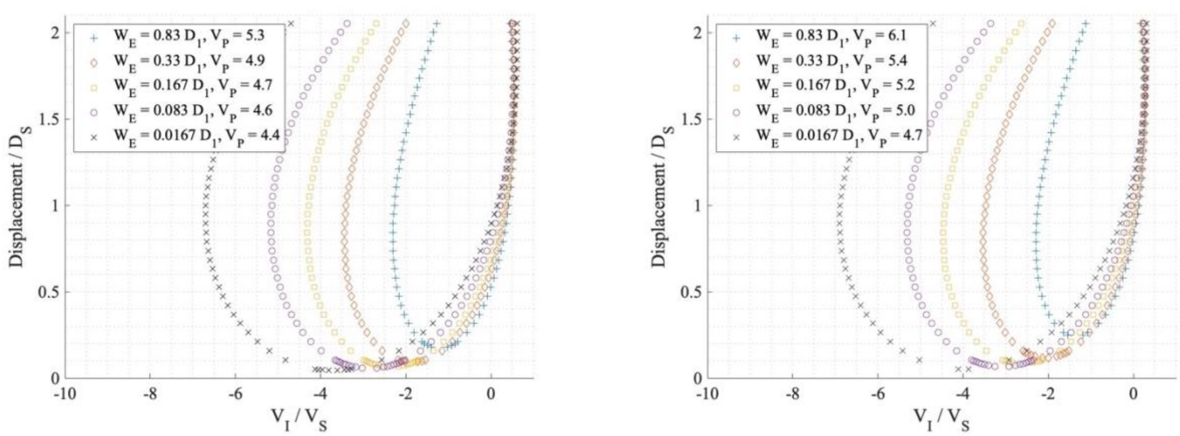

(a) (b)

Figure 3.9. Displacement vs. V_I for different W_E electrode widths when D_2 = 1.67 D_1 and W_S = 2.5 D_1 for (a) unipolar and (b) bipolar configurations.

Figure 3.11 shows the maximum displacement vs. W_E. In this case, the W_E was swept and the maximum possible travel range was measured for W_E = (0.0167 – 0.83) D_1. The larger the W_E, the smaller distance the actuator can travel before snap-down. Thus, we see that the maximum displacement (Δd_{max}) is inversely related to the electrode width. However, for the two cases of W_E = 0.83D_1 and 0.0167 D_1, the maximum displacements are equal to Δd_{max} = 1.4 D_S and 1.9 D_S, respectively, which are both significant improvements in travel range.

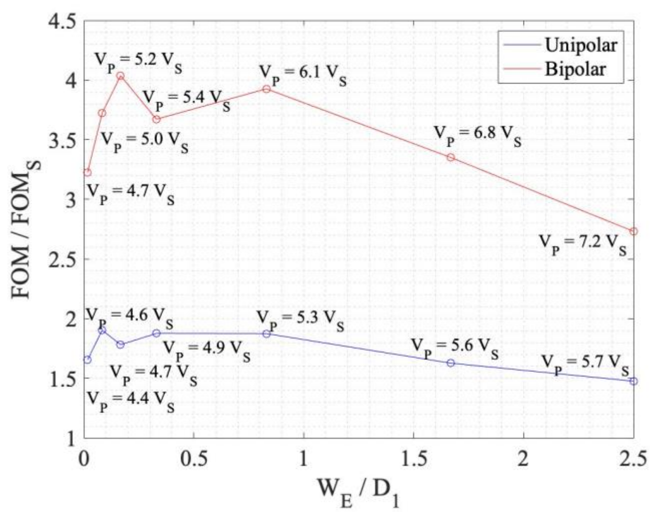

Figure 3.10. *FOM* vs. intermediate electrode width (W_E) for unipolar and bipolar systems (D_2 = 1.67 D_1 and W_S = 2.5 D_1).

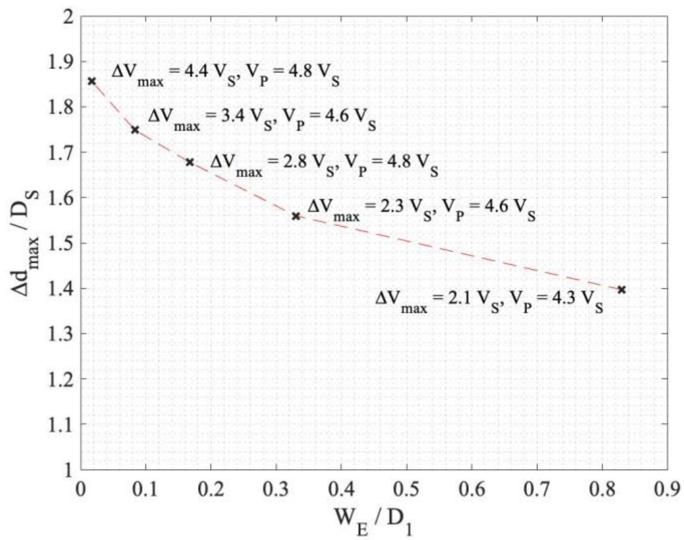

Figure 3.11. Maximum displacement (Δd_{max}) vs. intermediate electrode width (W_E) for unipolar and bipolar systems (D_2 = 1.67 D_1 and W_S = 2.5 D_1).

3.4.6 Intermediate electrode spacing (W_S)

The impact of the intermediate electrode spacings (W_S) is studied in this section. The spacing is normalized to D_1. The parameter W_S was varied from 1.0 D_1 to 4.0 D_1 for two widths of (W_E = 0.167 D_1) and (W_E = 0.83 D_1), in order to study the impact of electrode width and spacing simultaneously. The FOM for different spacings is shown in figure 3.12 when D_2 = 1.67 D_1. Looking at the curves, we see peaks for both W_E. The peak for unipolar and bipolar occurs at W_S = 2 D_1 and W_S = 2.5 D_1, respectively. Therefore, a conclusion would be that the spacings should not be too small to block the primary electrode electric fields, and not be too large to lose the intermediate electrode's contribution. Comparing two curves of W_E = 0.167 and 0.83 D_1, the narrower W_E provides a higher *FOM*. The maximum displacement vs. W_S is also depicted in figure 3.13 for both electrode widths.

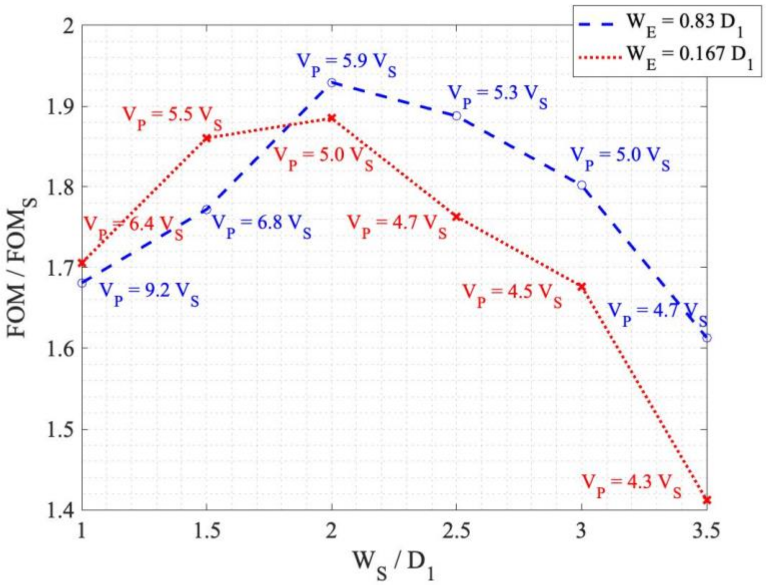

(a)

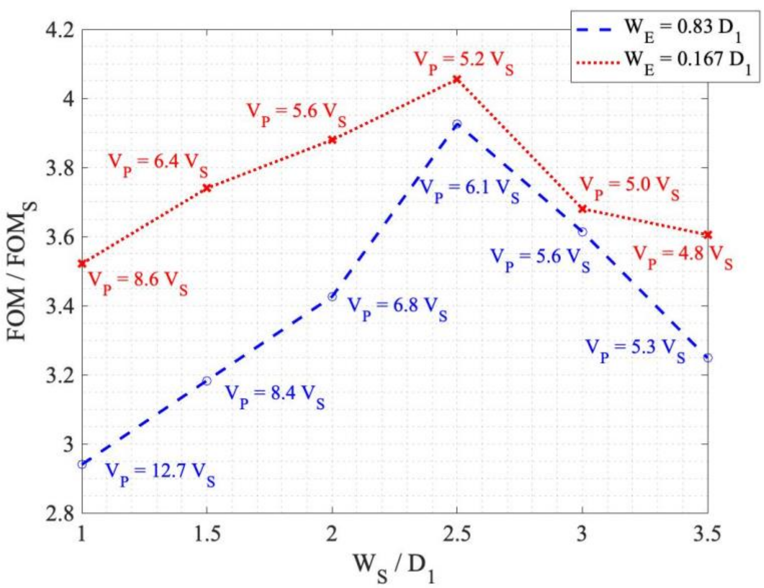

(b)

Figure 3.12. *FOM* vs. intermediate electrode spacings (W_S) for two different electrode widths ($W_E = 0.83\ D_1$ and 0.167 D_1 for (a) unipolar and (b) bipolar cases when $D_2 = 1.67\ D_1$.

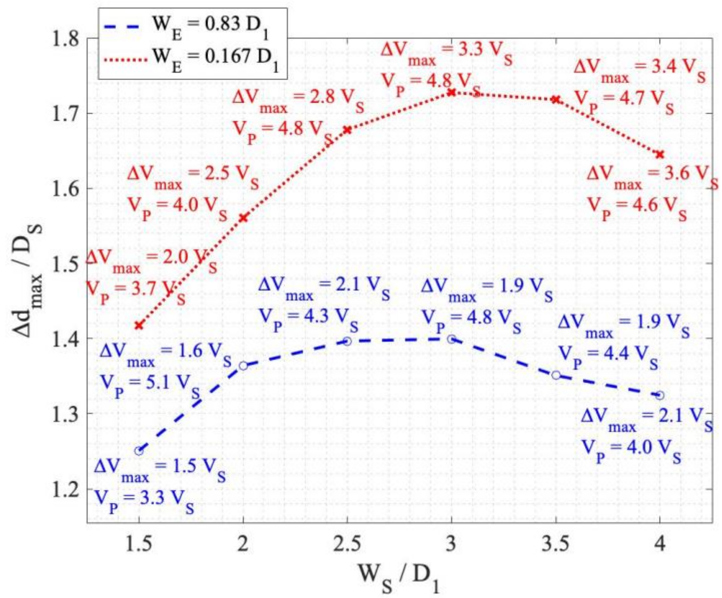

Figure 3.13. Maximum displacement (Δ_{max}) vs. intermediate electrode spacings (W_S) for two different electrode widths W_E = 0.83 D_1 and 0.167 D_1 for (a) unipolar and (b) bipolar cases when D_2 = 1.67 D_1.

Similar to the previous cases (unipolar and bipolar), the narrower electrode (W_E = 0.167 D_1) provides a better (more significant displacement) result compared to the W_E = 0.83 D_1. Comparing the two curves, we see that the maximum travel range before snap-down is Δd_{max} = 1.4 D_S for W_E = 0.83 D_1 and Δd_{max} = 1.7 D_S for W_E = 0.167 D_1.

3.4.7 Spacing between intermediate and primary electrodes (D_2)

One crucial parameter that affects the tri-electrode performance is the spacing between the stationary electrodes (D_2). The actuator performance (*FOM*) was studied for a range of D_2 = (1 – 2.67) D_1 and the results are displayed in figure 3.14. The intermediate electrode width and spacing resulting from the previous sections (W_E = 0.83 D_1, W_S = 2.5 D_1) were used. It was observed that the *FOM* increases by increasing the D_2 / D_1 ratio, but the increase rate is gradually reducing. However, a larger V_P is also required as the D_2 increases.

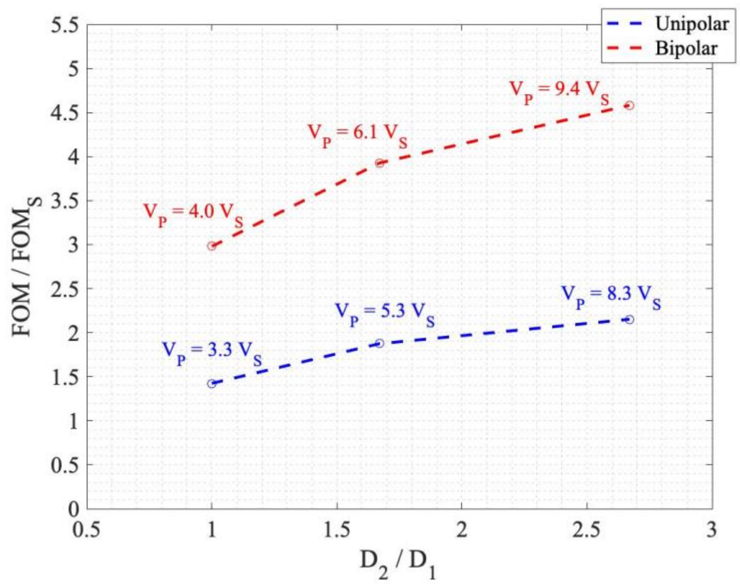

Figure 3.14. *FOM* vs. D_2/D_1 when W_S = 2.5 D_1 and W_E = 0.83 D_1 for unipolar and bipolar.

One important conclusion is that the D_2 / D_1 ratio should be larger than 1 to have an acceptable improvement in *FOM* and maximum displacement. According to our studies, the D_2 / D_1 ratio of 1.67 is an appropriate value for having a high enough *FOM* and an acceptable V_P value (not too high voltage). The reported studies here are a summary of numerous studies performed earlier, with additional studies summarized in Appendix A.

3.4.8 Conclusion

In this section (3.4), the impact of different parameters that significantly affect the tri-electrode performance were studied. The tri-electrode topology can have the same displacement as a conventional electrostatic actuator but for a considerably lower controlling voltage. Also, there is a mode in the actuator operation that the range of motion (before snap-down) in one case can be enhanced up to 70% more compared to that of a conventional topology. The improvement in range of motion can be enhanced even higher by having an extended primary electrode. The following sections will discuss this approach for improving travel range tri-electrode.

3.5 Extended electrode topology

As shown in the previous section, the tri-electrode topology is a valuable solution to reduce the controlling voltage and increase the limited travel range. Since the limited deflection range has been one of the main electrostatic actuator's issues, various solutions were introduced to overcome the pull-in effect which is the cause of the actuator's problem. One successful solution is the offset electrode concept [69-71]. Accordingly, an extended primary electrode was utilized to enhance the actuator's maximum displacement in the following [72].

3.5.1 Extended electrode design – response curve

Figure 3.15 shows the tri-electrode with an extended primary electrode topology. As explained before, the intermediate and primary electrodes' voltage polarity should be the same to have the tri-electrode operate in its enhancement mode. In the same way for the extended electrode, the primary electrode should have the same polarity as the intermediate to increase the maximum displacement range ($V_P > V_I > 0$).

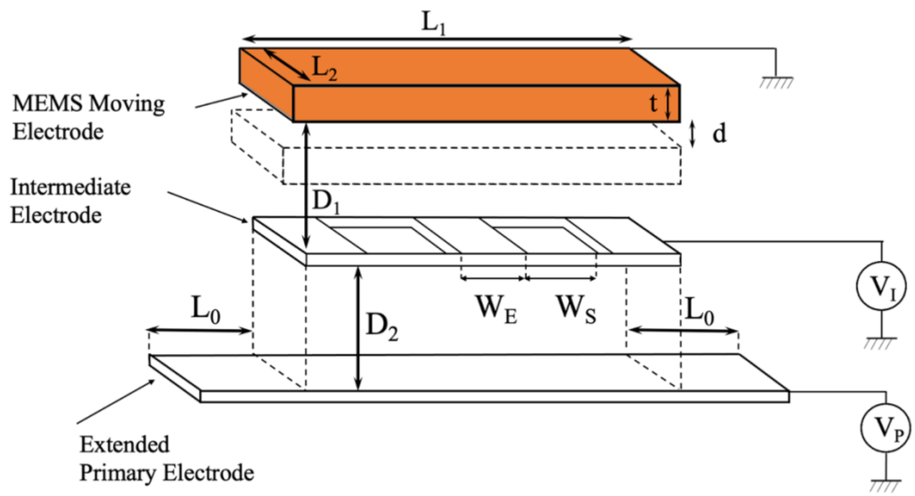

Figure 3.15. The 3D schematic of the extended electrode (tri-electrode) configuration. The extended section is equal to L_0 from two opposite sides of the primary electrodes.

Figure 3.16 shows the cross-section schematic of the non-extended and extended design including the electric fields between the electrodes. As shown, the extended section of the primary electrode (L_0) generates fringing fields that reach to the top surface of the moving electrode and provide lifting forces. This lifting electrostatic force fights against the attractive pulling force on the other side of the moving electrode and can cause increase in the controllable moving range of the actuator.

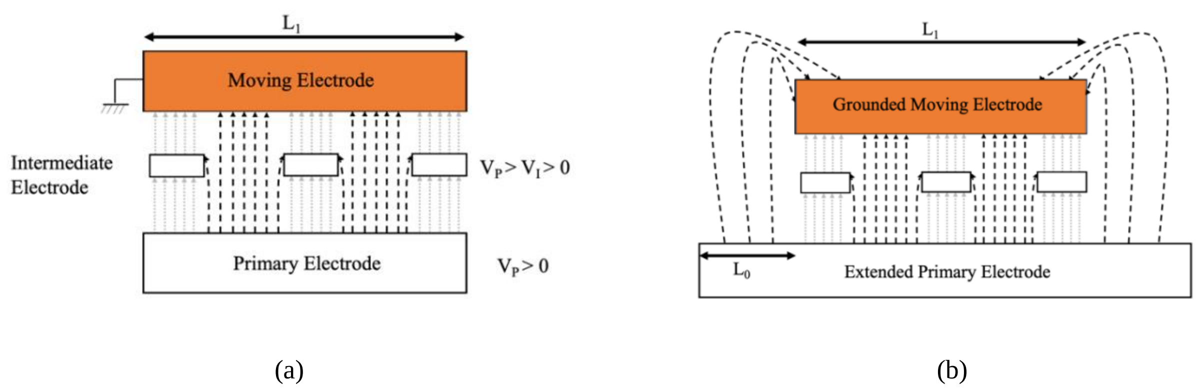

Figure 3.16. Tri-electrode configuration cross-section schematic with electric fields distributions for (a) non-extended primary electrode and (b) extended primary electrode.

The fringing fields (lifting forces) are not only important in increasing the actuator's deflection range, but the ratio of the lifting forces to the pulling forces are also a significant parameter. Since most of the fringing fields reach to the top edge of the moving electrode, designing a narrow moving electrode can help to increase the ratio of the electric fields contributing to the lifting force compared to the pulling force. Therefore, a narrow actuator is designed to show the increase in the maximum displacement of the tri-electrode. The dimensions of the actuator are $W_S/D_1 = 3$, $W_E/D_1 = 0.17$, $D_2/D_1 = 1.7$, $L_1/D_1 = 6.5$, $L_2/D_1 = 67$ and $V_P/V_S = 5.2$ where $D_1 = 6$ µm. The extended part of the primary electrode is $L_0/ D_1 = 13$. These dimensions are chosen to show the improvement in the maximum displacement range compared to the conventional and tri-electrode configuration. However, each of the parameters will be discussed in the following sections. The response curve of the tri-electrode with non-extended primary electrode (blue diamond curve) and the conventional topologies (purple cross curve) are depicted in figure 3.17a and the response for the extended electrode (black star curve) is shown in figure 3.17b.

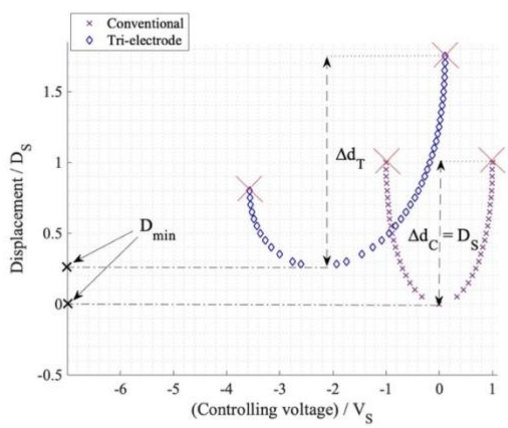

(a)

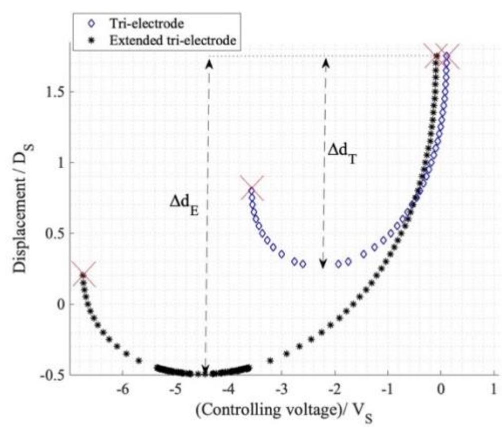

(b)

Figure 3.17. Response curves of the conventional, and tri-electrode with and without extended electrode. (a) Tri-electrode and conventional response curve for when $W_S/D_1 = 3$, $W_E/D_1 = 0.17$, $D_2/D_1 = 1.7$, $L_1/D_1 = 6.5$, $L_2/D_1 = 67$, $L_0/D_1 = 13$ and $V_P/V_S = 5.2$. (b) Tri-electrode with and without extended electrode response curves.

Comparing the results for conventional and tri-electrode in 3.17 we see that the tri-electrode maximum displacement (Δd_T) is almost 50% larger (Δd_T =1.5 D_S) than the conventional topology displacement before snap-down (D_S). The maximum displacement for the extended electrode configuration (Δd_E) is 50% larger than the tri-electrode (Δd_E = 1.5 Δd_T) and 2.3 time larger than the conventional (Δd_E = 2.3 D_S). Thus, we see that the extended electrode topology can increase the maximum displacement even 50% more than the tri-electrode. In this study, the thickness, and the air box size at the top of the moving electrode are determining parameters on the actuator performance. Therefore, each will be studied in the following sections. The thickness of the moving electrode and the air box height in the study illustrated in figure 3.17 were t = 0.017 D_1 and L_4 = 16.7 D_1, respectively.

As it was explained, the narrow moving electrode will be helpful to increase the impact of the extended electrode. Therefore, a very narrow actuator was also designed and studied to see the impact of the narrowness of the moving electrode comparing the narrow and very narrow configurations in the following section.

3.5.2 Narrow and very narrow moving electrodes

The narrow and very narrow actuators are shown in figure 3.18. Both actuators have the same dimensions except the width which for narrow actuator, the length is L_1 = 16 D_1 and for very narrow actuator, the length is L_1 = 6.5 D_1. The narrow actuator has six solid electrode parts as its intermediate electrode and the very narrow actuator has three. The similar dimensions for both are as W_S = 0.17 D_1, W_E = 3 D_1, D_2 = 1.7 D_1 and L_0 = 3.3 D_1. The moving electrode thickness is t = 0.017 D_1 and the heigh of the air-box above the moving electrode is L_4 = 67 D_1. In order to have the same pulling force per unit area from the underlying electrodes for both narrow and very narrow actuators, the spring constant is scaled with the actuators' widths. The maximum displacement for both cases is shown in figure 3.19. As can be seen, the very narrow actuator has almost 15% higher displacement before snap-down ($\Delta d_{max\text{-}narrow}$ = 1.76 D_S, $\Delta d_{max\text{-}very\ narrow}$ = 2.02 D_S).

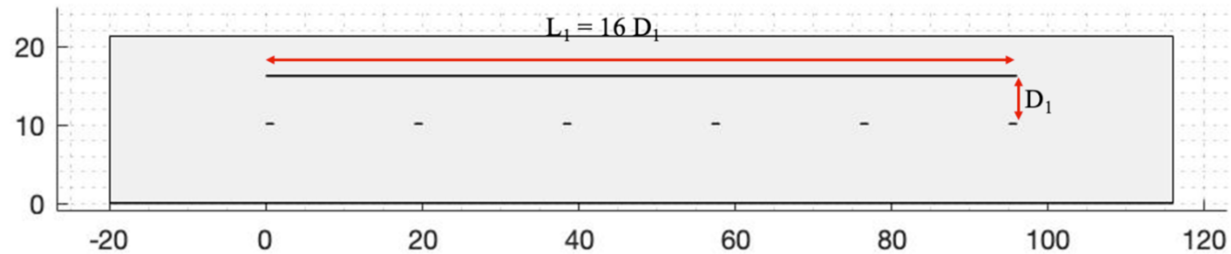

(a)

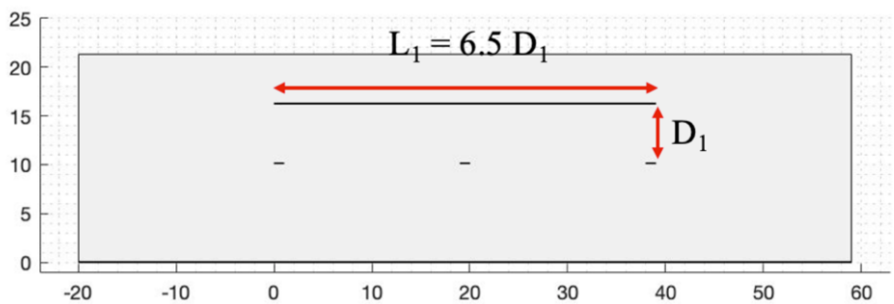

(b)

Figure 3.18. The 2D schematic of the extended electrode with (a) narrow (L_1 = 16 D_1) and (b) very narrow (L_1 = 6.5 D_1) configurations when W_S = 0.17 D_1, W_E = 3 D_1, D_2 = 1.7 D_1, L_0 = 3.3 D_1 and L_4 = 67 D_1.

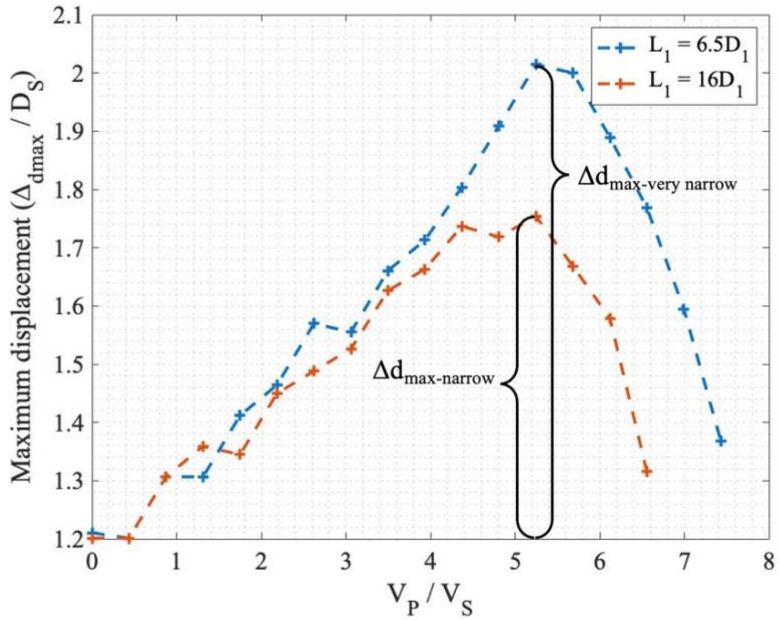

Figure 3.19. Maximum displacement vs. V_P for narrow and very narrow configurations.

The study of the narrow and very narrow actuators for a single biasing value showed that the narrower the actuator, the higher range of motion. Therefore, both actuator's performance at different L_0 and V_P in the following section are studied.

3.5.3 L_0 effect study

The maximum displacement (Δd_{max}) was studied for both narrow and very narrow electrode actuators for a range of L_0 = (0 – 25) D_1 and the results are shown in figure 3.20. The L_0 at a specific V_P was swept each time and the Δd_{max} was calculated. Each single value in figure 3.20, corresponds to an actuator response curve at a specific L_0 and V_P. Looking at curves, we see that the maximum displacement increases by extending the primary electrode (L_0) and this trend is more apparent at V_P >3.5 V_S. Since all the curves are almost flatten at L_0 >10 D_1, this amount of extension can be an acceptable extension if we also consider the actuator compactness. In the very narrow actuator (figure 3.20a), the maximum displacement with extended electrode (L_0 = 10 D_1) is almost 90% larger (Δd_{max} ~ 2.3 D_S) than the non-extended electrode topology (Δd_{max} ~ 1.2 D_S) when V_P = 6.1 V_S. For the same V_P, the maximum displacement for the narrow actuator is not more than almost 50% which is smaller than the very narrow actuator. Here, we again see that the very narrow actuator provides a higher maximum displacement.

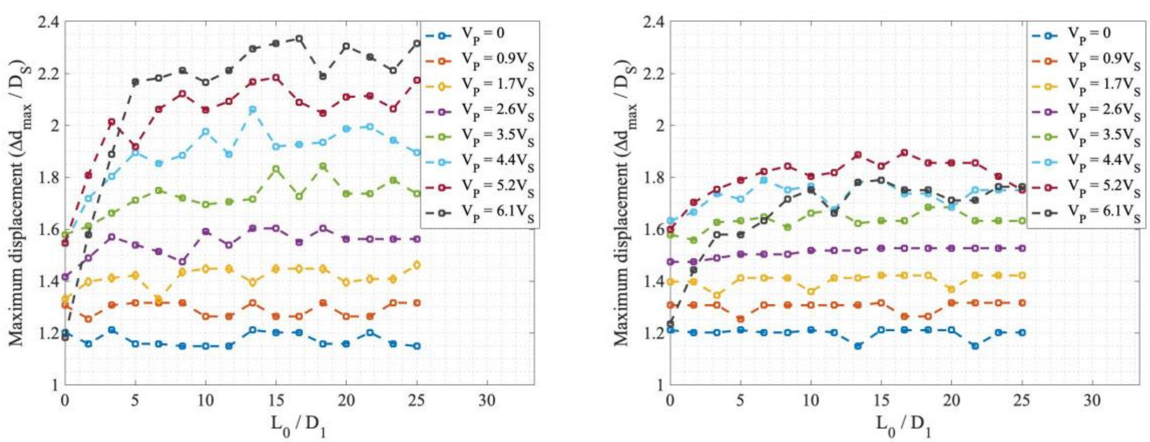

(a) (b)

Figure 3.20. Maximum displacement vs. L_0 at different V_P value (0 – 6.1 V_S) for (a) narrow actuator (L_1 = 16 D_1) and (b) very narrow actuator (L_1 = 6.5 D_1).

It is also worth mentioning that the displacement in figure 3.20 increases at larger V_P, but the increase stops at a specific V_P and then start falling. This can be seen in figure 3.20b that the maximum displacement at V_P = 6.1 V_S is smaller than at V_P = 5.2 V_S at any L_0 value. For the vary narrow actuator (figure 3.20.a) this increasing trend stops at V_P > 6.1 V_S.

Figure 3.21 shows the displacement vs. controlling voltage response curves for non-extended (L_0 = 0) and extended (L_0 = 13.34 D_1) tri-electrode of the narrow actuator at V_P = 0 – 6.1 V_S. The Δd_{max} increases from V_P = 0 to 4.4 V_S and then start decreasing. However, the Δd_{max} in the extended actuator continually increases by increasing the V_P. The reason is due to the extended part of the primary electrode. It shows that the extended actuator enhances the total maximum displacement by providing a controllable displacement in the opposite direction. This behaviour also confirms that the lifting force overcomes the electrostatic attracting force and turns the actuator to a bi-directional electrostatic actuator.

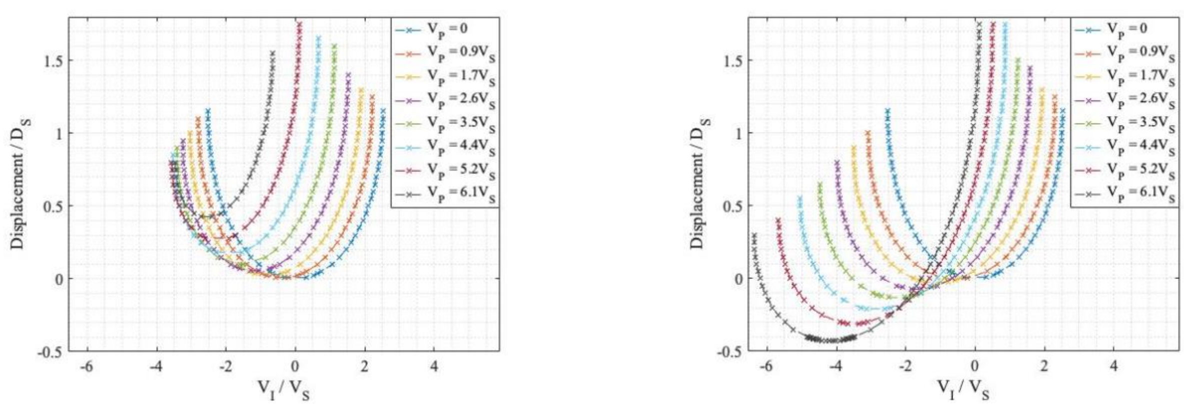

(a) (b)

Figure. 3.21. Response curve of the narrow actuator at V_P = 0 – 6.1 V_S at (a) non-extended actuator (L_0 = 0) and (b) extended actuator (L_0 = 13.34 D_1).

3.5.4 The effect of air-box

It was mentioned earlier that the space above the moving electrode has a significant influence on the actuator performance, with the higher free space above the moving electrode resulting in less electric field being blocked. Figure 3.22 shows the very narrow actuator with the free space height is defined by L_4. The area encompassing and located above the electrodes is regarded as the designated air-box. As shown, the impact of the extended part of the primary electrode is on the actuator's movement in the opposite direction. Thus, the impact of the maximum displacement can be explored by looking at the D_{min} of the response curves. L_4 was swept from $L_4 = 0.8\ D_1 – 3.3\ D_1$ and the response curves are plotted in figure 3.23a for when $V_P = 5\ V_S$ and $L_0 = 25\ D_1$. The D_{min} vs. L_4 is also depicted in figure 3.23b. Looking at figure 3.23b, we can see that D_{min} curve is almost flat for $L_4 > 10\ D_1$ which is almost $5(D_1+D_2)$. This height was always used in the previous studies to maximize the effect of extended electrode.

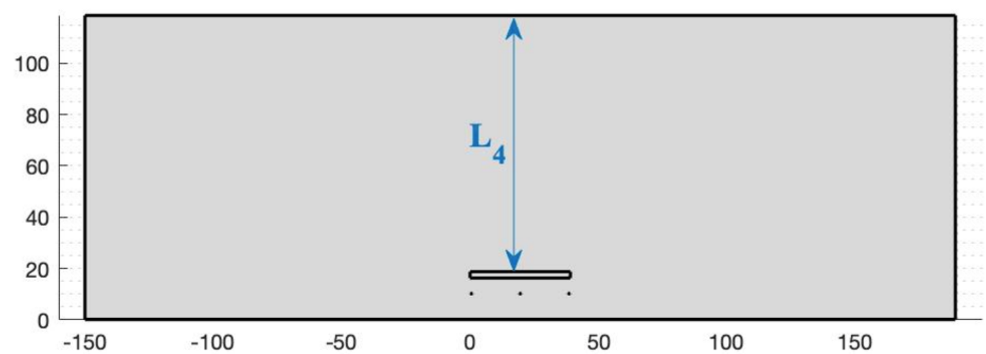

Figure 3.22. The 2D schematic of the very narrow extended tri-electrode actuator with L_4 height of air-box above the moving electrode.

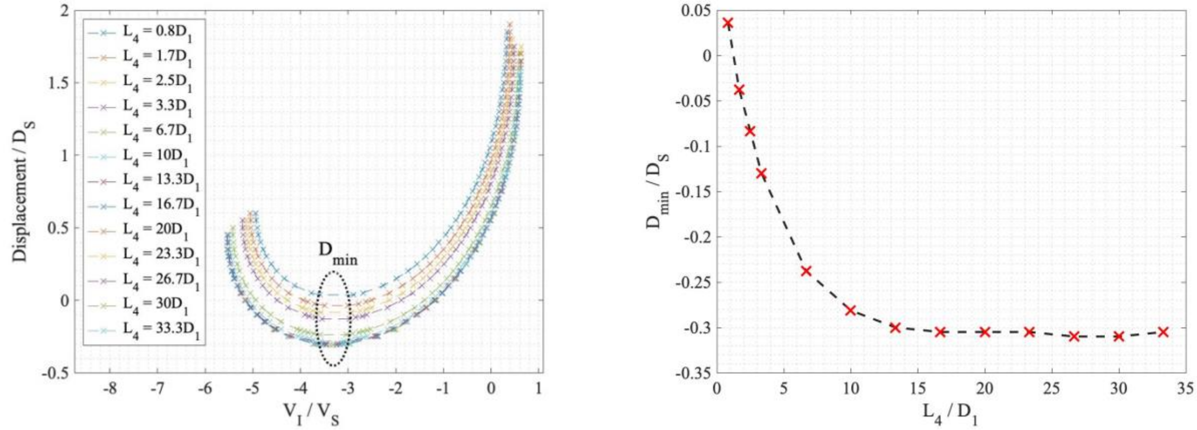

(a) (b)

Figure 3.23. (a) Displacement vs. controlling voltage at L_4 = (0.8 – 33.3) D_1 and (b) D_{min} vs. L_4 for the same L_4 range.

3.5.5 The effect of moving electrode thickness

The thickness of the moving electrode is a significant parameter affecting the lifting force generated by the extended electrode (figure 3.24). The parameter D_{min} was plotted for D_{min} vs. L_0 (0 – 25D_1) at different electrode thickness of t = (0.0017 – 1.7) D_1 for the same L_4 and V_P of the previous section. As depicted in figure 3.25, the thinner the electrode, the larger absolute value of D_{min} at a specific L_0. It also can be recognized that D_{min} does not increase significantly when electrode is thinner than 0.0017 D_1.

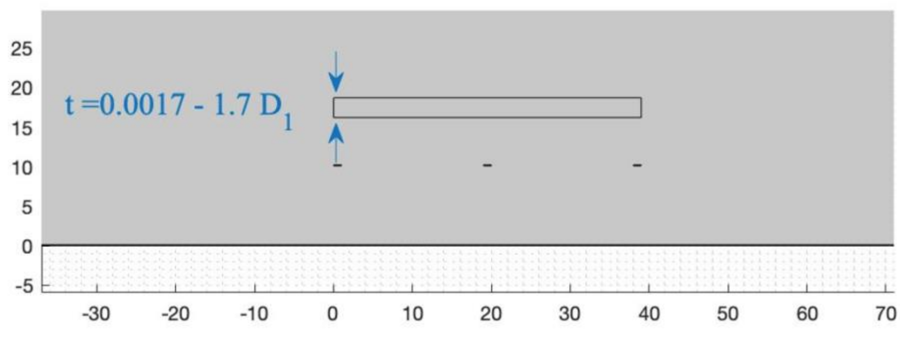

Figure 3.24. The 2D schematic of the very narrow extended tri-electrode actuator with moving electrode thickness of t.

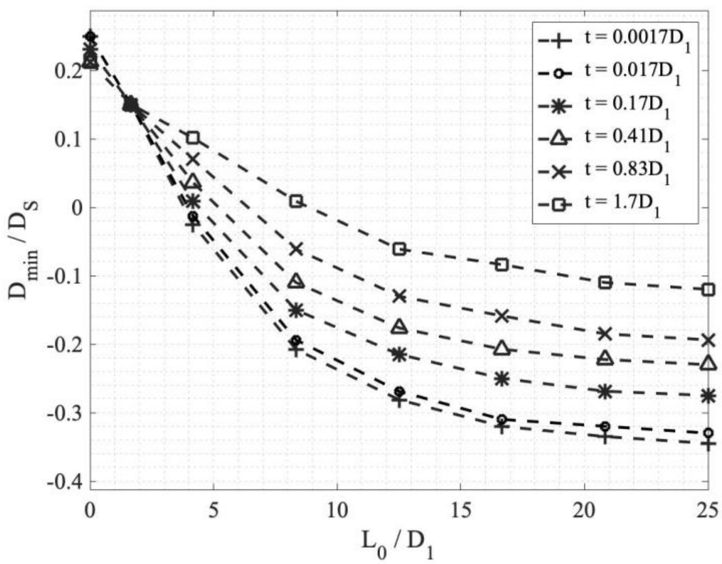

Figure 3.25. D_{min} vs. L_0 for t = (0.0017 – 1.7) D_1.

3.6 The D_2 spacer material effect

The previous studies showed that the tri-electrode is an appropriate solution to reduce the controlling voltage and travel range. The extended electrode configuration is also very useful to increase the maximum displacement employing the fringing fields. In both designs, there is free space between intermediate and primary electrodes. However, using a solid material can help to simplify the fabrication procedures. Thus, the impact of using solid materials (SU-8 and glass) with different dielectric constants was studied [73].

The unit-cell using a solid material in D_2 is shown in figure 3.26. First, a study was done for using glass as the spacer material between the stationary electrodes at different D_2 sizes (D_2 = 1.7, 2.5, 4.2 D_1) when W_E = 0.83 D_1, W_s = 2.5 D_1, and the intermediate electrode thickness is as the same as the electrode thickness in section 3.4. The results of the studies are summarized in table 3.3.

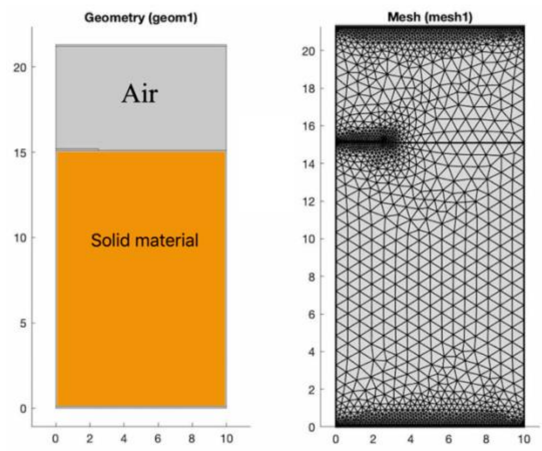

Figure 3.26. Unit-cell including a solid material in the space between stationary electrodes.

Table 3.3. Studying the *FOM* and maximum displacement when D_2 = 1.7, 2.5, 4.2 D_1, W_E = 0.83 D_1 and W_S = 2.5 D_1, with glass (ε_r = 4.2) in the D_2 region.

D_2	FOM_u / FOM_S	FOM_b / FOM_S	Max disp. / D_S
4.2 D_1	1.7 (V_P = 4.7 V_S)	2.9 (V_P = 5.7 V_S)	1.24 (V_P = 3.2 V_S)
1.7 D_1	1.3 (V_P = 2.1 V_S)	2.2 (V_P = 2.7 V_S)	1.18 (V_P = 1.5 V_S)
2.5 D_1	1.4 (V_P = 2.8 V_S)	2.6 (V_P = 3.7 V_S)	1.19 (V_P = 1.4 V_S)

Looking at table 3.3, we see that the thicker the solid material (D_2), the larger *FOM* for both unipolar and bipolar. The maximum displacement is also larger for the thicker spacer material. However, the corresponding V_P is also lager. The studies were carried out at one specific electrode gap spacing (W_s = 2.5 D_1) but more investigations were done to find the optimum spacing not only for glass, but also for another material such as SU-8 that is common in microfabrication. Therefore, it will help to compare the impact of two different solid materials. *FOM* is depicted for both unipolar and bipolar systems (D_2 = 4.2 D_1) in figure 3.27 when there is glass or SU-8 as spacer material in D_2 region and W_E = 0.83 D_1. The *FOM* for air is also depicted in figure 3.27 when D_2 = 1.67 D_1.

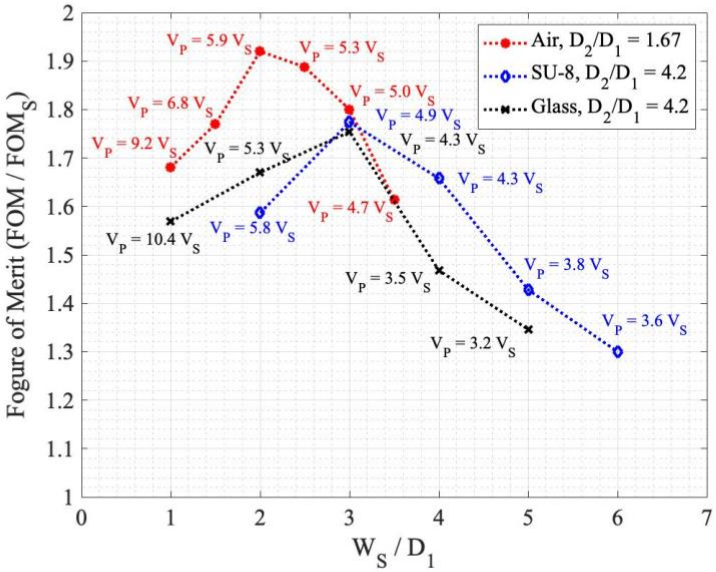

(a)

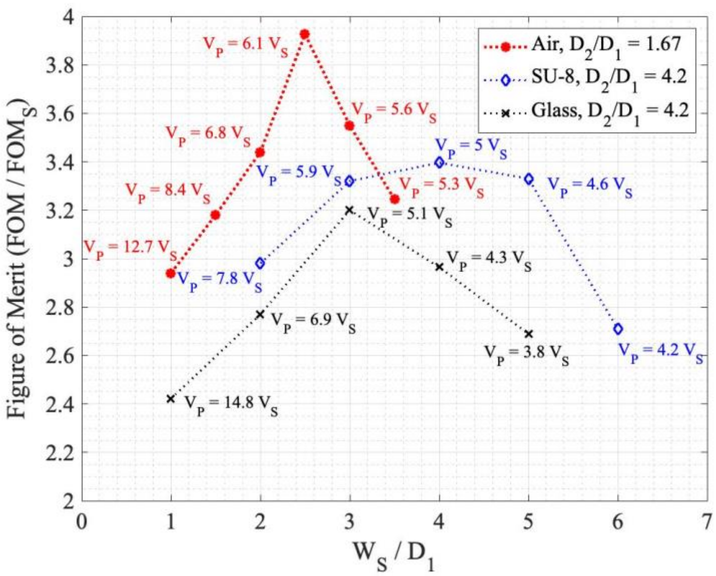

(b)

Figure 3.27. *FOM* vs. W_S when there are air, SU-8 and glass at D_2 region for (a) bipolar and (b) unipolar cases.

Looking at figure 3.27a, we see that the unipolar *FOM* is maximum and about 1.75 FOM_S for both SU-8 and glass materials at W_S = 3 D_1. The bipolar *FOM* is higher, and its maximum is equal to about 3.4 FOM_S for SU-8 at W_S = 4 D_1 and about 3.2 FOM_S for glass at W_S = 4 D_1. However, the *FOM* performance for the situation with air in the D_2 region is a little larger, but occurs at W_S /D_1 ratios that are a little smaller than the SU-8 and glass filled D_2 region cases. It is ~10% larger for the unipolar case occurring at W_S = 2 D_1, and about 15% larger for the bipolar case occurring at W_S = 2.5 D_1. It is interesting to note that at the same W_S /D_1 ratios of the peak performing SU-8 and glass materials, the *FOM* performance of the case for the air filled D_2 region is similar to that of the SU-8 and glass materials. Overall, it can be concluded that it is possible to use materials other than air to have a reduction in controlling voltage, with the best performing designs needing a larger D_2 than for the air filled D_2 situation.

4

Design and Microfabrication of Tri-electrode Actuators

Contents

4.1 Introduction

This chapter consists of two main sections. In the first section, tri-electrode topologies for two moving MEMS electrodes are designed and reported. The designed specifications were established according to the available materials and fabrication limitations.

In the second section, the microfabrication steps for these actuators are described. The majority of the steps are identical for both square and rectangular shape actuators; thus, the steps are detailed in one section and the second design fabrications were added in the following sections. The fabrication of either of the actuators consists of two parts. One is using a silicon wafer to build the moving MEMS electrodes, and the other part is coating and patterning the fixed electrodes on a quartz wafer. Each of the fabrication steps is reported in different sections.

4.2 Tri-electrode configuration

As shown in figures 4.1 and 4.2, the tri-electrode actuators which were built, consist of one moving square/rectangular MEMS electrode above intermediate and primary electrodes. A quartz wafer is used as the spacer material between the fixed controlling intermediate and primary electrodes. The solid quartz material was used to simplify the fabrication.

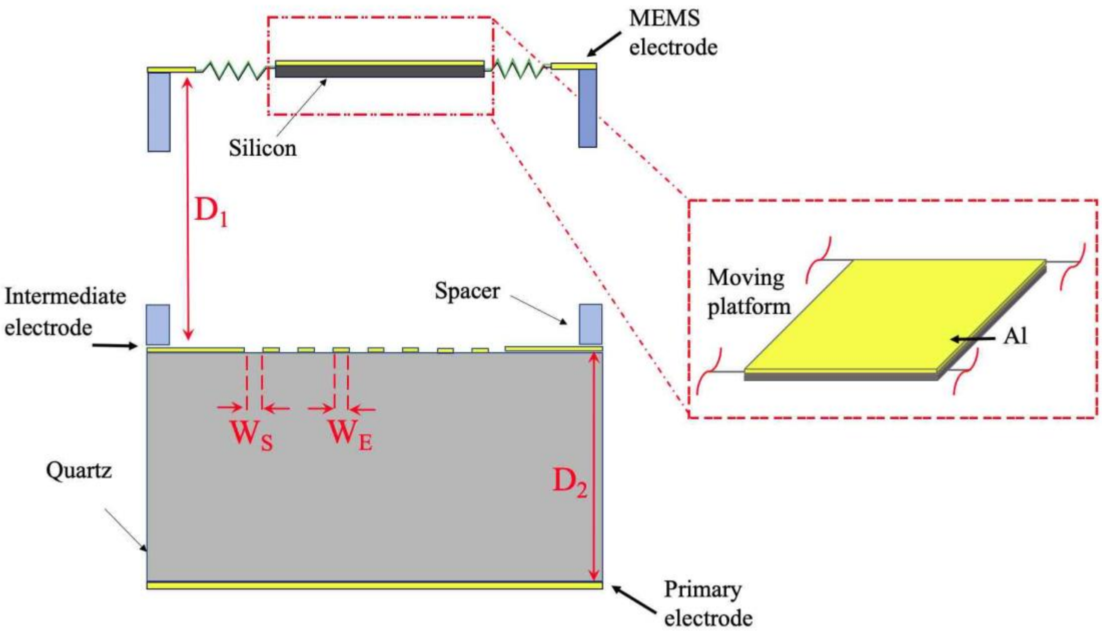

Figure 4.1. 2D Tri-electrode (square platform) schematic including MEMS moving electrode and using quartz as the material between the intermediate and primary electrodes.

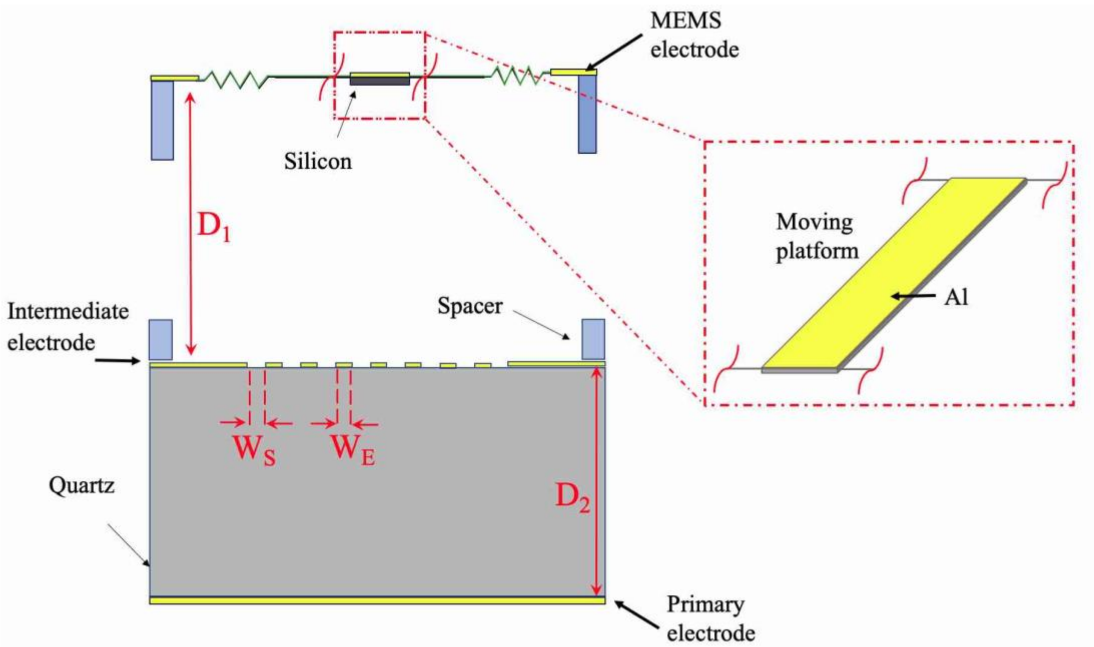

Figure 4.2. 2D Tri-electrode (rectangular platform) schematic including MEMS moving electrode and using quartz as the material between the intermediate and primary electrodes.

4.2.1. Tri-electrode configuration - square MEMS design

The design steps started by choosing a 500 µm thick quartz wafer as the material between intermediate and primary electrodes. Therefore, the gap between the intermediate and the primary electrodes (D_2) is equal to the quartz thickness. In the next step, the MEMS moving electrode platform size and supporting springs were designed, with the spring flexibility considered in accordance with the voltage range of the available power supplies that would cause the displacement in the experiments. After studying several versions, the square MEMS electrode of figure 4.3 was designed. In summary, various design criteria were taken into account during the development process, such as the type of springs employed, compact design, the number of turns in the serpentine spring, and the use of a long beam to minimize the impact of the underlying electrodes on the springs. The square electrode is suspended via four serpentine springs. The MEMS electrode dimensions are summarized in table 4.1. The MEMS (platform and supporting springs) should be designed first, as knowledge of the MEMS stiffness is required for the design of the tri-electrode. More details regarding the FEM mesh analysis and studying the linearity of the designed springs of the moving MEMS electrodes are reported in appendix B.

The moving MEMS platform size was chosen to be almost equal to 6.7×6.7 mm^2 to increase the attractive electrostatic force and reduce the corresponding required voltage. The serpentine springs were designed to be adequately far from the moving square platform and underlying electrodes, minimizing any attractive electrostatic force.

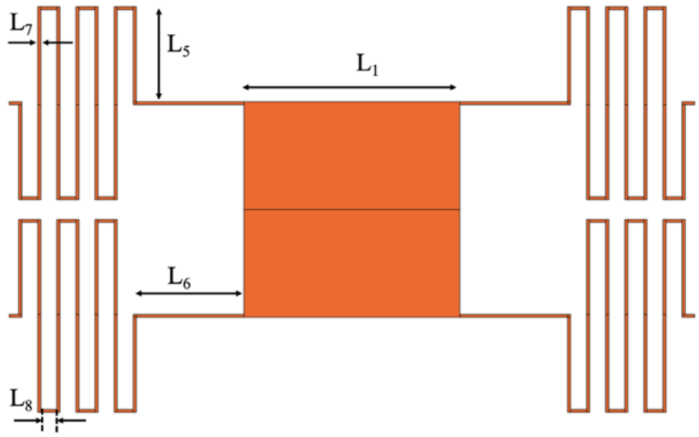

Figure 4.3. Top view of a 3D-designed MEMS moving electrode (square) for the tri-electrode topology.

Table 4.1. The dimension of the designed MEMS moving electrode.

Parameters	Values (μm)
L_1	6666
L_5	2910
L_6	3933
L_7	90
L_8	500
t (thickness)	40

Best figure of merit design:

According to the studies from chapter 3, the gap spacing between the MEMS electrode and the intermediate electrode (D_1) should be smaller than the distance between the intermediate and primary electrodes (D_2). We also know from section 3.6 that the larger the dielectric constant of the material used in region D_2 between the intermediate and primary electrodes, an increasing material thickness is required compared to a material with a lower dielectric constant. According to the study of section 3.6, it was shown that for a material with a dielectric constant in the range of ε_r = 3-5 (quartz has ε_r = 3.8), a ratio of D_2/D_1 = 4-5 gives the best figure of merit performance for the tri-electrode actuator, for W_S in the range of 3-4 times D_1. Therefore, since the quartz material is 500 µm thick, D_1 = 100 µm was chosen.

Simulations were performed for the tri-electrode design values (D_1 = 100 µm, D_2 = 500 µm and ε_r = 3.8) in order to acquire the maximum *FOM* for both unipolar and bipolar modes and their corresponding V_P. The results found W_S = 3 D_1 = 300 µm to give the best performance, as shown in Figure 4.4. The *FOM* for unipolar and bipolar are almost 1.45 and 3, respectively. The size of the intermediate electrode width (W_E) was chosen according to the results from section 3.4.6 (W_E = 0.167 D_1 = 16.7 µm).

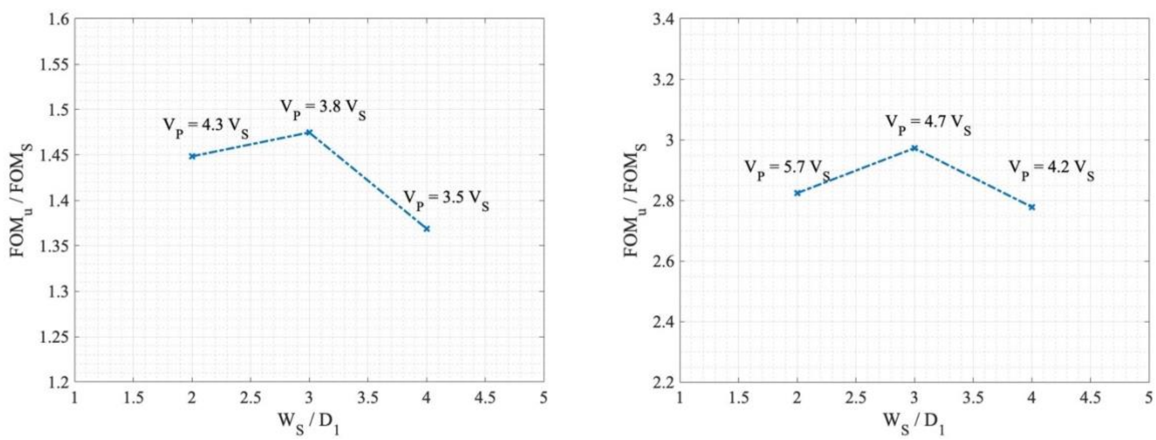

(a) (b)

Figure 4.4. *FOM* vs. W_S when (ε_r = 3.8, D_2 /D_1 = 5, W_E = 0.167 D_1 and D_1 = 100 µm) for (a) unipolar and (b) bipolar modes.

Best maximum displacement design:

For this device design, the maximum displacement possible before snap-down was simulated and it was found to be ~ 1.34 D_S., achieved with a primary electrode voltage of V_P = 4.4 V_S. However, the spacing for W_S and W_E that gives the best figure of merit, is not necessarily the same as that which would give the best maximum displacement possible before snap-down. In order to investigate this, more studies were carried at different values of W_S. Figure 4.5 summarizes these studies, with the corresponding V_P needed to achieve best displacement at each W_S. It can be seen that the maximum displacement possible increases with increasing W_S until about W_S = 4.5 D_S. Therefore, a second MEMS experimental device was designed with W_S = 450 µm to investigate the performance.

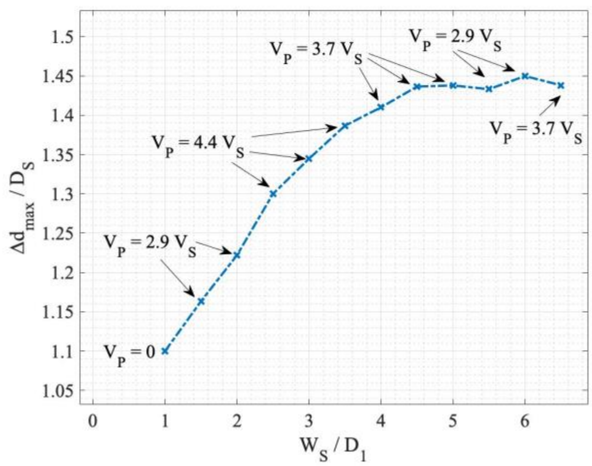

Figure 4.5. Maximum Displacement vs. W_S for (ε_r = 3.8) at D_2 / D_1 = 5, W_E = 0.167 D_1 and D_1 = 100 µm.

Design summary:

Table 4.2 summarizes the design parameters for the two square MEMS experimental devices.

Table 4.2. Tri-electrode topology parameters

Parameters	Values
D_1	100 µm
D_2 (quartz)	500 µm
W_E	16.7 µm
$W_{S\ best\ FOM}$	300 µm
$W_{S\ best\ displacement}$	450 µm

4.2.2. Tri-electrode configuration - rectangular MEMS design

A narrow rectangular MEMS was designed to test the tri-electrode topology in a compact configuration. Figure 4.6 shows the schematic of the rectangular narrow moving electrode. The electrode dimensions are summarized in table 4.3.

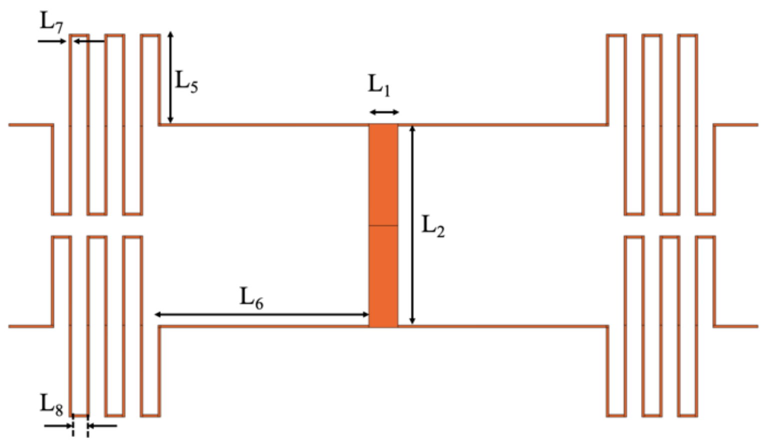

Figure 4.6. Top view of a 3D-designed MEMS moving electrode (recangular) for the tri-electrode topology.

Table 4.3. The parameters and their values utilized in the numerical simulations of the narrow MEMS electrode.

Parameters	**Values (µm)**
L_1	950
L_2	6666
L_5	2910
L_6	6790
L_7	90
L_8	500

Compared to the square MEMS design, the spring beam L_6 was made longer so that the final device size was the same as the square MEMS design. In this way, it made the etch mask design (which will be discussed later in this chapter) the same for both the square and narrow MEMS devices. For this narrow design, the intermediate electrode gap spacing of W_S = 450 µm was used.

4.3 Mask preparation

The schematic of the tri-electrode and the designed masks for each of the electrodes are illustrated in figures 4.7 and 4.8. Three transparent UV lithography masks were ordered from the nano fabrication lab at the University of Alberta, as illustrated in figures 4.9 and 4.10. A mask set for a square moving electrode (ACT-1) is to test the performance of the square tri-electrode topology, for two different intermediate electrode gap spacings of 300 and 450 µm are designed in masks. The other mask set (ACT-2) is to test the performance of the narrow rectangular MEMS tri-electrode topology.

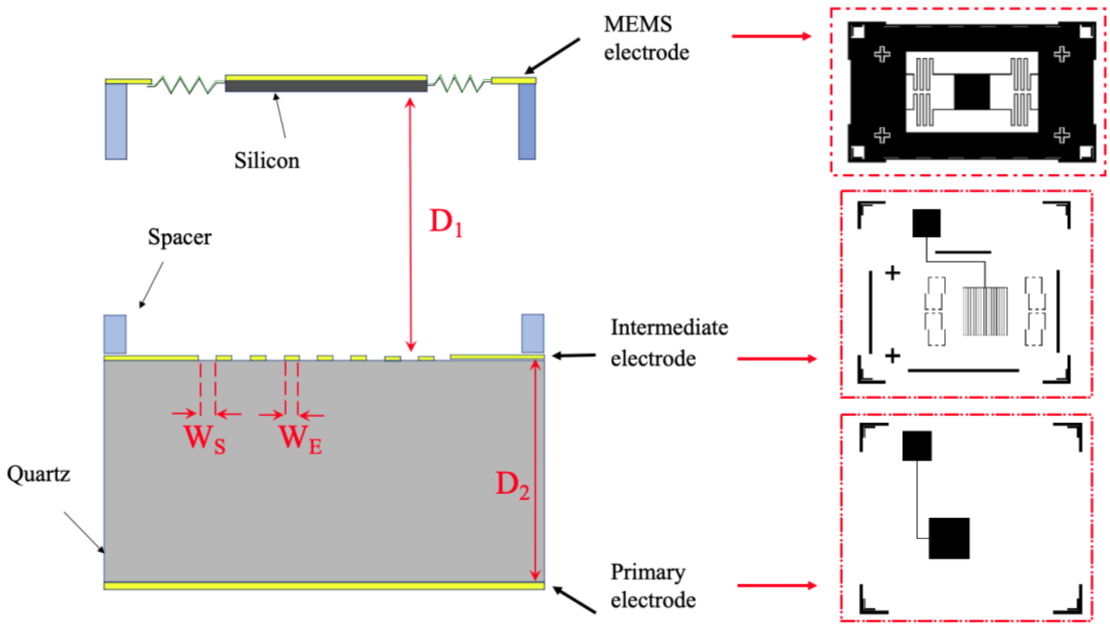

Figure 4.7. 2D Tri-electrode design and masks for square MEMS platform, including all the three electrodes and the corresponding designed masks.

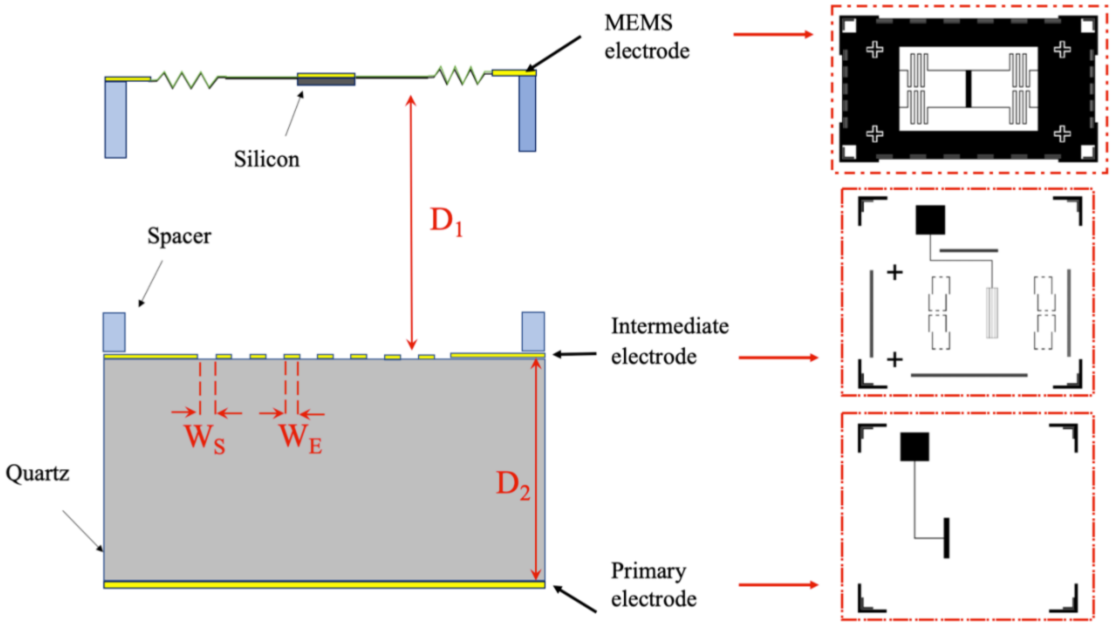

Figure 4.8. 2D Tri-electrode design and masks for narrow rectangular MEMS platform, including all the three electrodes and the corresponding designed masks.

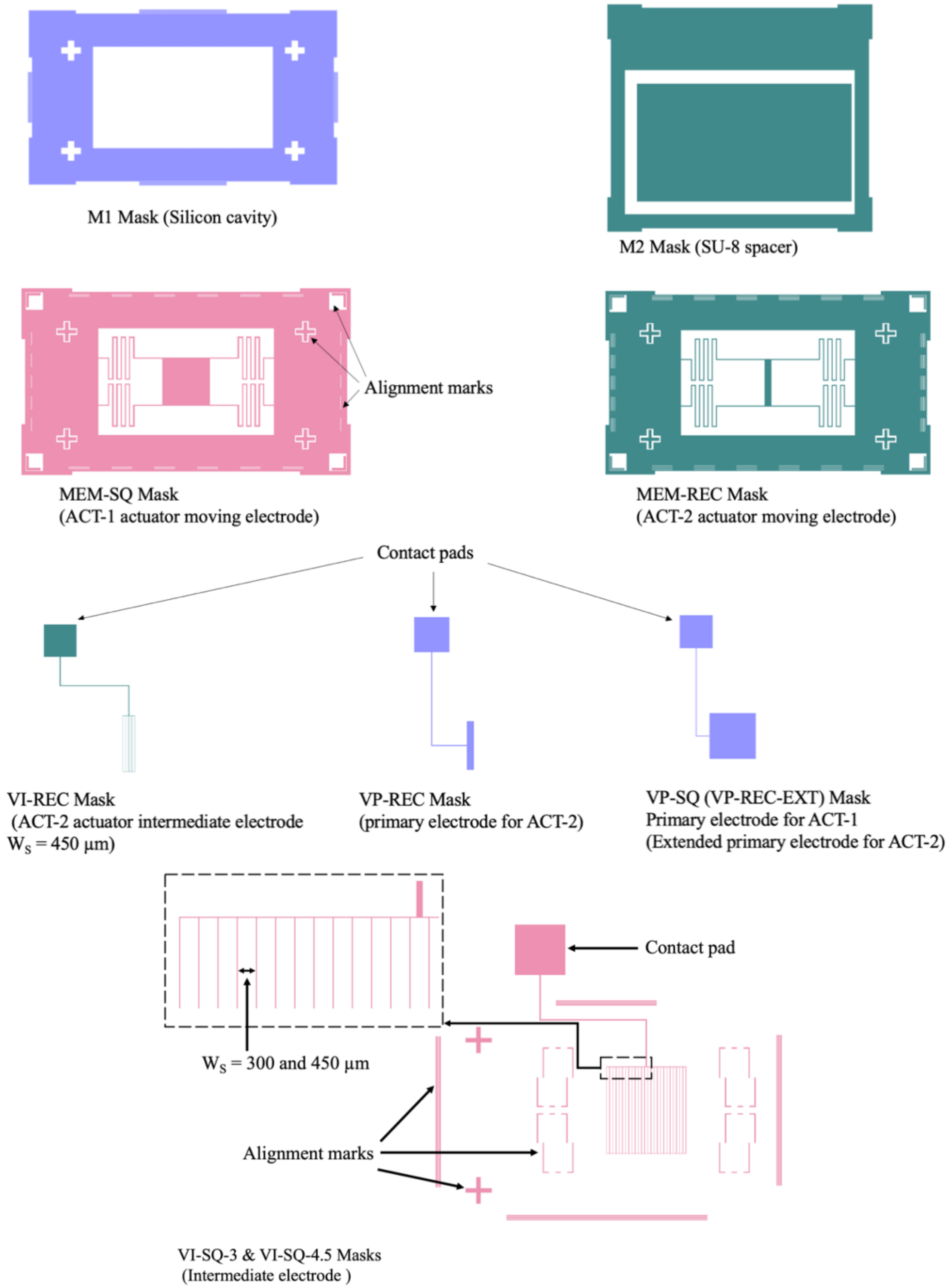

Figure 4.9. Photolithography masks for two ACT-1 and ACT-2 actuators.

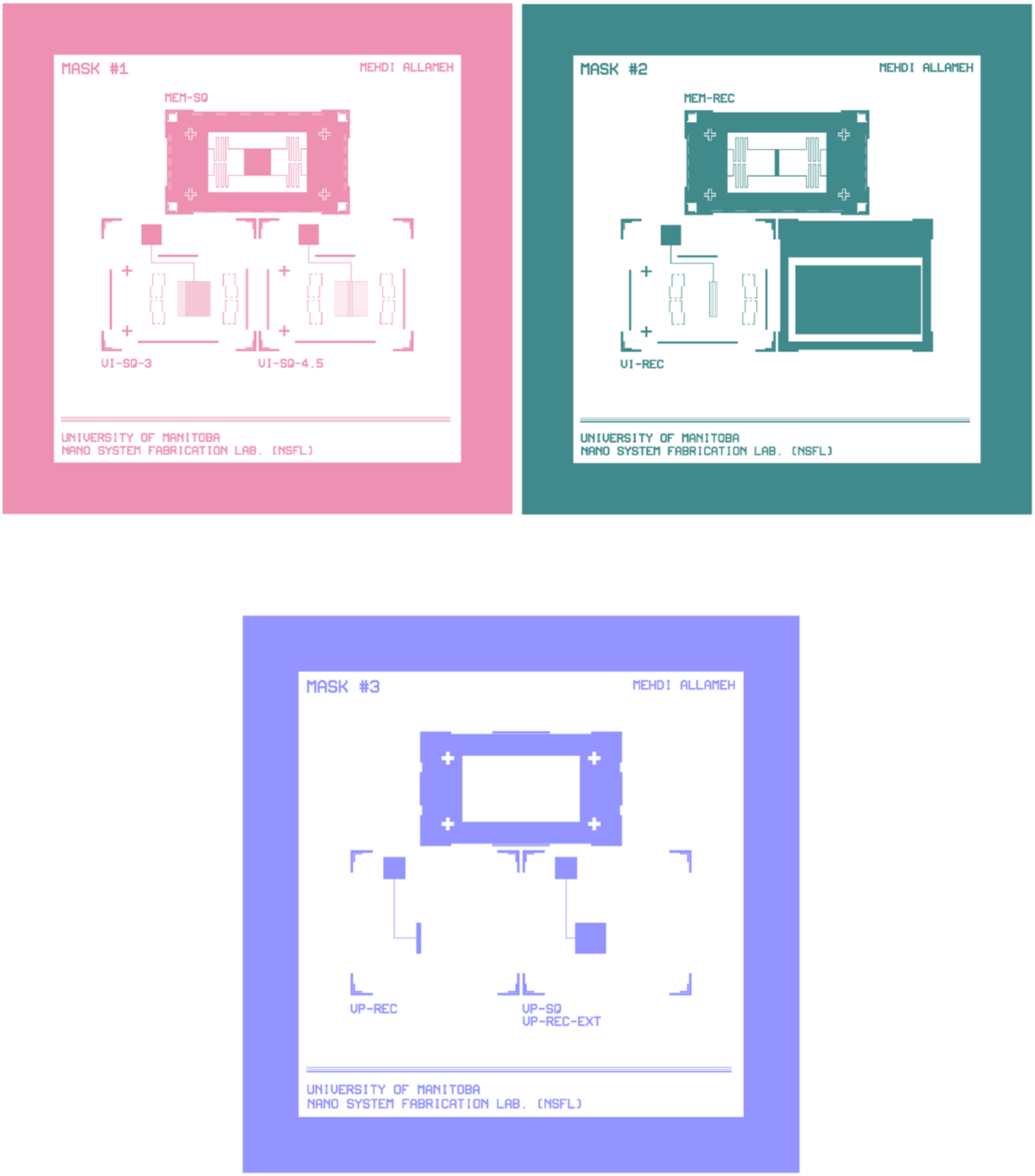

Figure 4.10. Photolithography masks for two ACT-1 and ACT-2 actuators fabrication based on three transparent masks ordered to nano fab (Masks # 1,2,3).

M_1, and M_2 are the common masks for both ACT-1,2. M_1 is used to form the thin silicon layer for both actuators in the KOH etch, and M_2 is to pattern the SU-8 thin spacer layer between two quartz and silicon to attach them and as an electrical isolation.

In ACT-1, MEM-SQ mask is for patterning the moving MEMS electrode on the front side of the sample. VI-SQ-3 and VI-SQ-4.5 are the masks for intermediate electrodes at the two different gap spacings. VP-SQ (VP-REC-EXT) is the primary electrode mask.

In ACT-2, MEM-REC is the mask for the very narrow moving electrode. VI-REC is the intermediate electrode mask. VP-REC is the primary electrode mask, and VP-SQ (VP-REC-EXT) is the narrow primary mask to test the narrow compact actuator.

4.4 Fabrication steps

Before fabrication starts, the wafers should be cleaned, removing any metal or organic residues from their substrates. First, the 4-inch silicon and 3-inch quartz wafers were washed with isopropanol alcohol (IPA), and following, washing with acetone to remove any remaining contamination from cleaning with IPA, then the wafers were dried using N_2. Following this, cleaning the wafers was continued using piranha solution to remove the organic residues. Therefore, the wafers were soaked in the piranha solution (4:1 mixture of sulfuric acid and hydrogen peroxide) for 5-10 minutes. Afterwards, the wafers were rinsed with deionized water (DI) and dried with N_2.

4.4.1 MEMS moving electrode – Silicon wafer

After cleaning, the wafers need to be cut into the designed pieces, but first, an oxide layer was grown since the wafer oxidation quality might not be adequately uniform after cut.

4.4.1.1 Oxidation

A thermal silicon dioxide (oxide) layer is required to be grown on the samples as a mask for the following silicon wet etch step. Since the silicon etchant also etches the oxide, the oxide should be thicker than a specific value. During the oxidation, the wafers were moved back to the front, rotated, and flipped across the wafer holder to have the uniform oxide layers. Thus, almost a 2.7 µm oxide was grown using an oxidation furnace heated up to 1100 ℃. The thickness of oxidized wafers is reported in Appendix C. After taking the wafers out of the furnace. They were cut into the designed pieces using a wafer saw. Since the wafer cutting also contaminates the samples, it was needed to repeat the cleaning steps.

4.4.1.2 Oxide patterning (photolithography 1)

This step is to pattern the square opening on the back side of the silicon sample to etch the oxide. The oxide was patterned using a positive photoresist (PR) HPR 504 after oxidation, using Solitech spin coater. A dehydration bake was carried out at 100 ℃ using a vacuumed hot plate to remove the humidity. Following, an HMDS (Hexamethyldisilane) curing was done at 150 ℃ for 5 min to increase the PR adhesion. However, the dehydration and HMDS curing steps were not improved the adhesivity of the surface sufficiently. Therefore, a very thin layer of chromium (Cr) was coated on the oxide on both sides, the results were very promising, and the PR coating adhered to the entire surface of the sample appropriately. This step was examined and approved during the flexible tri-layer fabrication described in chapter 6. After coating the PR on the front side, the sample was baked at 115 ℃ for 2 min using a hot plate as a soft bake, and then after rinsing with DI water again baked in the oven at 125 ℃ for 25 min as the hard bake step (HB). Following, the back side of the sample was coated with PR, but heating in an oven was used for both soft baking and HB, this time to avoid any damage to PR on the front side. After soft bake in the oven, the PR was exposed to UV light (30 mW/cm^2) under the coated glass mask. Then the sample was immersed in the HPR 504 developer to wash off the exposed PR. Then, the sample was baked again in the oven as its HB.

4.4.1.3 Etching Oxide

After patterning, the sample was immersed in buffered hydrofluoric (BHF) acid to etch the oxide on the back side. According to our measurements, the oxide etch rate was about 60 nm/min. Thus, the sample was kept in BHF for almost 50 min considering 10% more time, ensuring to etch the entire oxide on the patterned area. Since the etching area is very wide, under-etch does not damage the final structure and an extra etching time can be used to remove the undesired oxide entirely. Then, the PR was washed with acetone and IPA. Following the coated Cr was etched using Cr etchant. The Cr layer was coated to improve the PR adhesion to oxide. There were some issues removing the entire oxide from the patterned opening which is addressed in this chapter's trials section.

4.4.1.4 Etching Silicon

30% potassium hydroxide (KOH) concentration at 80 °C was utilized to etch the silicon isotropically. Due to the different silicon crystal orientations in different directions, the etch rate will be different. When the silicon substrate orientation is <100>, the silicon can be etched isotropically as this crystal orientation is more suitable for rectangular cavities [74], and this orientation has fewer surface atoms which result in less trapped surface charges and dangling bonds [75]. According to [76], the expected etch rate should be about 1.1-1.2 µm/min, but the rate was a little lower in cleanroom (1-0.9 µm/min) due to the temperature variations and the aged KOH solution. A stirrer was used in the solution to make the etch more uniform. The samples were also rotated in the etchant solution to etch all the surfaces more equally.

In this step, the silicon was etched to reach the designed D_1 gap size, since the cavity depth is considered the gap between moving and intermediate electrodes. Following, it was needed to continue etching the remaining silicon to the thickness required for the MEMS moving device. Thus, three etching procedures were tried, as it is explained in the trial section at the end of this chapter. The sample after etching is shown in figure 4.11. The sidewalls have slower etch rates (angled with 54.47°) that were considered in the mask design section to have the desired opening at the end of etching. The silicon membrane after etching has two different values because two ACT-1 and ACT-2 actuators have different thicknesses.

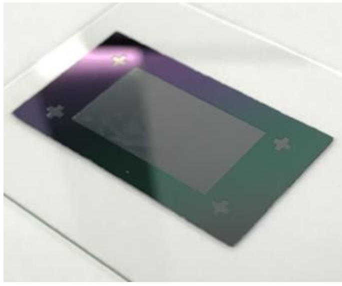

(a)

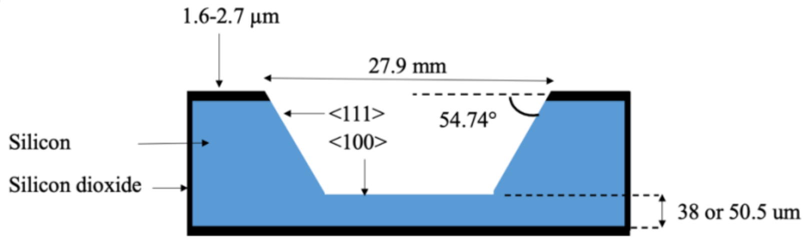

(b)

Figure 4.11. (a) The sample after KOH etch and (b) the schematic of the sample showing the angled sidewalls and the remaining silicon and silicon dioxide (oxide) after KOH.

In the KOH etch step, it was needed to etch the silicon for a thickness equal to D_1 to be able to use the edges of the cavity as the spacer material. However, the etch should continue to thin the silicon in the cavity area equal to the ultimate MEMS moving electrode thickness. First, the patterned silicon samples were etched for about 100 - 110 µm. The thinning step of the remaining silicon including the silicon in the cavity and the spacers were performed in three different trials as mentioned before.

4.4.1.5 Etching Oxide – remove oxide mask

After etching silicon to the desired thickness and having D_1 gap size, the remaining oxide was etched from both sides. Since the oxide also was etched during the silicon etch in KOH, the oxide was thinner and etched in a shorter time.

4.4.1.6 Aluminum deposition

A thin 300 nm of Al was deposited on the front side of the sample using sputtering. This Al was used as the conductive layer of the moving electrode and as a mask layer in the plasma etch step to release the structure. The recipe of the sputtering is also summarized in table 4.4. Due to the unavailability of the DC sputtering, RF sputtering was used for the deposition. In this case, the deposition rate is slower, and there is some change in the color of the Al at points where there are holes. This is because the higher electric field at the corners may damage the sputtered Al. In some cases, when the Al color turned in brown, another 100 nm layer of Al was deposited using thermal evaporation to keep the electrical conductivity continuous.

Table 4.4. Sputtering recipe for coating Al on the silicon samples.

Base Pressure	12 µ Torr
Work pressure	12 m Torr
Power	100 Watts
Argon Flow	100 SCCM
Time	90 min
Thickness	270 nm
Deposition Rate	3 nm/min

4.4.1.7 Al patterning (photolithography 2)

Lithography was repeated after sputtering Al, this time on the front side of the samples where the silicon was thin. MEM-SQ and MEM-REC masks were used for ACT-1 and ACT-2, respectively. Similar to lithography 1, a positive HPR 504 was spin-coated on the samples, and the lithography was done using the same recipe described before. The developed sample is shown in figure 4.12.

4.4.1.8 Al etch

The Al was etched by immersing the samples in the Al etchant at about 60-70 °C, stirring at about 300 rpm. After the etch, the samples were washed with DI and dried with N_2. Following, the PR was washed off using acetone and IPA. The sample ACT-1 after Al etch is shown in figure 4.12. The etch is a function of temperature. Therefore, the curve in [77] was used to choose the right temperature and the etching speed. On one hand a low temp. (slow) etch results in an under-etch around the narrow features such as springs, and on the other hand a very high temperature etch process can end up in a peeled-off and damaged PR. Thus, this issue is also discussed in the trial section.

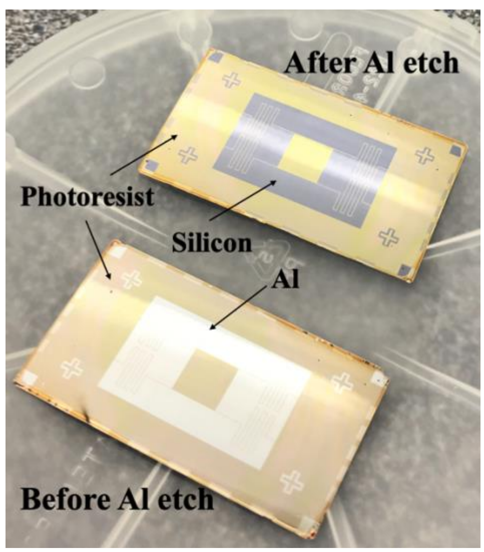

Figure 4.12. Samples (ACT-1) before and after Al etch.

4.4.1.9 Plasma etch – structure release

In order to release the moving MEMS electrode and etch the unwanted sections of the thin silicon membrane, the Trion Phantom II plasma etch was used. Due to the lack of deep reactive ion etching (DRIE) system at Nano System Fabrication Laboratory (NSFL), fluorine-based reactive ion etching (RIE) was used to have an isotropic etch for release. Releasing the structure with undercut might not be an issue in the surrounding area of the structure with relatively large feature sizes, but at parts with very small features, such as springs, it was needed to have a vertical trench around the elements. Therefore, having silicon fluorine based RIE helps us having a less under-cut in the final structure. Thus, the recipes were utilized from the previous plasma etches in NSFL logbooks and the studies from [78]. The ultimate attempted recipes and the one (Recipe 3) used in releasing the structure are summarized in table 4.5. The release attempts were also studied and reported in the trial section of this chapter. During the release, the other plasma etcher (PETS) was used and some useful etch recipes were extracted which are reported in Appendix D.

Table 4.5. The ultimate plasma etches recipes (1,2 and 3) for silicon etch and structure release (Trion plasma etcher).

	Recipe #1	Recipe #2	Recipe #3
Pressure (m Torr)	60	50	50
ICP power (W)	255	200	100
RIE power (W)	50	100	50
O_2 flow (SCCM)	5	15	15
CHF_3 flow (SCCM)	15	15	15
SF_6 flow (SCCM)	15	30	30
Etch rate (µm/min)	0.93	1.96	1.12

The structure (ACT-1) at different stages of the release is shown in figure 4.13a. The sample was monitored during the plasma etch, avoiding the over etch and having the structure fully released. Thus, the etched silicon was measured in various steps, in order to calculate the etch rate.

However, there have been some parameters that made the etching process complicated and not 100% under control. The most important parameters are reported in this chapter. The final structure is also shown in figure 4.13b.

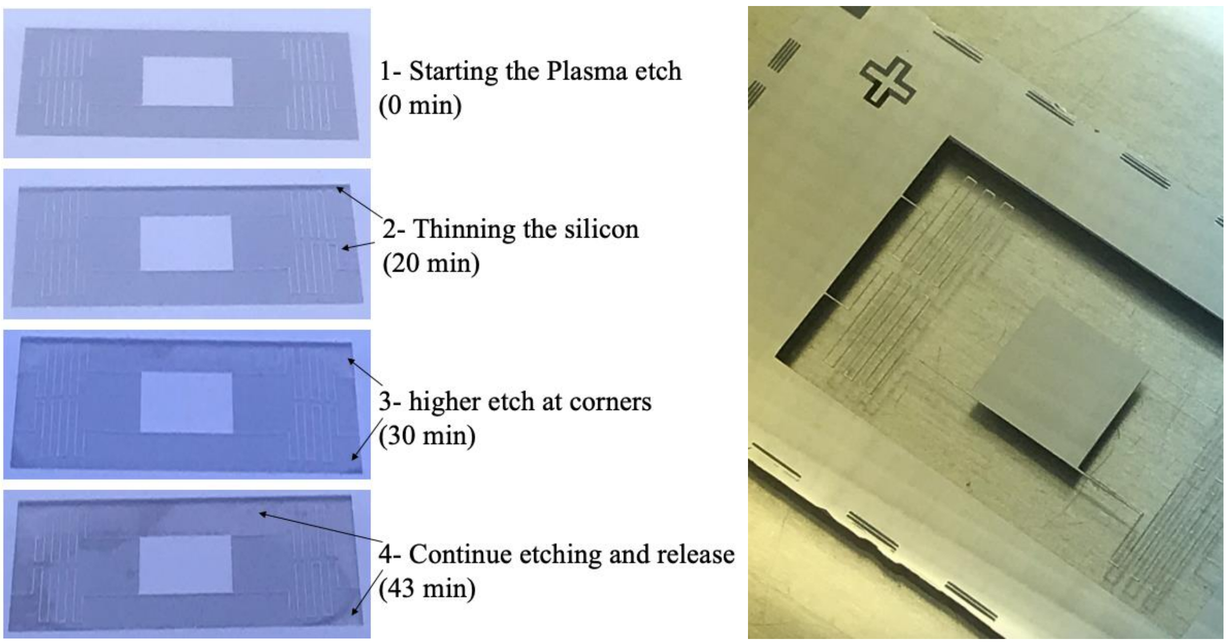

(a) (b)

Figure 4.13. Plasma etches of sample (ACT-1) with the final 30 µm membrane silicon using recipe #3 after four steps of etch (a) at the beginning and at 20, 30 and 43 min from beginning and (b) the released structure.

The ACT-2 released actuator is shown in figure 4.14.

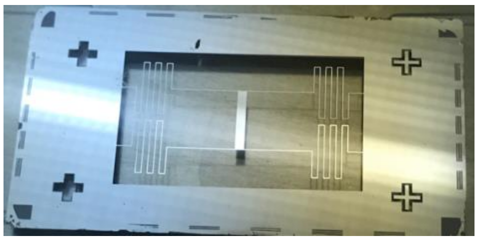

Figure 4.14. The ACT-2 actuator after plasma etches steps and release.

4.4.1.10 The MEMS fabrication steps

The entire fabrication steps of the silicon-based MEMS structure are shown in figure 4.15. The steps are as follows:

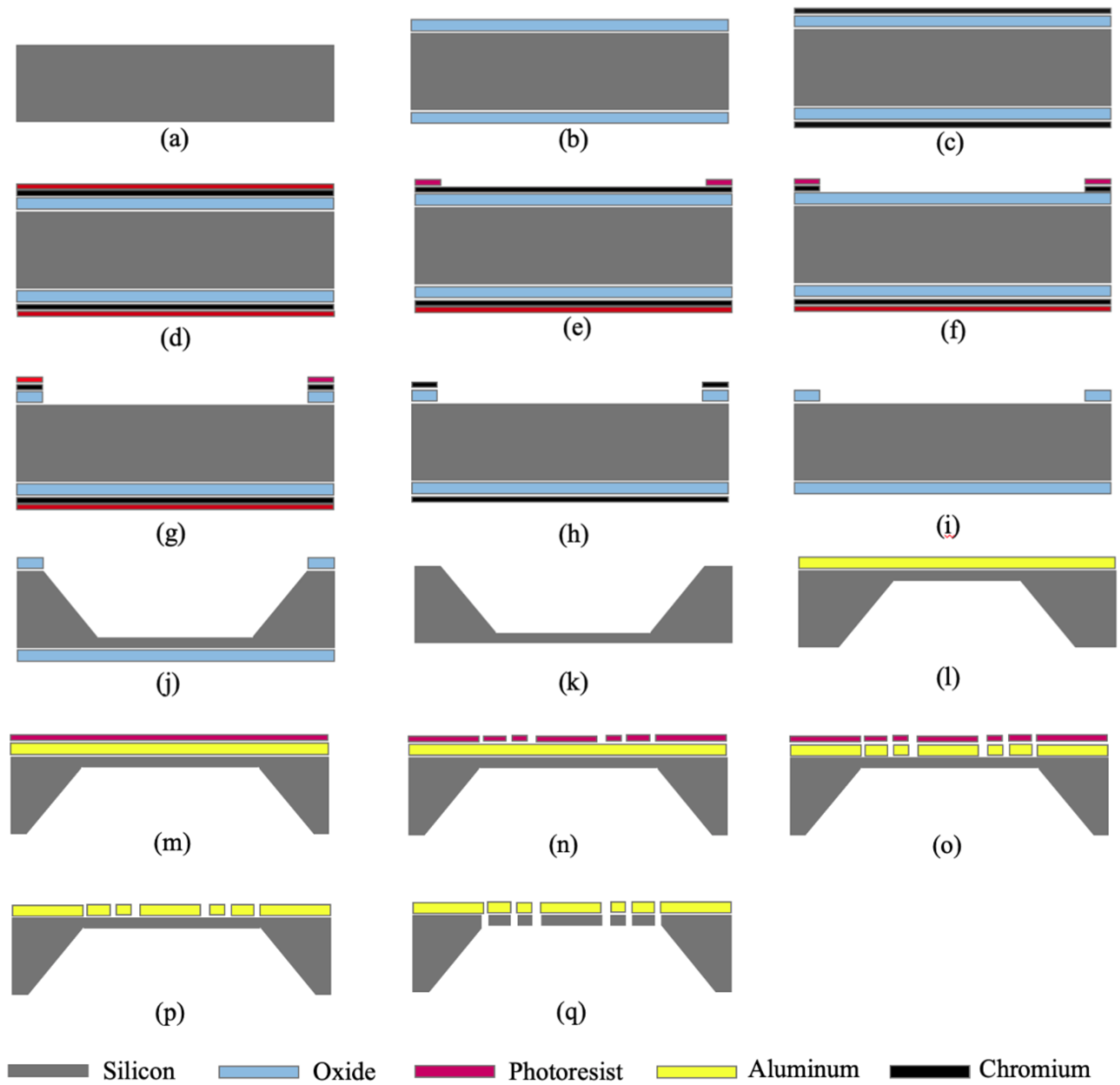

Figure 4.15. The MEMS fabrication performed at NSFL including the steps of (a) silicon wafer cleaning, (b) thermal oxidation, (c) sputtering Cr, (d) PR spin coating, (e) patterning and exposing PR, (f) etching Cr, (g) etching oxide using BHF, (h) washing PR with acetone, (i) etching Cr, (j) etching silicon isotopically using KOH, (k) etching oxide using BHF, (l) sputtering Al on the sample front side, (m) PR spin coating, (n) pattern and exposing PR, (o) etch Al, (p) washing PR with acetone and (q) releasing the structure using RIE plasma etch.

4.4.2 The fixed electrodes fabrication steps – Quartz wafer

In this section, the steps of fabricating the fixed electrodes of the tri-electrode topology using a quartz wafer are explained. After cleaning the wafer using IPA, acetone, and piranha, the quartz wafer was cut into pieces using the wafer saw. Since the cutting procedure contaminates the samples, the cleaning after the cutting was repeated.

4.4.2.1 Sputtering Aluminum

The quartz material is considered a spacer material in the tri-electrode topology; thus, its thickness (~ 490 µm) is the D_2 gap spacing between the intermediate and primary electrode. A thin layer of Al on both sides of the cut quartz sample was deposited, as the conductive layer of the electrodes. The RF sputtering system was utilized to deposit almost 290 nm of Al.

4.4.2.2 Aluminum patterning (photolithography 3)

Both sides of the quartz were spin-coated with HPR 504 photoresist. After soft bake, VI-SQ-3 and VI-SQ-4.5 masks were utilized to pattern the intermediate electrodes with different gap spacings for ACT-1. For the same sample, VP-SQ was used to pattern the PR on the other side to form the primary electrode.

VI-REC mask was used on one side of the two other samples to pattern the PR as the intermediate electrode for ACT-2 actuator. On the other side, one VP-REC was used to pattern the primary electrodes.

After exposing and developing the PR, all the samples were hard baked in the oven for 30 minutes. The samples are shown before HB in the oven in figure 4.16.

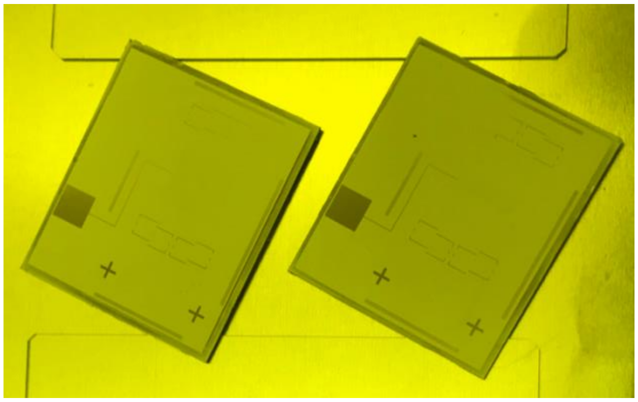

Figure 4.16. Two quartz samples after patterning the sputtered Al ready to be annealed in oven for HB step. The edge beads are seen as a rectangular ring at the edges of the samples.

4.4.2.3 Aluminum etch

After patterning the PR on both sides, samples were immersed in the solution of Al etchant for 30 sec at 60 °C. The stirrer was also used to make the Al etch uniform. In this case, the samples were put in the solution such that the etch is very uniform on both sides. The quartz sample for the ACT-1 actuator with two different intermediate electrode gap-spacings (W_S = 300, 450 μm) is shown in figure 4.17. The quartz sample for ACT-2 is also shown in figure 4.18.

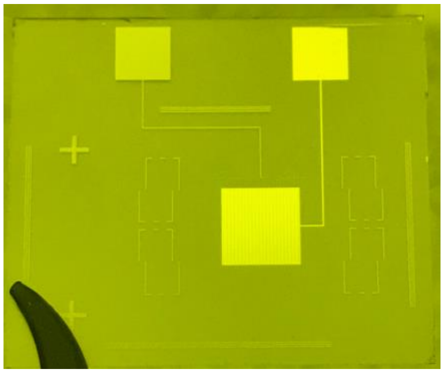

(a)

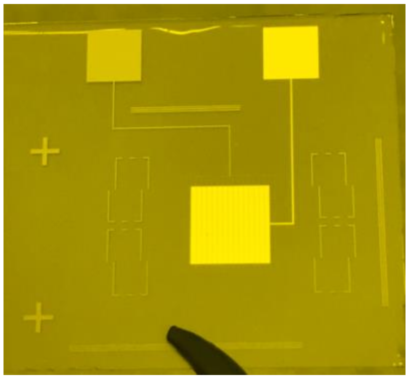

(b)

Figure 4.17. The quartz samples with two intermediate electrode gap-spacings of (a) W_S = 300 μm and (b) W_S = 450 μm for ACT-1 actuators.

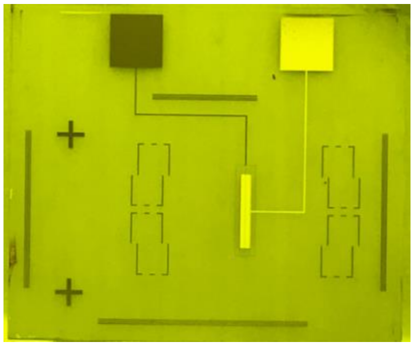

Figure 4.18. The quartz samples of the narrow rectangular actuator ACT-2.

4.4.2.4 Edge bead removal

One problem after pattering the Al is the higher thickness of the PR at the edges of the samples. After exposing the PR, the edges will remain, and after the Al etch step, we see an undesired Al ring of Al around the rectangular quartz sample. Therefore, a simple rectangular shape mask was used to expose the sample after spin coting for a very longer time (2-4 min) than the regular exposure. This time is needed to ensure that the PR at the edge was exposed deeply. The edge beads are shown in figure 4.16. The different trials to remove the edge beads are described in the trial section of this chapter.

4.4.2.5 SU-8 spacer

In order to have a dielectric spacer between the quartz and the silicon-based MEMS electrode, a thin layer of SU-8 2025 negative PR was spin-coated on the quartz samples. Even though the SU-8 is a PR (basically using for patterning), it also can be used as a structural layer if it is baked sufficiently in HB step. The thin SU-8 also can be used as an adhesive layer to attach the two parts of the tri-electrode actuator. The M2 mask was used to pattern the SU-8 forming the attaching layer. The same procedure of edge bead removal was also performed to remove the unwanted SU-8 rings at the edges of the samples.

4.4.2.6 The quartz samples fabrication steps

The complete fabrication steps of the quartz samples are illustrated in figure 4.19. The edge bead removal steps are not included in the figure. In the next step quartz and silicon samples were attached together as shown in figure 4.20.

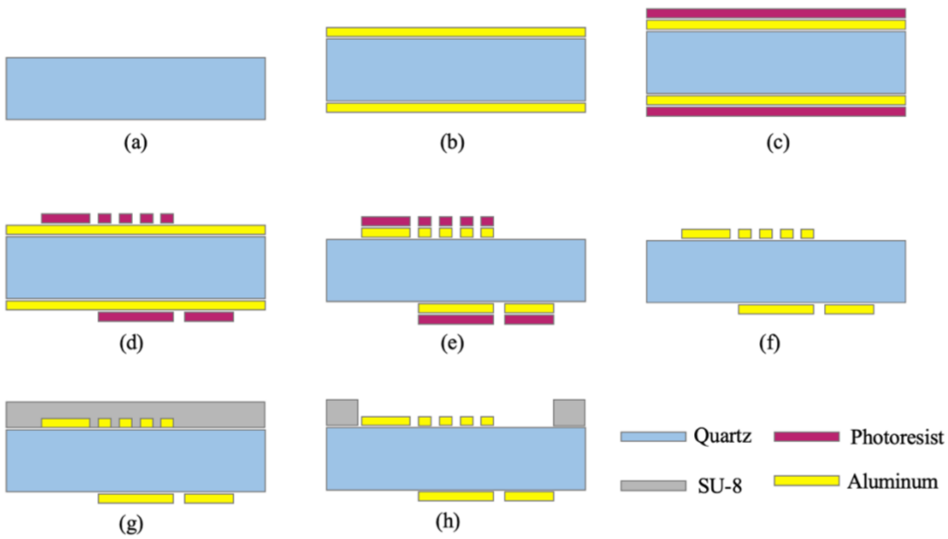

Figure 4.19. The complete fabrication steps of the quartz sample including (a) cleaning the quartz samples, (b) sputtering Al on both sides of the samples, (c) spin coating the samples with HPR 504 PR, (d) patterning the PR, (e) etching the Al in Al etchant, (f) washing off the PR using acetone, (g) spin coating the SU-8 and (h) patterning the SU-8.

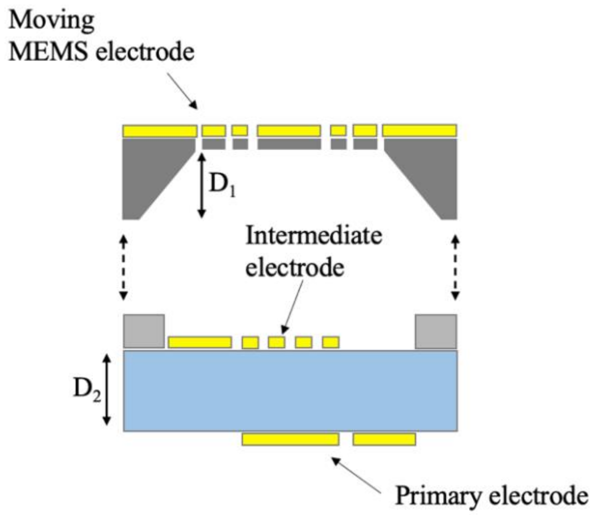

Figure 4.20. Attaching silicon and quartz samples to form the tri-electrode actuator.

4.4.3 ACT-1 and ACT-2

The square ACT-1 actuator and rectangular narrow ACT-2 are shown in figure 4.21 after attaching the silicon and quartz samples. The pictures are taken by Keyence VHX-7100 microscopes using 200x magnification.

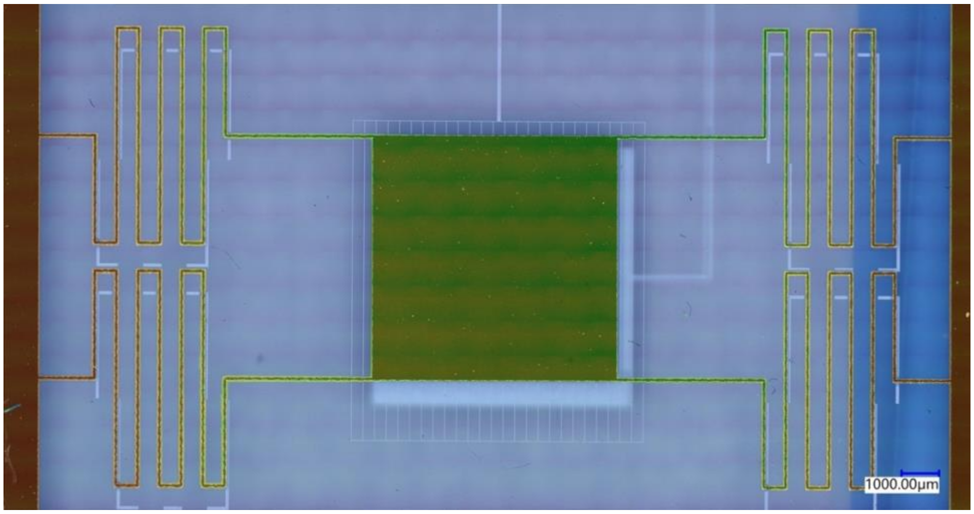

(a)

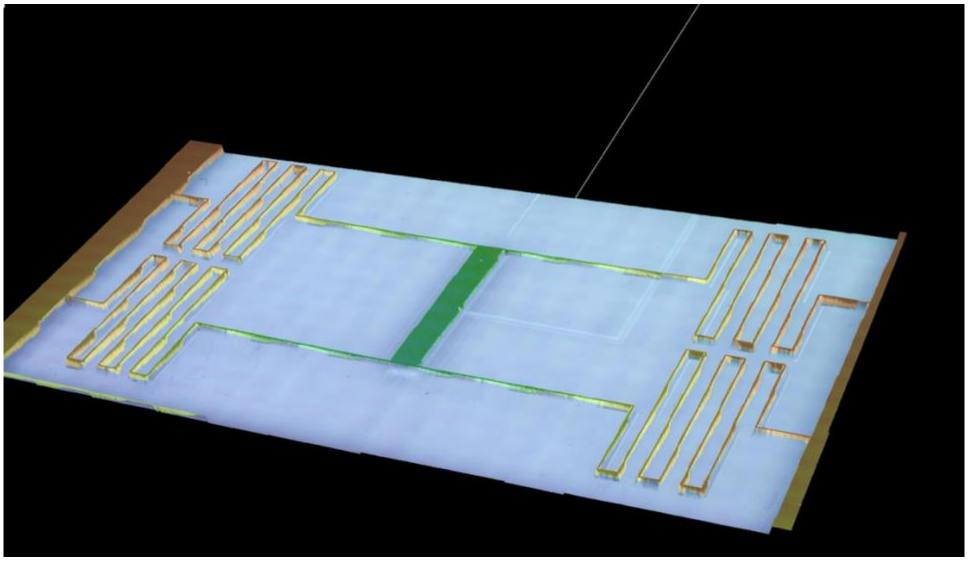

(b)

Figure 4.21. The picture taken from the square and narrow rectangular actuators after attaching silicon and quartz parts using Keyence VHX-7100 microscopes. (a) ACT-1 and (b) ACT-2.

4.5 Fabrication Trials

There were several trials in the fabrication of ACT-1 and ACT-2 actuators.

4.5.1 Trial #1: Multi-step KOH etch shown in figure 4.15(j).

- Problem:

  The second KOH etch was not successful in methods 1&2. The causes of not having an acceptable final product are indicated in the description of each method if this was unsuccessful.

- Solution 1 (unsuccessful):

  In this method, the oxide of both sides was etched using BHF etchant. Then the sample was immersed in KOH etchant to reach the desired thickness in the cavity area. The point of using this method is that the front and back of the silicon sample were etched at the same time, and the etching time is almost half of that when we only etch the back side. This method is not a 100% successful process since the surface quality of the front side (also the outer edge of the back side) is very rough, as shown in figure 4.22.

  Cause:

  The measurements showed roughness around 200-300 nm on the front side. This roughness is relatively high if we want to use the actuator surface as a mirror. Even though the KOH etch was performed under perfect conditions by rotating the samples periodically, the roughness was significantly larger than the original silicon roughness.

- Solution 2 (unsuccessful):

In method 2, after ending the first etch. The oxide was removed, similar to method 1. As etching both sides at the same time did not work in method 1. It was decided to cover the front side and etch the back side oxide with BHF. Cr is an available material we can use as a protective material. It also was used as an adhesion layer in the microfabrication of our actuators. Thus, it was unknown whether Cr could be an appropriate layer to protect the front side oxide. Thus, it was covered with another layer of copper (Cu). In order to find the appropriate recipe, another experiment was defined to evaluate the impact of BHF etchant on chrome and copper layers. An oxidized 3-inch silicon wafer was coated first with a very thin layer of Cr, then with Cu. Afterward, the wafer was cut into two pieces. One piece was covered with blue tape, and then both samples were immersed in BHF etchant for 60 min. The samples' images are shown in figure 4.23.

Cause:

The sample without blue tape was damaged during the etch. The Cr/Cu layer was damaged with KOH even though the experiment was repeated several times with different thicknesses of Cu. Therefore, it may be concluded that the Cr/Cu layer is not an appropriate layer protecting oxide during BHF etch for this experiment.

- Solution 3 (successful):

Using a thick layer of HPR 504 positive PR as the protective layer was a successful method to protect the oxide. Spin coating the front side of the sample was very challenging and broke the sample several times since the back side is etched and has a cavity. To resolve the issue, a small glass-made holder was designed to be able to spin coat the PR on the sample front side without any damage. Then the samples were immersed in BHF. The results were promising, and the front side oxide was intact while the back side oxide etched completely.

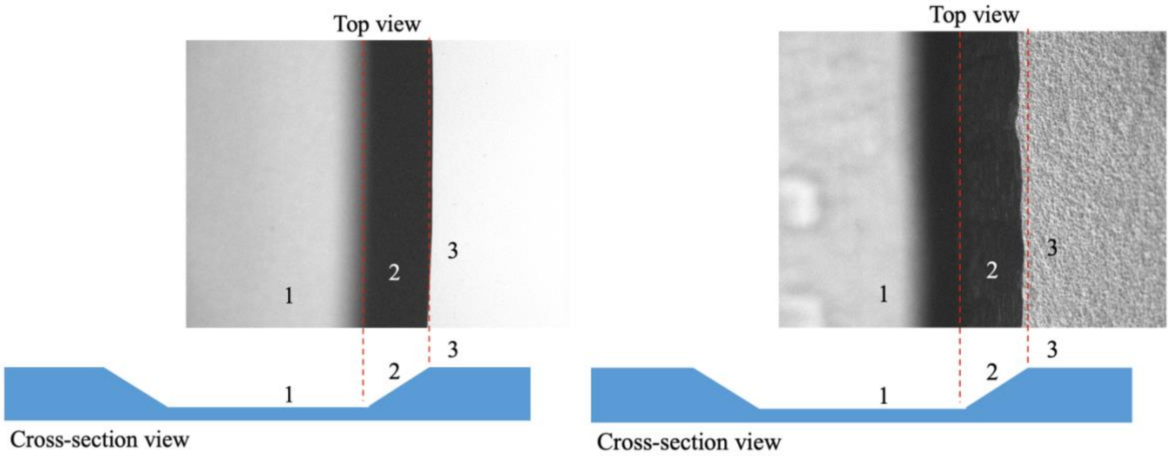

(a) (b)

Figure 4.22. The images of the silicon surface front side (a) before 2nd KOH and (b) after 2nd KOH etch step, showing the differences in roughness on areas #3 caused by the KOH etchant.

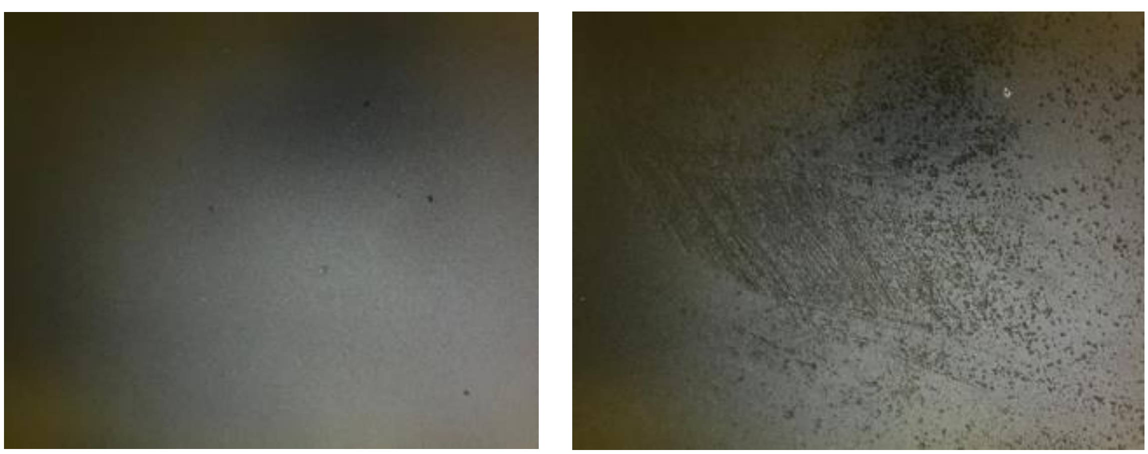

(a) (b)

Figure 4.23. The images of the oxidized silicon coated with Cr/Cu protecting layers after BHF etch under Olympus microscope with 20x magnification (a) covered with the blue tape and (b) not covered with the blue tape.

4.5.2 Trial #2: Etching oxide shown in figure 4.15(f).

- Problem:

  After finishing the BHF etch to form the oxide opening as the mask layer for etching silicon in the following steps. The oxide was not etched completely and some unetched islands were observed at the center of the opening as shown in figure 4.24. The main cause is that the PR was not removed during the developer process.

- Solution:

  The aged developer solution can cause the problem. Thus, a new developer was used besides cleaning the mask from any probable dust using a Nitrogen gun for the following etching steps. For the samples with unetched oxide spots, the samples were immersed again into the BHF for 10% more etch. The over etch process will not damage the entire structure since there is not very narrow and small features in the etch. The solutions were successful for both new and already etched samples.

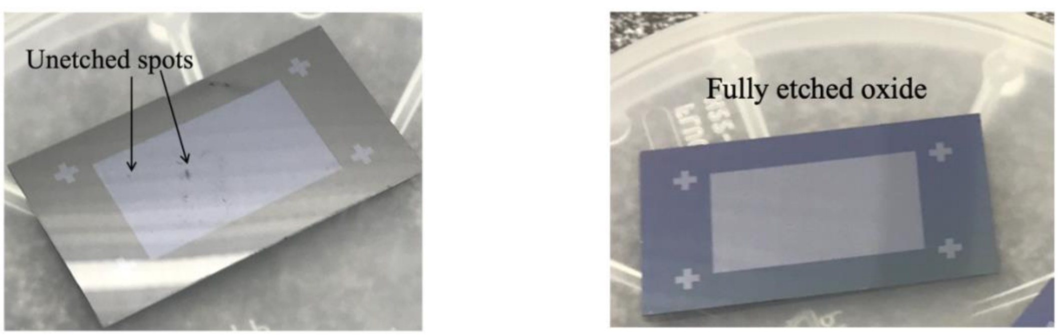

(a) (b)

Figure 4.24. The silicon samples after oxide etch when (a) there is unetched oxide spots in the opening and (b) a fully etched oxide without any unetched islands.

4.5.3 Trial #3: Etching Al shown in figure 4.15(o)

- Problem:

  The etched Al wires were narrower (80 µm) than the width of the designed mask (90 µm). The narrower etched Al will reduce the designed spring constant since the Al layer also used as the mask layer for the RIE plasma etch to release the structure.

- Solution:

  The etching time and the Al etch temperature are critical parameters. The higher the temperature, the higher the risk of peeling off the PR. In a relatively low-temperature etchant, the etching time is longer, and there is a higher risk of having a larger under etch. Thus, adequately short etching time and high enough temperature are the required parameters to etch the Al avoiding any under etch and narrow springs. Initially, a standard recipe recommended by the Al etchant manufacturer was used, involving heating the Al etchant up to 50 ℃. A magnet stirrer with a speed of 250 rpm was also used to have a uniform etch. The spring's width after etching was 80 µm. Besides the temperature, the higher stir speed can help have a more uniform etchant solution. Therefore, after several attempts, the Al etchant with 60 ℃ and a stirrer speed of 300 rpm was used. The measured springs after etching were about 88-94 µm, close to the designed value. The profile of the Al thickness for the first and second etch settings are shown in figure 4.25. The two scans are measured in two different vertical resolution. Therefore, this is the reason they look a little different at their levels.

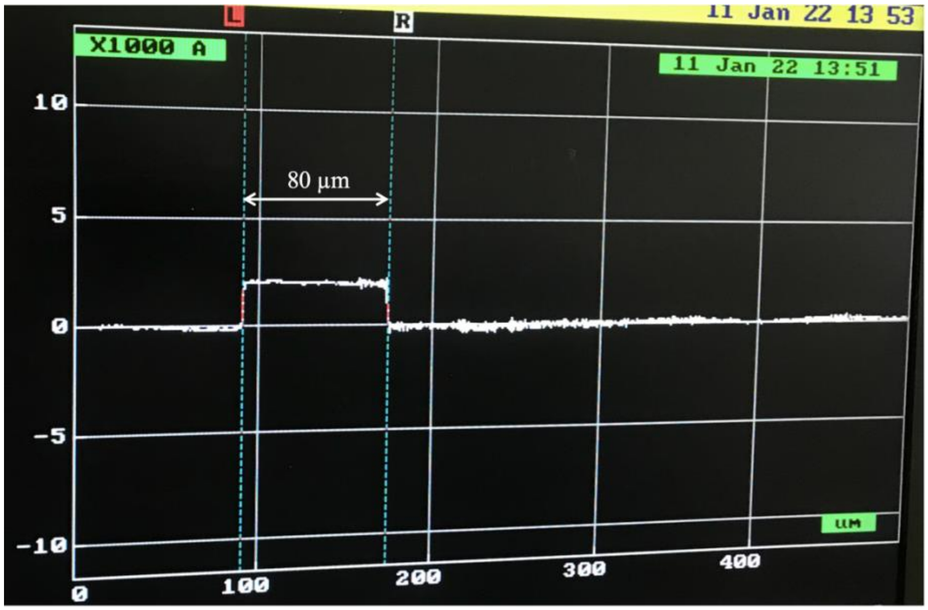

(a)

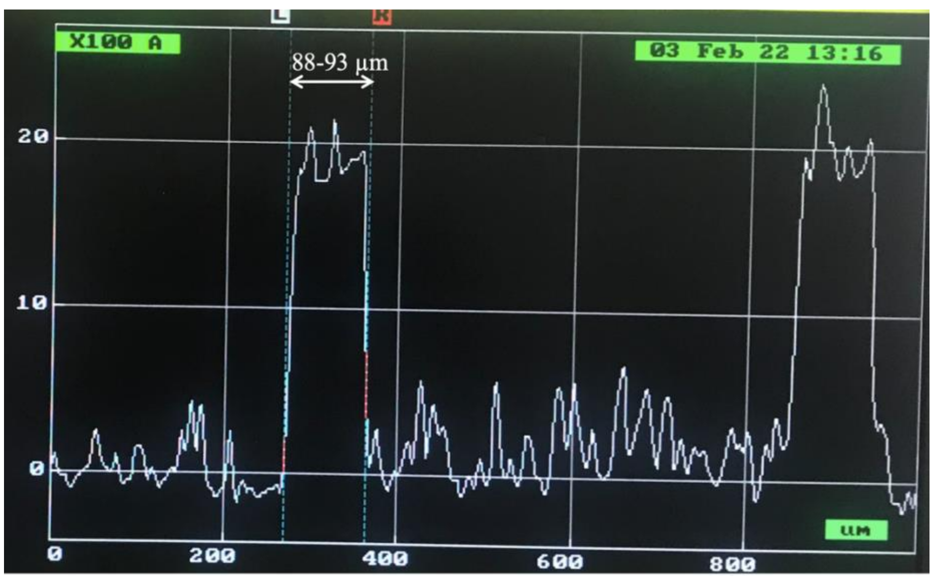

(b)

Figure 4.25. The spring profile scanned with Tencor Alphastep 500 profilometer after (a) first time Al etch and (b) the final Al. The scans were performed with different height resolutions.

4.5.4 Trial #4: RIE plasma etch shown in figure 4.15 (q)

- Problem:

The structure after release is narrow at springs using a plasma etch recipe #1 due to the high level of silicon under etch. Therefore, a well-developed recipe [78] were used with a different combination of O_2 and SF_6 flow rates and the ICP and RIE powers, recipe #2.

- Solution:

In the new plasma etch recipe, the entire spring has a less narrow width, but the top surface of the actuator toward the sources of ions is narrower. This is due to the under etch effect during the al etch, and also during the anisotropic plasma, RIE etch. Thus, having a recipe with half ICP and RIE power helps to have a less under etch, though the etch rate is slower. The released spring images using recipes #1-3 are shown in figure 4.26 and 4.27. It is apparent that using recipe #3 gives the springs very much closer to the designed thickness and width. The process of etching and releasing the springs, including etching silicon and under-etching the springs are illustrated in figure 4.28. Final measurements using recipe #3, showed that the released structure has a minimal under-etch.

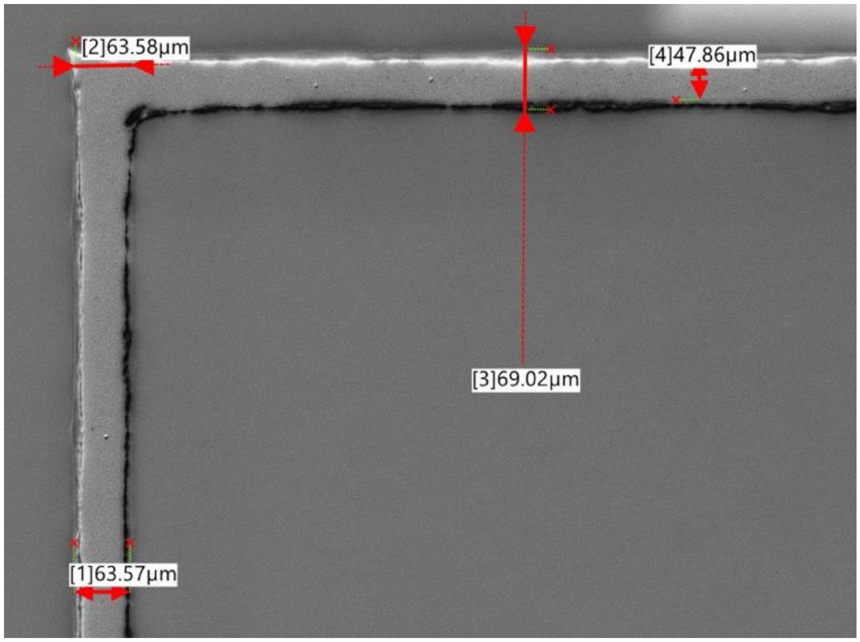

(a)

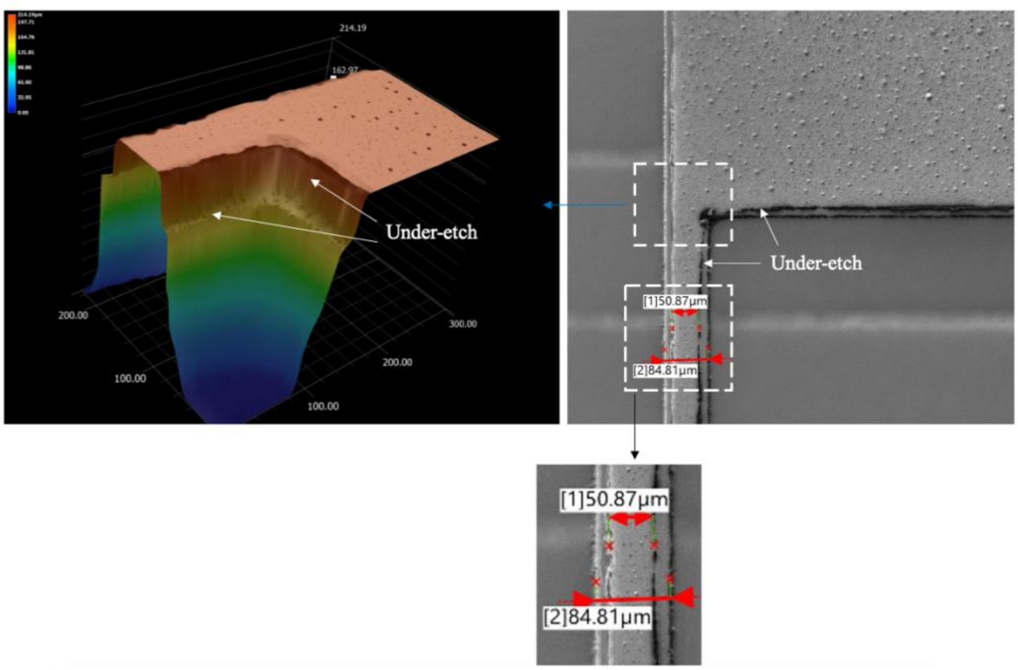

(b)

Figure 4.26. The image taken with a Keyence microscope from the released structure (spring) using (a) recipe #1 (spring width is ~48μm at top and 69μm at bottom), (b) recipe #2 (spring width is ~ 51 μm at top and ~85 μm at bottom).

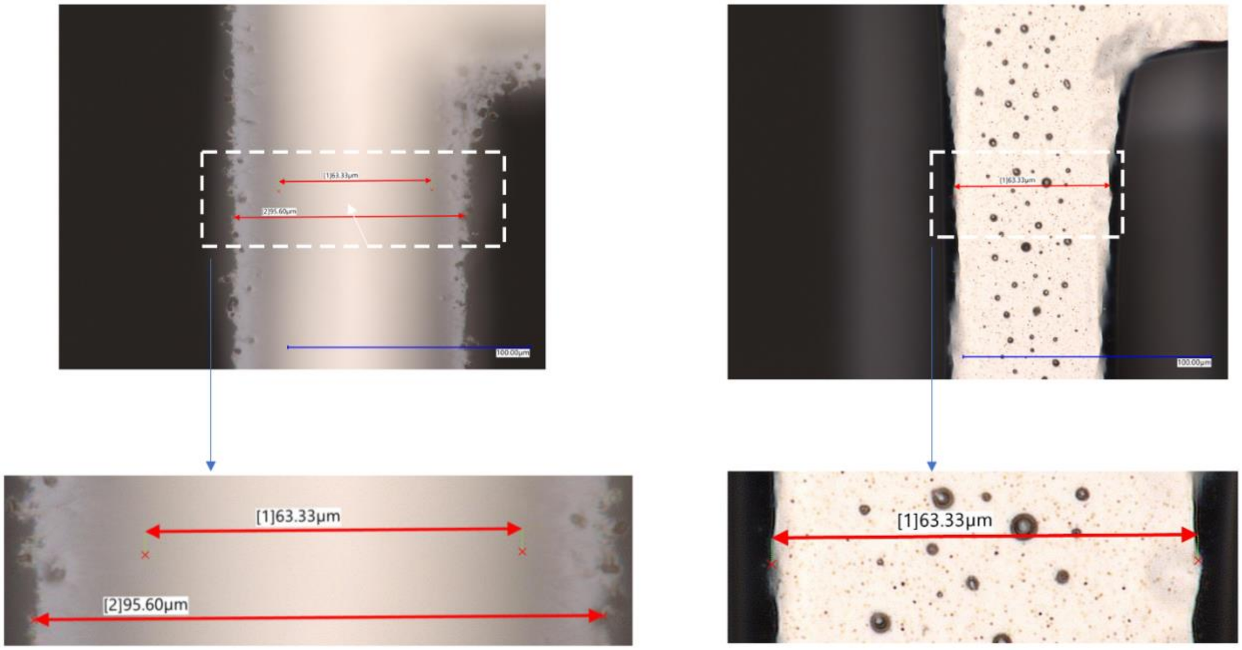

Figure 4.27. The image taken with a Keyence microscope from the released structure (spring) using recipe #3 (spring width is ~63 µm at top and 95µm at bottom).

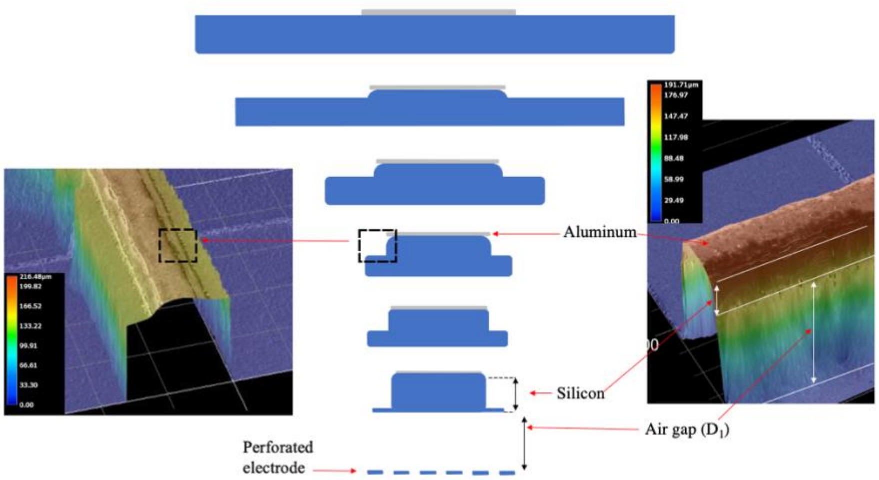

Figure 4.28. The schematic shows the steps of etching silicon using Al as the etch mask, also showing the Al under etch. (The color legends are not exactly representing the spring height and thickness, as the taken images are resized and the colors were altered, the images were taken at two different spots and are used only showing that how under-etch alters the spring shape).

4.5.5 Trial #5: Edge beads removal shown in figure 4.19 (e&h)

- Problem:

During patterning Al and SU-8, the PR coated at the edges of the samples has a higher thickness and forms the edge beads. Failing to remove the thicker PR can cause an electrical connectivity problem for intermediate electrode. It also causes an unwanted thick SU-8 at the edges. Since, the regular time and power of UV exposure might not be adequate to fully expose the edge beads. Thus, a separate exposure with a higher power is essential.

- Solution:

Due to the limited space on the designed masks (#1-3), there were no masks designed explicitly for edge bead removal. Thus, a hand-made mask using black tape and glass was designed to expose the edges of the samples. The exact required time to remove the edge beads also was not known. Thus, several exposures were carried out to explore the minimum time. The samples before and after edge bead removal are shown in figure 4.29.

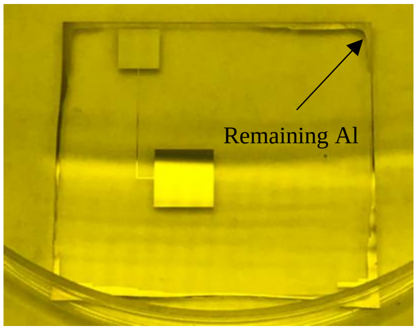

(a)

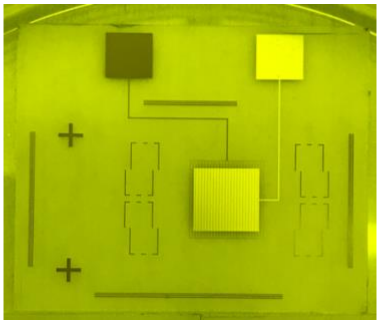

(b)

Figure 4.29. (a) Glass sample after Al etch without edge bead removal step and (b) the quartz sample after Al etch including the edge bead removal.

4.6 Final actuator dimensions

Considering the limitations of the fabrication and the errors in various steps such as etching and releasing, a few alterations were made in the built tri-electrode actuator dimensions. Some of the modifications (D_1 and D_2 spacings) were modified due to microfabrication issues and fabrication limitations, and some dimensions such as MEMS moving electrode thickness (t) were altered. The final actuators' dimensions, (design parameters) are summarized in table 4.6 and 4.7. Accordingly, the simulations studies of section 4.2 were repeated to extract the tri-electrode actuator performance and response curves according to these values. The new simulation results are discussed in Chapter 5, in conjunction with the device performance analysis.

Table 4.6. Tri-electrode topology parameters – square MEMS.

Parameters	**Designed Values**	**Built Values**
$D_{1,\ best\ FOM}$ (unipolar and bipolar modes)	100 µm	140 µm
$D_{1,\ best\ displacement}$ (maximum displacement mode)	100 µm	155 µm
D_2 (quartz)	500 µm	490 µm
W_E	16.7 µm	16.7 µm
$W_{S\ best\ FOM}$	300 µm	300 µm
$W_{S\ best\ displacement}$	450 µm	450 µm
MEMS thickness	40	30

Table 4.7. Tri-electrode topology parameters – rectangular MEMS.

Parameters	**Designed Values**	**Built Values**
$D_{1,\text{ best FOM}}$ (unipolar and bipolar modes)	100 µm	120 µm
D_2 (quartz)	500 µm	490 µm
W_E	16.7 µm	16.7 µm
$W_{S\text{ best displacement}}$	450 µm	450 µm
MEMS thickness	40	30

5

Test Experiments

Contents

5.1 Introduction

The MEMS electrodes were designed and built in Nano System Fabrication Laboratory cleanroom using the microfabrication procedures described in chapter four. In this chapter, the three tri-electrode designs were employed to do experiments and test the actuator's performance.

5.2 Tri-electrode configuration - Square MEMS Design

As discussed in section 4.6, the built actuator dimensions were different from the initial designs of section 4.2, due to fabrication issues. Tables 5.1a and 5.1b show the final fabricated device dimensions.

Table 5.1a. Tri-electrode topology parameters – unipolar, bipolar and maximum displacement modes.

Parameters	**Values**
$D_{1,1}$	140 µm
D_2 *(quartz)*	490 µm
W_S	300 µm
W_E	16.7 µm

Table 5.1b. Tri-electrode topology parameters – higher maximum displacement mode.

Parameters	**Values**
$D_{1,2}$	155 µm
D_2 *(quartz)*	490 µm
W_S	450 µm
W_E	16.7 µm

Analysis of device with dimensions shown in table 5.1a:

The numerical simulations for device performance discussed in section 4.2 were repeated, in order to determine the performance of the final built actuator dimensions. As we know for the case of unipolar and bipolar modes, the required V_P should be determined when the moving electrode travels the distance equal to D_S (conventional maximum displacement before snap down). For this purpose, the primary controlling voltage was swept in simulation from 0 to 140 V and the response curves at each V_P were calculated. Figure 5.1 (table 5.1a values) shows the maximum possible displacement (Δd) of each response curve before snap-down vs. V_P.

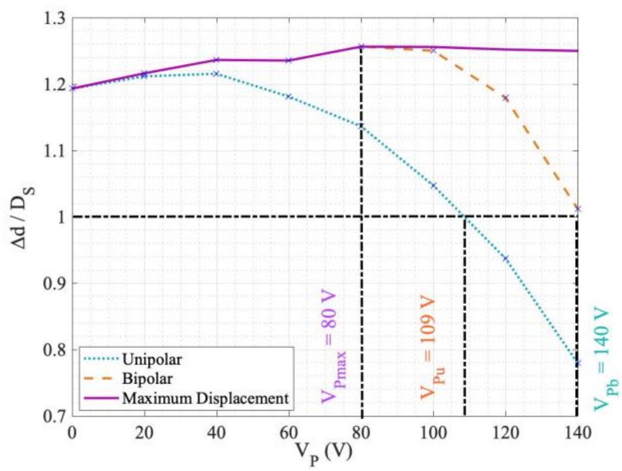

Figure 5.1. Simulations results of the maximum possible displacement (Δd) vs. V_P for unipolar, bipolar and maximum displacement.

We can see that the primary electrode voltage (V_P) for when the actuator travels the distance equal to D_S for unipolar and bipolar modes are V_{Pu} = 109 V and V_{Pb} = 140 V, respectively. The *FOMs* found in simulation are FOM_u = 1.4 *FOMs*, FOM_b = 2.6 *FOMs*. The maximum possible displacement (Δd_{max}) at this gap spacing (W_S = 300 µm) occurs at V_P = 80 V and is 28% larger than the conventional actuator (Δd_{max} = 1.28 D_S). Note, the conventional actuator in this case has a D_1 = 140 µm.

The response curves for all three cases are depicted in figure 5.2. The response curves were plotted for the controlling voltage (V_P = 80, 109, 140 V), and also in the unstable region, and the snap-down point is highlighted with red crosses.

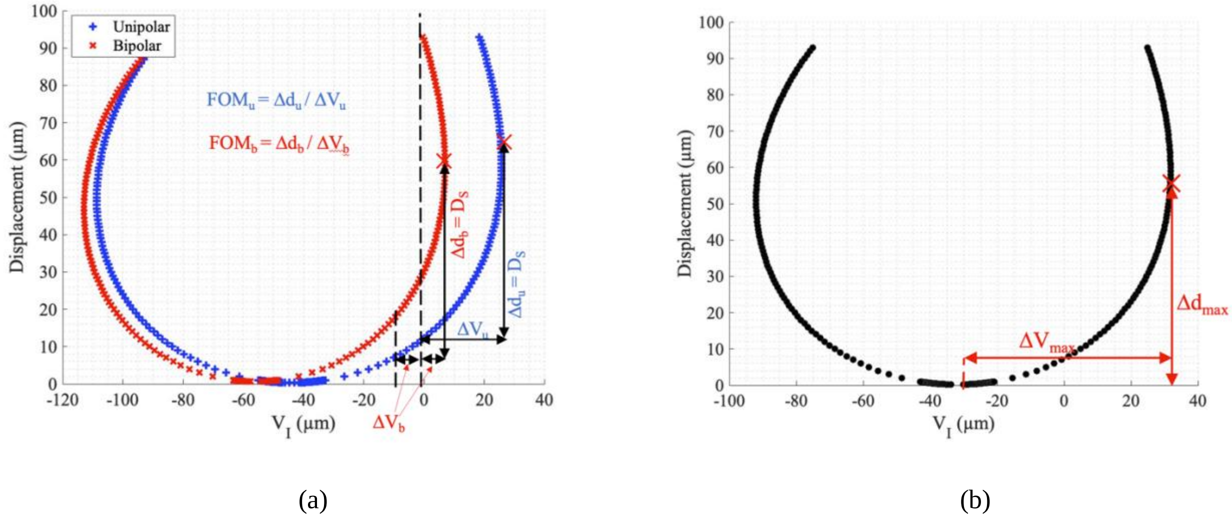

Figure 5.2. Simulations results of the displacement vs. V_I for (a) unipolar and bipolar modes (V_{Pu} = 109 V, V_{Pb} = 140 V), and (b) maximum displacement, for $D_{1,1}$ = 140 μm, D_2 = 490 μm, W_S = 300 μm, W_E = 16.7 μm. The snap-down point in the negative voltage range is not highlighted as the actuator performance is poor when V_I has a different voltage polarity than V_P.

Analysis of device with dimensions shown in table 5.1b:

Simulations were also done for W_S = 450 μm, which gives a higher maximum possible displacement (as discussed in section 4.2). Simulations were repeated for this spacing, to find the maximum displacement and its corresponding V_P. The studies showed that the maximum displacement occurs at V_P = 120 V and has a maximum possible displacement 33% larger than the conventional actuator (Δd_{max} = 1.33 D_S). Note, the conventional actuator in this case has a D_1 = 155 μm.

5.3 Tri-electrode configuration - Narrow Rectangular MEMS Design

Similar to the previous section, numerical simulations were performed for updating all three cases of the unipolar, bipolar and maximum displacement. The primary electrode voltage was swept from V_P = 0-120 V and in each case, the actuator response curve was plotted and the maximum displacement was determined. The results (displacement (Δd) vs. V_P) are plotted in figure 5.3. This figure was used to determine the required V_P for each of the cases. The parameters of the narrow rectangular tri-electrode topology are reported in table 5.2 (from section 4.6).

The primary electrode voltage for each of the three modes are V_{Pu} = 93 V (unipolar), V_{Pb} = 112 V (bipolar), and V_{max} = 70 V (maximum displacement). The response curves for all three cases are depicted in figure 5.4. The response curves for the controlling voltage are plotted only in the stable region here, so the maximum value of displacement is the snap-down point. The reduction in controlling voltage in the cases of unipolar and bipolar can be recognized by looking at figures 5.4 a,b. The *FOM* for unipolar and bipolar are FOM_a = 1.23 *FOMs*, FOM_b = 2.5 *FOMs*, respectively. The maximum displacement is 40% larger than the conventional actuator.

Table 5.2. Very narrow tri-electrode topology parameters

Parameters	**Values (µm)**
D_1	120 µm
D_2 *(quartz)*	490 µm
W_S	450 µm
W_E	16.7 µm

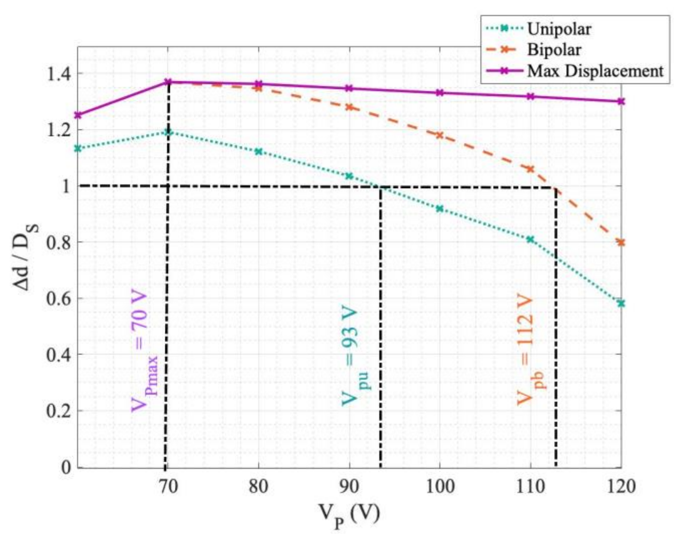

Figure 5.3. Maximum possible displacement (Δd) vs. V_P for unipolar, bipolar and maximum displacement.

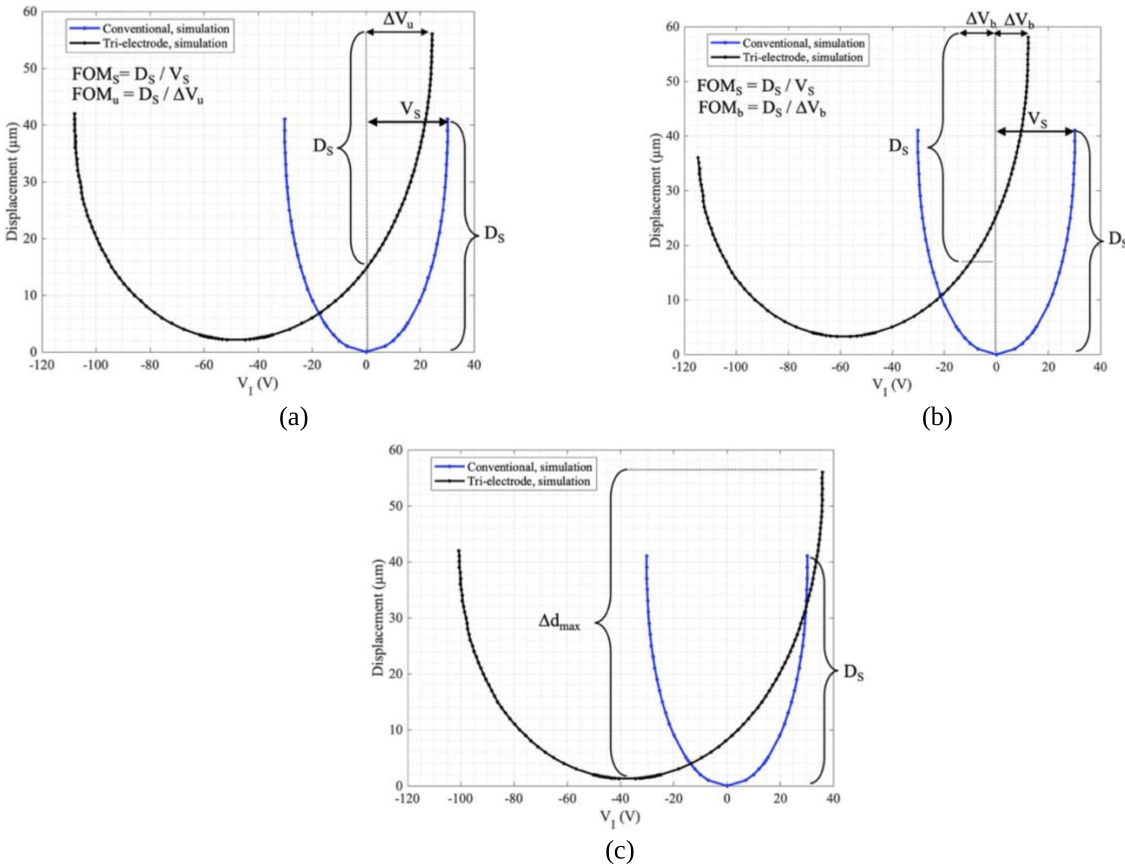

Figure 5.4. Displacement vs. controlling voltage for (a) unipolar at V_{Pu} = 93 V, (b) bipolar at V_{Pb}= 112 V and (c) maximum displacement at V_{max} = 70 V.

5.4 Experimental measurements

5.4.1 Square MEMS electrode

The set-up shown in figure 5.5 was used to do the experiment. The tested tri-electrode actuator was fixed on an aluminum plate, in order to avoid any unwanted charges interrupting the measurements. Three Agilent power supplies (E3620A, E3647A and E3646A) were utilized to supply the electrode voltages. Since the intermediate electrode is required to be supplied from a positive to negative voltage range in the two modes of bipolar and maximum displacement, two power supplies were used to bias the intermediate electrode and the third was used to bias the primary electrode. A fixed voltage was applied to the primary electrode, and at each V_P the intermediate electrode voltage was swept with the lowest possible resolution of 0.1 V.

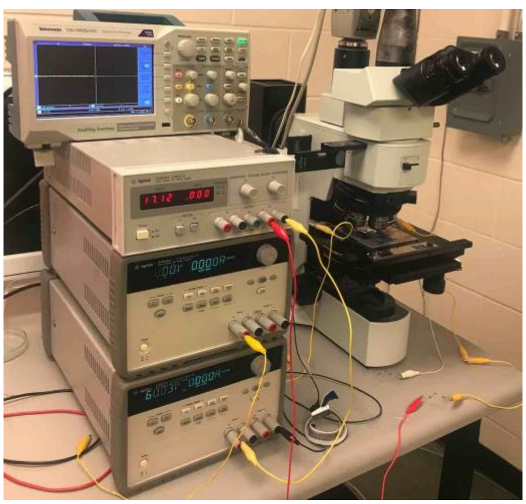

(a)

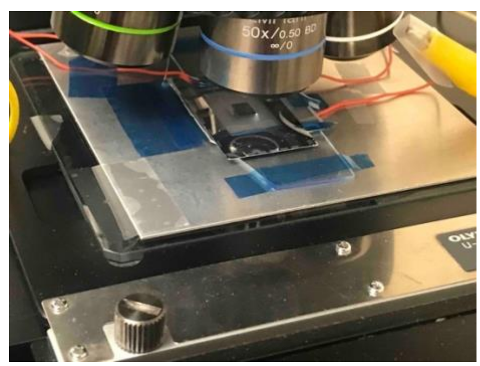

(b)

Figure 5.5. Measurement set-up using Agilent power supplies and Olympus (BX51) microscope. (a) Microscope and power supplies. (b) Tri-electrode actuator under the microscope with 50x magnification.

Two microscopes were utilized to measure the displacement of the moving electrode. An Olympus (BX51) was employed to measure the actuator displacement in the first measurements (seen in figure 5.5). However, measurements were later repeated using a Keyence (VHX-7100) microscope, since its software can easily determine displacement values using the method called depth from defocus (DFD). Measurements were made with 2500x magnification to have the higher accuracy.

Perforated conventional actuator measurement:

In the first step of the measurements, no voltage was applied to the primary electrode and only the intermediate voltage was supplied. This configuration is quite similar to the conventional topology. However, as the effective area is smaller (perforated conventional) we expect to need a larger voltage compared to the conventional topology. The conventional and the perforated conventional schematic are shown in figure 5.6.

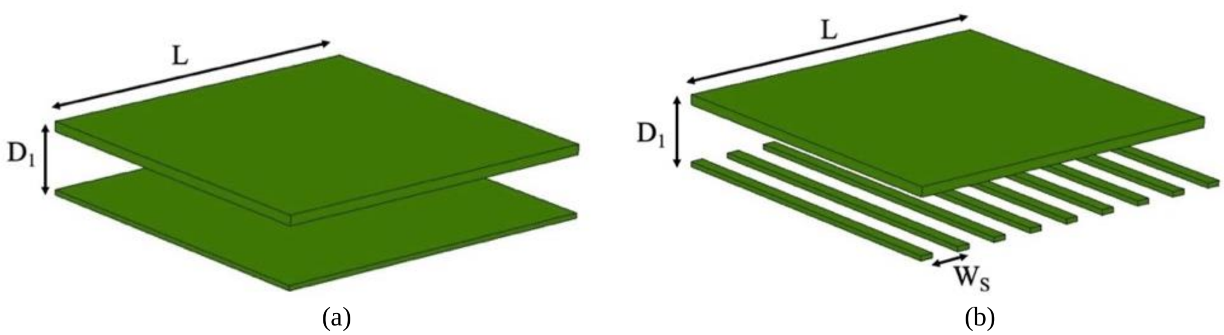

Figure 5.6. The schematic of the conventional topology and the perforated conventional topology (a) Conventional topology with D_1 gap spacing between the electrodes (b) perforated conventional topology with D_1 gap spacing between intermediate and MEMS electrode.

The results of the measurements of the perforated conventional topology (high impedance primary electrode) are shown in table 5.3 and plotted in figure 5.7. As expected, we see that the snap-down voltage is larger compared to the conventional as the effective area of the bottom electrode is decreased compared to the solid electrode. Note, the measurements with the Keyence microscope have ±4 µm error, due to the accuracy of detecting device motion with the microscope.

Table 5.3. The measured displacement with no voltage applied to the primary electrode when D_I = 140 µm, W_S = 300 µm and W_E = 16.7 µm

V_I (V)	Displacement (µm)	V_P
30	6	High Impedance (H.I.)
40	13	H.I.
45	21	H.I.
48	27	H.I.
49	32	H.I.
50.4	37	H.I.
51	41	H.I.
51.3	46	H.I.

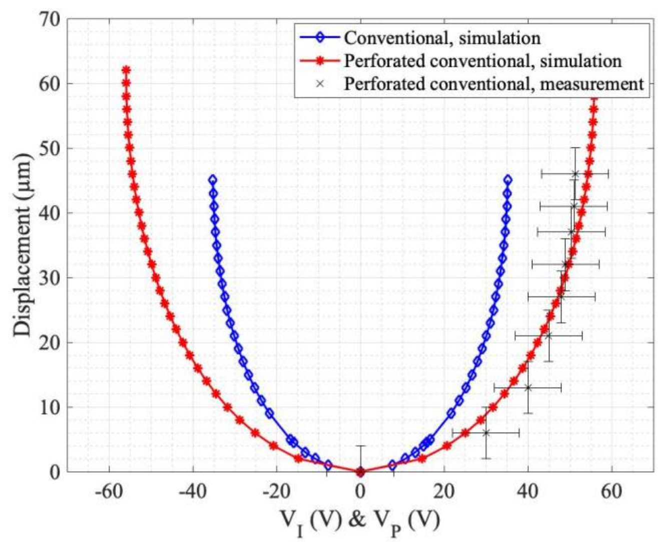

Figure 5.7. Displacement vs. controlling voltage (V_I or V_P) for perforated conventional topology (tri-electrode topology with H.I. primary electrode). As mentioned before, the measurement error is ±4 µm.

Tri-electrode operation measurement (table 5.1a configuration):

The primary voltage was extracted in the simulations to have the displacement equal to D_S for both unipolar and bipolar, as shown in figure 5.1. For unipolar mode, the V_P = 107 V was applied to the primary electrode and the intermediate electrode voltage was swept from zero to 26.6 V. The measured displacements are reported in table 5.4 and plotted in figure 5.8.

Table 5.4. The measured displacement for unipolar mode, when V_P = 107 V, D_1 = 140 µm, D_2 = 490 µm, W_S = 300 µm and W_E = 16.7 µm

V_I (V)	Displacement (µm)
0	10
5	13
10	15
13	18
16	22
20	27
22	30
24	34
25	38
25.5	40
26	43
26.4	46
26.6	50

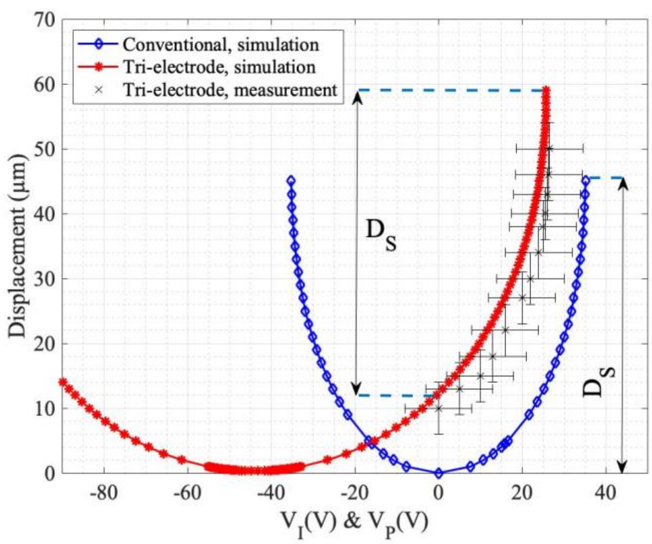

Figure 5.8. Displacement vs. controlling voltage (V_I or V_P) for unipolar mode when V_P = 107 V, D_1 = 140 µm, D_2 = 490 µm, W_S = 300 µm and W_E = 16.7 µm. As mentioned before, the measurement error is ±4 µm.

The depicted red curve shows the simulation results only in the stable region. The blue curve is the simulation results for the conventional topology and the black cross dots are the measurements. As can be seen, the measurements are in a close agreement with the simulation results. The results show that the controlling voltage range (snap-down voltage) of the unipolar mode (ΔV_u = 26 V) is smaller than the conventional one (V_S = 35.2 V) by almost 40% for the same displacement range of D_S.

The measurements of the bipolar mode are reported in table 5.5 and plotted in figure 5.9. According to the simulations, the primary voltage at which the MEMS travel for D_S is V_P = 140 V. The intermediate voltage was swept for a wider required range from -25 V to 14.5 V and the displacements were measured. Since the required voltage for the bipolar operation is ±13.35 V, the reduction in the controlling voltage is almost 2.6 times smaller than the conventional. The simulations results are plotted for a wider V_I range than the measured power supply range, to show the minimum of the response curve.

Table 5.5. The measured displacement for unipolar mode, when V_P = 140 V, D_1 = 140 µm, D_2 = 490 µm, W_S = 300 µm and W_E = 16.7 µm.

V_I (V)	Displacement (µm)
-25	5
-15	8
-10	10
-5	13
0	18
3	24
6	28
8	30
10	34
11	37
12.1	40
12.9	44
13.7	47
14.2	49
14.5	50

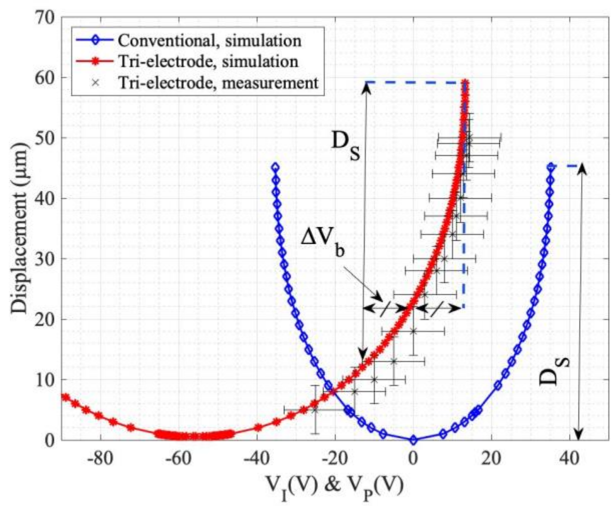

Figure 5.9. Displacement vs. controlling voltage (V_I or V_P) for bipolar mode when V_P = 140 V, D_1 = 140 µm, D_2 = 490 µm, W_S = 300 µm and W_E = 16.7 µm.

For the maximum displacement mode, the calculated primary electrode voltage (V_P = 80 V) was applied, and the intermediate electrode was swept from -28 to 40 V. Looking at the results, the maximum displacement is 59 µm which is almost 26% larger than the conventional snap-down displacement of D_S = 47 µm. The measurements are reported in table 5.6 and plotted in figure 5.10.

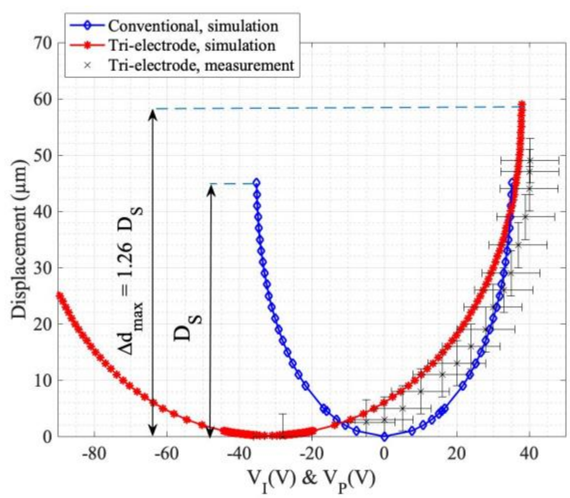

Figure 5.10. Displacement vs. controlling voltage (V_I or V_P) for maximum displacement mode when V_P = 80 V, D_1 = 140 µm, D_2 = 490 µm, W_S = 300 µm and W_E = 16.7 µm.

Table 5.6. The measured displacement for maximum displacement mode, when V_P = 80 V, D_1 = 140 µm, D_2 = 490 µm, W_S = 300 µm and W_E = 16.7 µm.

V_I (V)	Displacement (µm)
-28	0
-5	8
0	3
5	5
10	8
16	11
20	13
24	16
28	19
30	23
33	26
35	29
37	34
39	39
40	44
40.1	47
40.2	49

Tri-electrode -higher displacement range (table 5.2a configuration):

The measurements were carried out in order to find the maximum displacement when W_S = 450 µm. The results are summarized in table 5.7 and plotted in figure 5.11. We see that there is a very good agreement between the measurements and the simulations. The maximum displacement in this case is Δd_{max} = 69 µm, which is 33% larger than the conventional actuator snap-down displacement of D_S = 52 µm.

Table 5.7. The measured displacement for maximum displacement mode, when V_P = 140 V, D_1 = 155 µm, D_2 = 490 µm, W_S = 450 µm and W_E = 16.7 µm.

V_I (V)	Displacement (µm)
-25	16.4
-10	14
-15	10.8
-20	8.4
-25	7.2
0	20.5
5	24.2
10	27.9
15	33.4
20	40.6
25	56.4

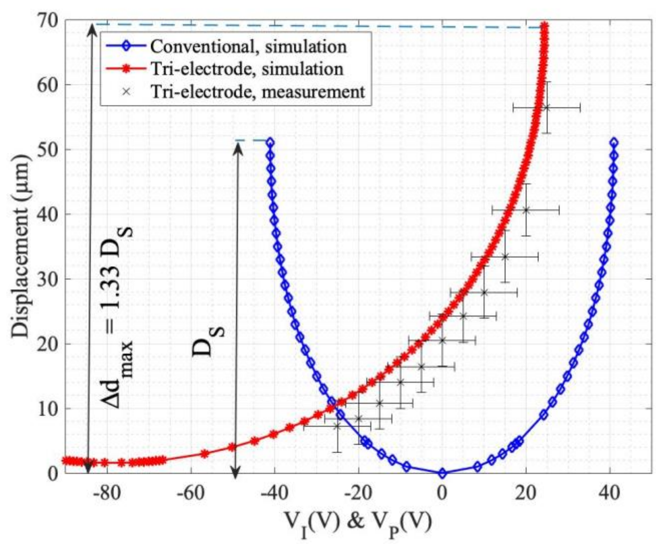

Figure 5.11. Displacement vs. controlling voltage (V_I or V_P) for maximum displacement mode when V_P = 140 V, D_1 = 155 µm, D_2 = 490 µm, W_S = 450 µm and W_E = 16.7 µm.

5.4.2 Narrow rectangular MEMS electrode (table 5.2 configuration)

The measurements were done by sweeping the controlling voltage from 0 to 28 V. The measured displacements are reported in table 5.8 and plotted in figure 5.12. We see that there is a close agreement between the measurements and the simulations. According to the simulations, the controlling voltage reduced by almost 23% (ΔV_u = 24.4 V) compared to conventional V_S = 30 V.

Table 5.8. The measured displacement for unipolar mode, when V_P = 93 V, D_1 = 120 µm, D_2 = 490 µm, W_S = 450 µm and W_E = 16.7 µm.

V_I (V)	Displacement (µm)
0	17.3
10	22.9
15	26.1
18	29.1
20	31.6
21	35
23	37.5
26	41.5
27	43.9
28	47.9

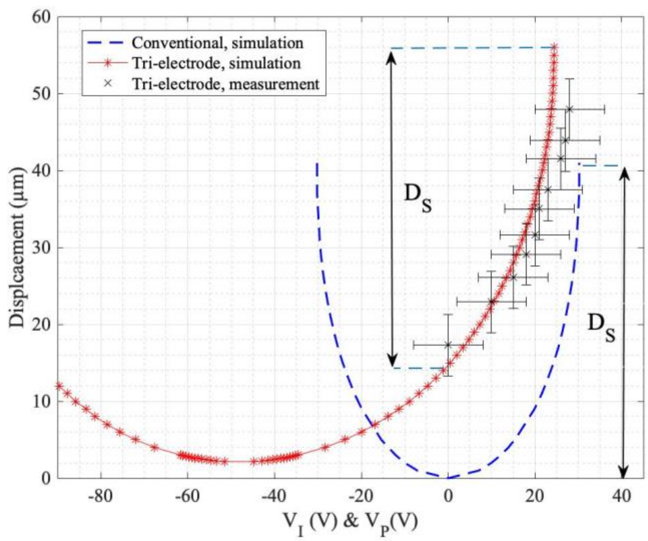

Figure 5.12. Displacement vs. controlling voltage (V_I or V_P) for unipolar mode when V_P = 93 V, D_1 = 120 µm, D_2 = 490 µm, W_S = 450 µm and W_E = 16.7 µm.

For the bipolar experiment the intermediate electrode voltage was swept from -12 to +18 V. The measured displacements are reported in table 5.9 and figure 5.13. The voltage reduction for the bipolar mode is almost 2.5 times since the controlling voltage is $\Delta V_b = \pm 12.26$ V.

Table 5.9. The measured displacement for unipolar mode, when V_P = 112 V, D_1 = 120 µm, D_2 = 490 µm, W_S = 450 µm and W_E = 16.7 µm.

V_I (V)	Displacement (µm)
-12	14
-5	18
0	22
5	25.7
10	31.8
15	37.9
17	41
18	45.8

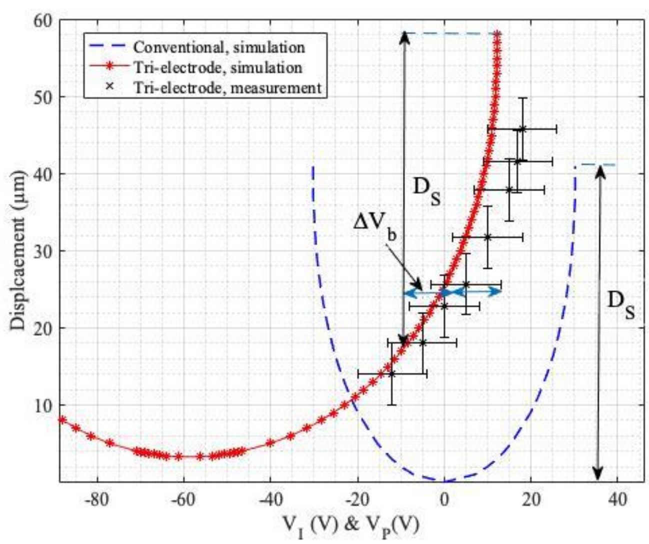

Figure 5.13. Displacement vs. controlling voltage (V_I or V_P) for bipolar mode when V_P = 112 V, D_1 = 120 µm, D_2 = 490 µm, W_S = 450 µm and W_E = 16.7 µm.

The measurement results of the maximum displacements are summarized in table 5.10 and plotted in figure 5.14. The displacement is increased almost 40% for the displacement of 56 µm compared to the conventional of D_S = 40 µm.

Table 5.10. The measured displacement for maximum displacement mode, when V_P = 70 V, D_1 = 120 µm, D_2 = 490 µm, W_S = 450 µm and W_E = 16.7 µm.

V_I (V)	Displacement (µm)
0	10.8
10	16.3
15	19.7
20	23.1
25	29.4
27	32.2
29	36.2
30	38.8
31.5	40.7
32.4	45

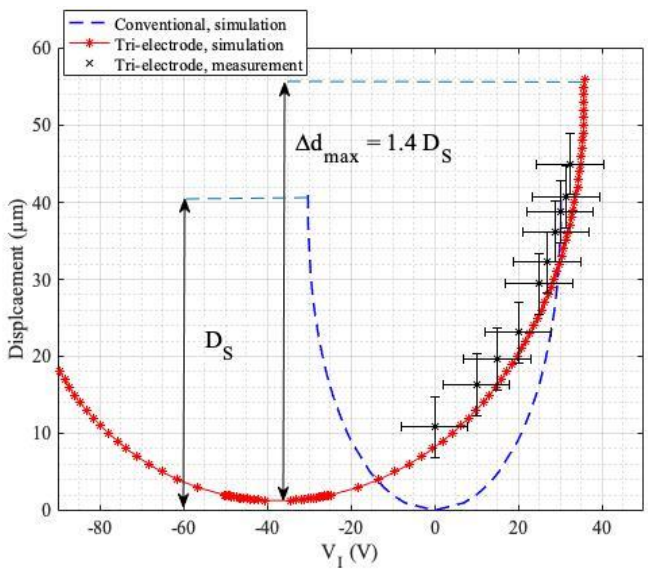

Figure 5.14. Displacement vs. controlling voltage (V_I or V_P) for bipolar mode when V_P = 70 V, D_1 = 120 µm, D_2 = 490 µm, W_S = 450 µm and W_E = 16.7 µm.

6

Fabrication and Stress Analysis of a Tri-layer Flexible Mirror

Contents

6.1 Introduction

In the first section of this chapter, the design, and thermal stress analysis of a tri-layer metal / SU-8 / metal mirror is explained. This mirror was introduced in [26] for a Lorentz force DM. However, there were always fabrication imperfections due to the manufacturing procedures. Since SU-8 polymer is utilized as the flexible layer, the cross-linked polymer is very sensitive to temperature. Therefore, a reliable fabrication technique is required to result in a smooth and wrinkle-free mirror. It also should be resistant to possible temperature variation during the mirror fabrication and functioning.

In this chapter, the fabrication steps for the tri-layer mirror are explained. At first, material stress analysis is studied, which is to explore the impact of the various processing steps of three stacking mirror layers, including the polymer and metal layer coatings, on the stress levels in each material. Following this discussion, fabrication steps for a complete 1.2×1.2 cm^2 square mirror are reported using the previous stress analysis results. The results were also applied to the fabrication of a 4.4×4.4 cm^2 mirror. This mirror is designed for a 20×20 array of actuators in an ongoing project at the Nanotechnology Research Centre, National Research Council of Canada (Edmonton), and Nano Fab - Fabrication & Characterization lab, at the University of Alberta. The recipe and the flowchart of the mirror fabrication are also summarized at the end of this chapter.

6.2 Design and methodology

The tri-layer flexible mirror consists of one flexible structural layer and two metal layers coated on both sides of the structural layer. One metal is considered the mirror face and the other is to cancel out the residual thermal stress between the first coated metal and the flexible layer. The flexible layer is SU-8, a negative polymer photoresist. The structure of the mirror is shown in figure 6.1 including the three stacking layers and the substrate.

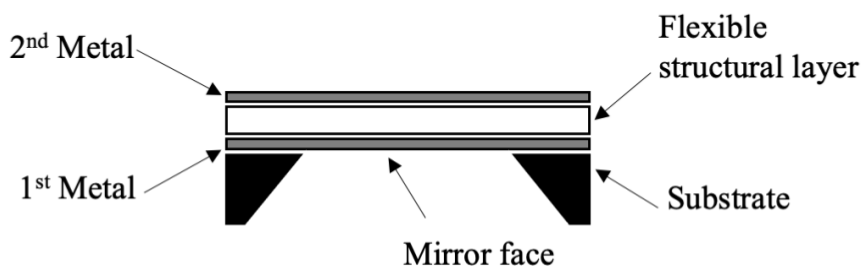

Figure 6.1. Tri-layer, metal/flexible layer/metal mirror for DMs.

In a multi-layer structure, stress between each layer can result in deformation of the mirror. An overall compressive stress can cause buckle delamination and wrinkles after the coating [79], however, tensile stress can help ensure acceptable flatness of the mirror. In selecting each material, and the processes used in their fabrication, we would want to ensure minimal residual thermal stress after the fabrication, which may involve elevated temperatures. For example, if a large thermal expansion coefficient difference exists between the first metal and the next material layer, possible curvature or wrinkling of the final mirror may occur. Selecting from a choice of different metals could then provide different stress. Therefore, in this work, the impact of two different metals was studied. Figure 6.2 shows the result of tensile and compressive stress between material layers, which can cause concave or convex curvature. Therefore, it was needed to study and design the mirror fabrication such that the ultimate stress after coating all three layers is tensile.

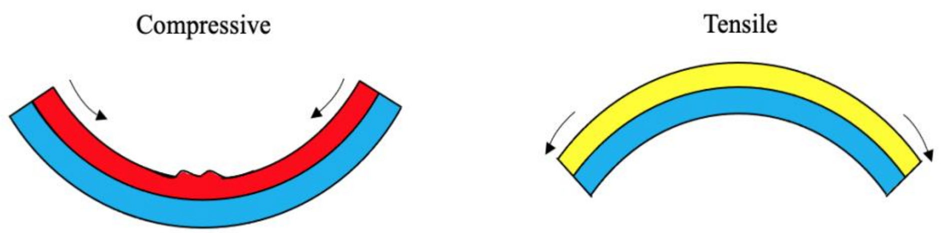

(a) (b)

Figure 6.2. The bent substrate with residual stress after being coated with thin films with different thermal expansion coefficients for when the stress is (a) compressive in the upper red material, and (b) tensile in the upper yellow material.

Experimental studies of the materials used in the mirror were done in the development of the flexible mirror process. During these studies, material stress levels were measured using the TOHO FLX-2320 machine (figure 6.3a) in order to understand the effect of fabrication processes on the residual stress in each material. The stress is calculated using the measured radius of curvature (ROC) of the coated substrate. The measurements were conducted before and after each step of coating and baking. The calculations then were carried out using Stoney's equation below [80]:

$$\sigma_f = \frac{E_s t_s^2}{6(1-\upsilon) t_f R}, \tag{6.1}$$

where t_s is the substrate thickness , υ is Poisson ratio of the substrate, E_S is the substrate Young's modulus, t_f is the thickness of the thin film, R is the substrate radius of curvature, and $E_S/(1-\upsilon)$ term is called biaxial modulus. Stoney's equation is utilized to calculate the stress between only two layers. However, in the case of coating more than one thin film, biaxial modulus of each coated layer and also mismatch strain between them should be considered [81]. Therefore, since the stress equation of multiple layers is complicated, the measured ROC was used to study the impact of residual stress. Stoney's equation parameters are displayed on figure 6.3b when there is a tensile stress.

(a)

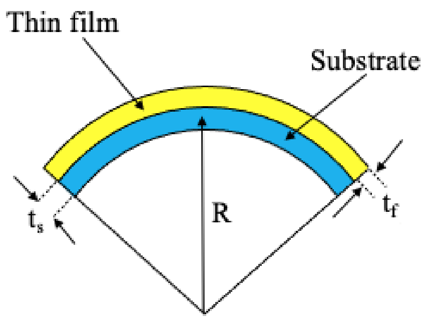

(b)

Figure 6.3. (a) TOHO FLX-2320 stress measurement machine. (b) The bent substrate after being coated with a thin film including the parameters uses in Stoney's equation to calculate the stress using measured ROC.

6.3 Stress Analysis

The fabrication of a thermally stable SU-8 material is very important for mirror fabrication. It is a polymer-based material, and therefore it can be adversely affected by elevated temperatures during the subsequent metal depositions (thermal evaporation or sputtering). Forming a stabilized, temperature-resistive SU-8 layer with maximum cross-links is required to have a predictable and reliable mirror structure. According to [82,83], SU-8 structural reliability is significantly dependent on the hard bake (HB) step. The SU-8 hard bake step affects the material properties of SU-8. The thermal stability of SU-8 depends on the processing time, temperature, and exposure. The temperature of the hard bake is not the only important parameter. The temperature holding time (THT) is also critical to keep continuing the polymerization process and make the polymer chain longer. Therefore, the effect of HB on SU-8 was studied. The SU-8 was fabricated by spin coating a layer of SU-8 on a silicon wafer and measuring the stress after different HB steps. Two different experiments were performed. In one experiment (case 1), the temperature was increased in different steps and the SU-8 was kept at that temperature for a fixed amount of time. In the other experiment (case 2), the stress and thickness of SU-8 were measured after holding at a fixed temperature but for different time periods in each step. The case 2 experiment was performed to see the influence of THT.

6.3.1 SU-8 on silicon wafer

The fabrication was started by spin coating SU-8 2025 (diluted with thinner at 1:1 ratio) on a 3-inch silicon wafer. The spin speed was 500 rpm for 15 sec in the spread mode and 1300 rpm for 30 sec for spin mode. Following this, the soft bake was done in two steps, first at 65 ℃ for 2 minutes and then at 95 ℃ for 10 minutes on the hot plate. The SU-8 was baked in two steps, in order to prevent any thermal shock to SU-8 that might cause cracks after removing the photoresist solvents. Then, the sample was exposed to UV light (30 mW/cm^2) for about 15 sec to form the cross-links between the polymer chains. The sample was again baked at the post-exposure bake (PEB) step with the same temperature and timing as the soft bake. This step is to activate the cross-linking further and prevent the SU-8 chains that are not cross liked during the exposure [84]. After each one of the soft bakes and PEB steps, the samples were cooled down slowly (over approximately 5 minutes) to avoid any bending, cracking, or peeling off. Following this, the HB step is done and its impact on the SU-8 ultimate stress is studied in cases 1 and 2.

In case 1, the HB started from 150 ℃ as recommended in the SU-8 2000 MICROCHEM company datasheet [85]. The temperature was raised in several steps by 25 ℃ steps up to 300 ℃. The sample was kept in the oven for 30 min for each step and then the stress was measured after cooling down. The thickness of the SU-8 in each step was measured using NanoSpec thin film thickness measurement and Woollam spectroscopic ellipsometry. The measured values with two different tools were similar (within 1-2%), and the thickness result found by the Woollam ellipsometer is shown in figure 6.4b. The thickness after each step of baking shows the HB impact on the shrinkage (in thickness) of the SU-8 layer. The stress and the thickness of the various measurements are illustrated in figure 6.4.

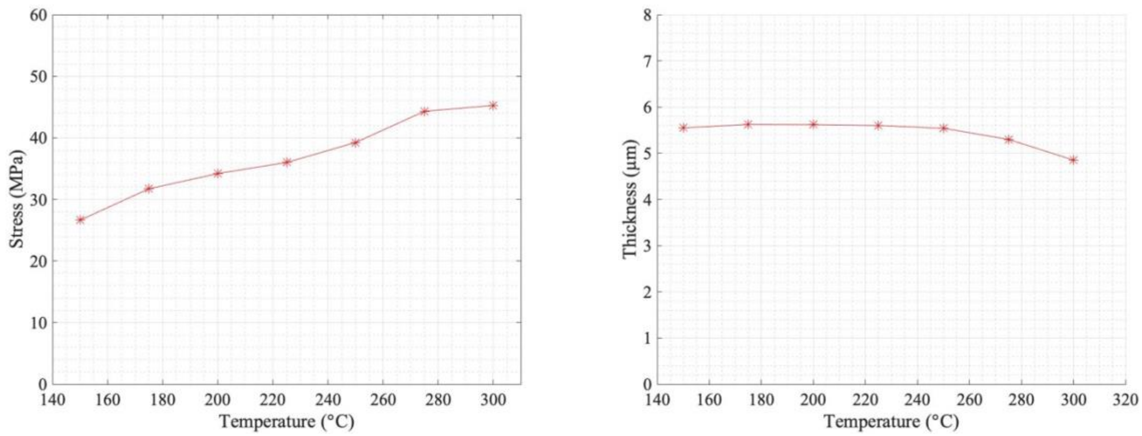

(a) (b)

Figure 6.4. Case 1 stress and thickness measurement with curves of (a) stress vs. temperature and (b) thickness vs. temperature.

As we see in figure 6.4a, the stress is positive (tensile) and increases by baking at higher temperatures. Looking at figure 6.4b, we see that the thickness starts dropping at about 275 °C. This temperature is an appropriate temperature for continuing our experiment to study the THT, since it is high enough to be stable during the following high-temperature physical depositions and it is below the SU-8 degradation temperature found in literature of around 380 °C [86]. Also, as recommended in the photoresist datasheet, the HB temperature is better to be 10 °C higher than the following steps of fabrication if they are high-temperature processes.

In case 2, the experiment was performed on two different silicon wafers called samples 1 and 2. In sample 1, the wafer was baked at 200 ℃ for 15 min in the oven. Then, the sample was again baked at 275 ℃ for three more times each for one hour. After each hour, the sample was cooled down and the stress and thickness were measured. In sample 1, the stress and thickness measurements were carried out for HB and after PEB, but in sample 2, the stress after soft bake also was measured to show the increase in stress before and after the first time HB. In sample 2, the wafer was baked for 10 hours at 275 ℃ and measurements were carried out every hour. The wafers (sample 1) after each time of baking are displayed in figure 6.5. The measurement results of case 2 are illustrated in figures 6.6 and 6.7. Looking at the results and comparing sample 1 and 2, we see that the major increase in the tensile stress happens after baking for the first time at 275 ℃. After more baking, even baking more than 10 more hours, the tensile stress increased not more than 10%.

In both samples, the stress sits between 40 - 50 MPa after the first-time baking. It can be an appropriate conclusion that two hours of baking at 275 ℃ is enough to improve the tensile stress in the HB step. The first hour is to reach the high-level stress from soft bake and the second one hour (which increases stress by almost 10%) results in an almost stable stress. The good news about the selected temperature is that the SU-8 is not damaged and baking the SU-8 is safe even for a long period of time.

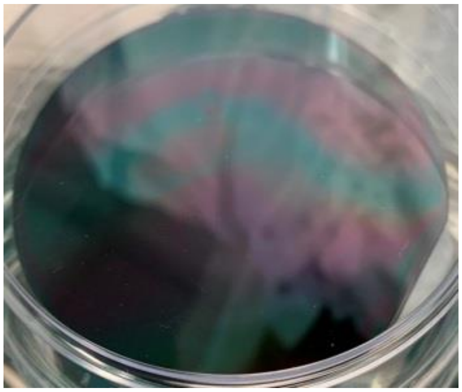

(a)

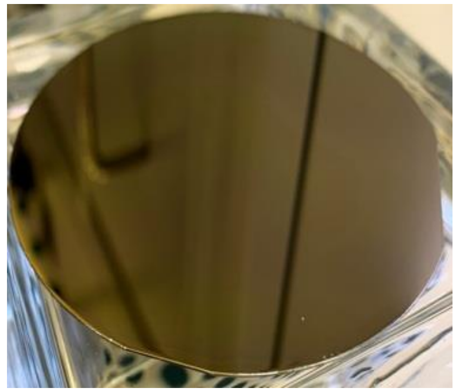

(b)

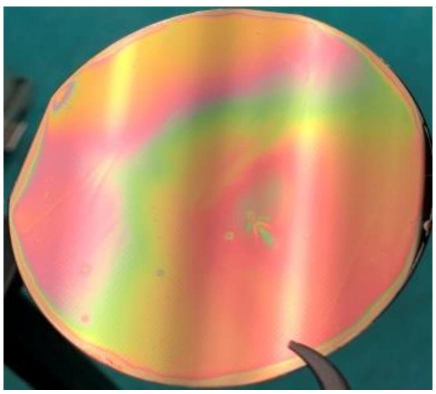

(c)

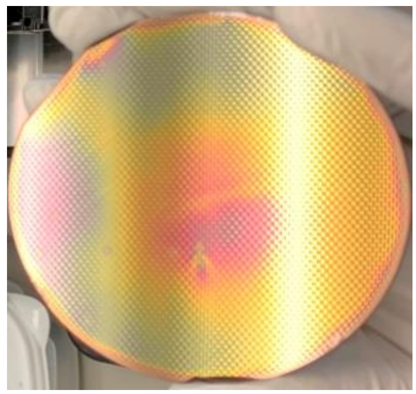

(d)

Figure 6.5. case 1 at a) 200 °C, 15 min, b) 275 °C, 60 min, c) 275 °C, 60 min for 2nd time and d) 275 °C, 60 min for 3rd time.

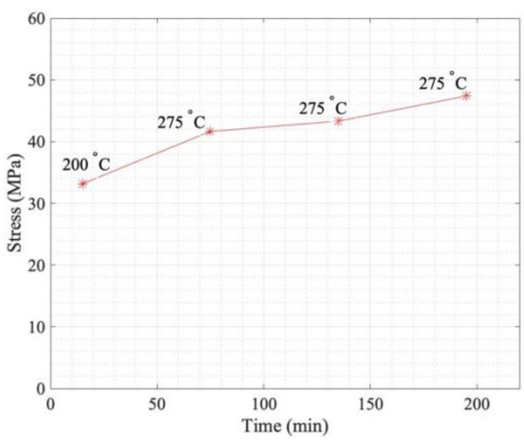

(a)

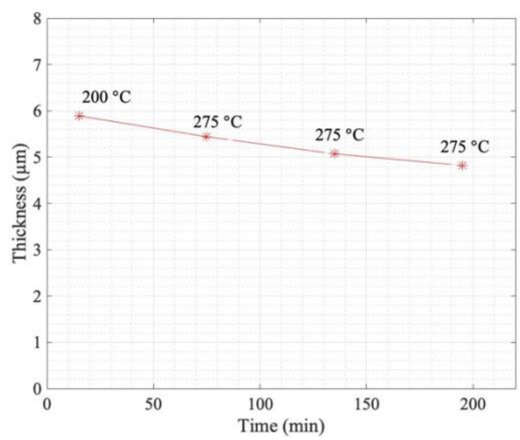

(b)

Figure 6.6. Case 2 (sample 1) stress and thickness measurement with curves of (a) stress vs. temperature and (b) thickness vs. temperature.

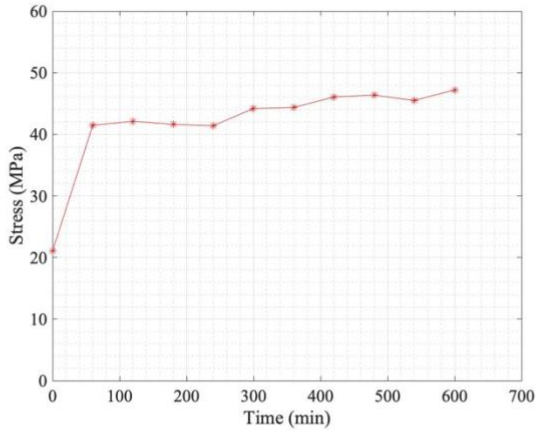

(a)

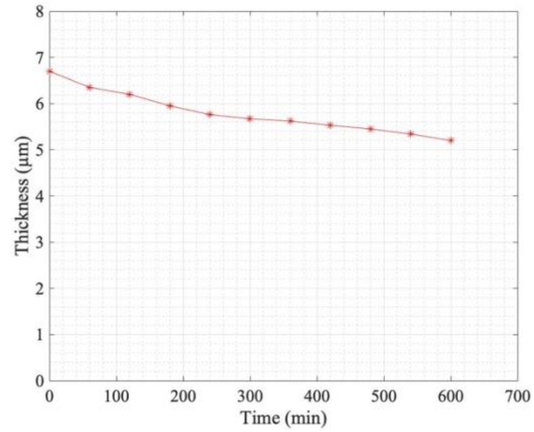

(b)

Figure 6.7. Case 2 (sample 2) stress and thickness measurement with curves of (a) stress vs. temperature and (b) thickness vs. temperature.

6.3.2 Metal/SU-8/Metal on silicon wafer

In this section, the effect of each of the three mirror layers on the overall stress was studied. The impact of the two different physical depositions of sputtering and thermal evaporation was also studied. In the experiments, the two metal layers and SU-8 were coated on a 3-inch silicon wafer and the stress was measured after each step of coating, depositing, and baking. The steps of fabrication are shown in figure 6.8. The goal was to find a process which resulted in an overall moderate tensile stress, to ensure mirror flatness.

Cr and Al were used in different samples, in order to see the effect of different metals on stress and investigate the various thermal expansion coefficients. The selected metals were coated on four silicon wafers using sputtering or thermal evaporation. The stress after each step of the coating was measured as summarized in table 6.1. In thermal evaporation, the Al or Cr deposition rate was about 0.85 nm/s and the final thickness was 100 nm. The thermal evaporation base pressure was 0.46 µTorr and the deposition pressure was 2 µTorr. Comparing Cr and Al, we see that the Cr gives a very high tensile stress while the Al stress is compressive (negative). For the rest of the coatings (deposition of more than one thin film layer), we look at the ROC, as the lower the ROC the higher the tensile stress (equation 6.1).

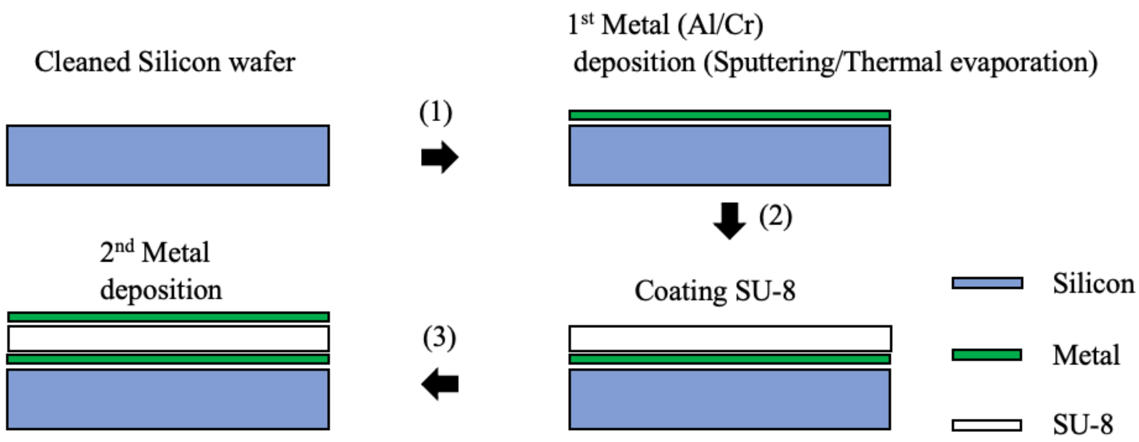

Figure 6.8. Three-layer coating on a 3-inch silicon wafer (1) deposition of the first metal (Al/Cr) using either sputtering or thermal evaporation, (2) coating SU-8 and (3) deposition of the second metal.

In the other samples, sputtering was used to coat Al and Cr with deposition rates of 0.21 nm/s and 0.37 nm/s respectively. The sputtering coatings were performed using 150W power (DC voltage) at the base pressure of 1.3 µTorr and deposition pressure of 1.7 mTorr. The argon flow used in the sputtering processes was 12 SCCM. Then SU-8 was coated and baked for 2 hrs at 275 °C. The recipe for coating SU-8 is the same as the recipe used in section 6.3.1. As we see in table 6.1, the Al also provides compressive stress compared to Cr in the sputtering. However, the compressive stress is larger in the sputtering. By coating SU-8 and then the second metal (using the same recipe as the first metal) in both cases of using sputtering and thermal evaporation, the compressive stress turns to tensile and the overall tensile stress increases. It can be due to the high-temperature process of coating, which essentially adds a step that is similar to hard baking the SU-

8 during the second metal high-temperature process. Looking at two different metals and two different deposition methods, it is observed that the thermal evaporation of Cr provides very higher tensile stress.

For the mirror itself, reflectivity is a primary importance. Al has a higher reflectivity than Cr, and so is would be used for the mirror surface itself (1st metal layer as shown in Figure 6.1). This could be covered by a thicker Cr layer (before the SU-8 coating), to give the stress characteristics of Cr if desired.

It can be also concluded by looking at figure 6.9, that Al has a higher reflectivity with respect to Cr. As we see in both cases of sputtering and thermal evaporation, the tensile stress increases (reducing ROC) after coating SU-8. However, it is still unknown whether the reason is due to the high-temperature SU-8 coating process annealing the 1^{st} metal or the SU-8 newly added layer itself resulting in the stress change. Thus, a new experiment was carried out to bake the first metal and measure the temperature after each step. Only Al metal was investigated, as it had the higher reflectivity.

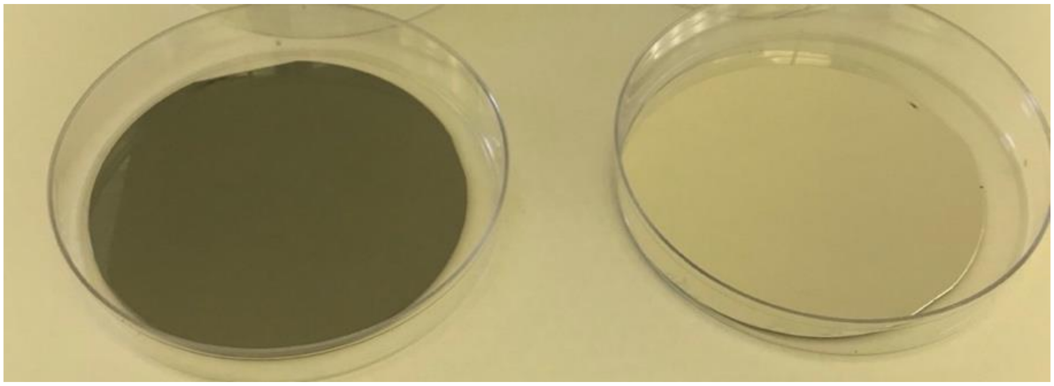

Figure 6.9. Samples coated with Cr/SU-8/Cr (left) and Al/SU-8/Al (right).The Cr coated wafer is darker and less reflective than Al.

Table 6.1. Measured stress after each step coating for Al and Cr using sputtering and thermal evaporation.

		1st Metal Stress (MPa)	Wafer ROC (m)	1st Metal ROC (m)	SU-8 ROC (m)	2nd Metal ROC (m)
Sputtering	Cr	+241.7	-308.6	102	14.7	13.6
	Al	-95.5	177.6	240.1	21.4	15.5
Thermal Evaporation	Cr	+1156.1	-105.3	74.8	16.4	13.9
	Al	-14.6	99.2	102.8	18.2	16.4

According to [87], when the Al crystallite size is smaller than the thickness of the entire coated layer, every high-temperature step such as following SU-8 soft bake and HB step results in the Al crystal grain growth to the point that the crystal size reaches to the coated Al layer thickness (metastable structure). Therefore, in a new experiment, a 100 nm of Al was deposited as the first metal layer using thermal evaporation. The thermal evaporation base pressure was 0.47 µTorr and the work pressure was 2-5 µTorr. After thermal evaporation, the thin Al layer was heated based on the heating cycles carried out for baking SU-8 including soft bake. Therefore, the wafer was heated at 65 ℃ for 4 min, and then heated up to 95 ℃ for 20 min (soft bake steps) using a hotplate, and then the stress was measured. In the next step, the wafer was baked for six hours, and stress was measured every hour. The annealing temperature was the same (275 ℃) as the temperature at which the SU-8 will later be hard-baked.

The measurements after each hour of baking (table 6.2) showed that the stress was almost unchanged after hour four. As we know (table 6.1), the stress of the Al deposited using thermal evaporation is compressive. Therefore, the deposition rate of thermal evaporation was increased to 3.6 nm/s in order to minimize the compressive stress during thermal evaporation. It was carried out by decreasing the time (higher deposition rate) that the wafer is exposed to the thermal evaporation's high-temperature source. After developing an Al layer with stable stress at the processing temperature, the SU-8 layer was coated and then baked for two hours at 275 ℃. The stress was measured after two stages of soft bake and HB. The recipe for coating SU-8 is the same recipe used in section 6.3.1. Following this, the second Al was sputtered at 0.21 nm/s deposition rate with the recipe used in section 6.3.2. Then the sample was baked for two hours at 275 °C. The ROC of the wafer was measured after each step of fabrication and the results are reported in table 6.2. The measured values show that by baking the Al after coating (thermal evaporation), the compressive stress turned to tensile, and it was observed to increase by continue baking. Coating with SU-8 also decreased the ROC (increase the tensile stress) and this trend continued by baking SU-8 and coating the second metal and with subsequent baking. The results of this study were published in the IEEE Canadian conference on Electrical and Computer Engineering 2021 [88].

Table 6.2. The measured stress and ROC after each step of fabrication and baking.

		Process	ROC (m)	Stress (MPa)	Thickness (μm)
Layers	Silicon wafer	-	3930.0	-	375
	1st Al	Thermal evaporation	-2440.0	-28.1	0.1
		Annealing (1st hr)	359.3	107.0	0.1
		Annealing (2nd hr)	122.5	334.5	0.1
		Annealing (3rd hr)	183.9	219.2	0.1
		Annealing (4th hr)	120.7	339.8	0.1
		Annealing (5th hr)	118.2	347.0	0.1
		Annealing (6th hr)	119.7	346.6	0.1
	SU-8	Soft bake	44.1	-	~ 5.5
		Hard bake (2 hours)	24.2	-	~ 5.5
	2nd Al	Sputtering	20.1	-	0.1
		Annealing (1st hr)	15.5	-	0.1
		Annealing (2nd hr)	15.4	-	0.1

6.4 Mirror fabrication

The stress study results in the previous section were utilized to build two mirrors with two different sizes. One was a 1.2 × 1.2 cm^2 square mirror for a 5 × 5 array of actuators and the other one a 4.4 × 4.4 cm^2 mirror for a 20 × 20 array of actuators. The entire required fabrication steps are reported here in this thesis; however, the release step will be performed later at Nanotechnology

Research Centre, National Research Council of Canada (Edmonton), and Nano Fab - Fabrication & Characterization lab, at the University of Alberta.

6.4.1 Fabrication of a 1.2 × 1.2 cm^2 mirror

In this section, a complete fabrication procedure is reported which was employed to build a square flexible mirror. All the main steps are shown in figure 6.10.

The mirror fabrication started with cleaning the silicon wafers with piranha. Piranha is a solution with 4:1 mixture of sulfuric acid and hydrogen peroxide which is used to clean the organic residues. Then the wafers were oxidized in the thermal oxidation silicon furnace.

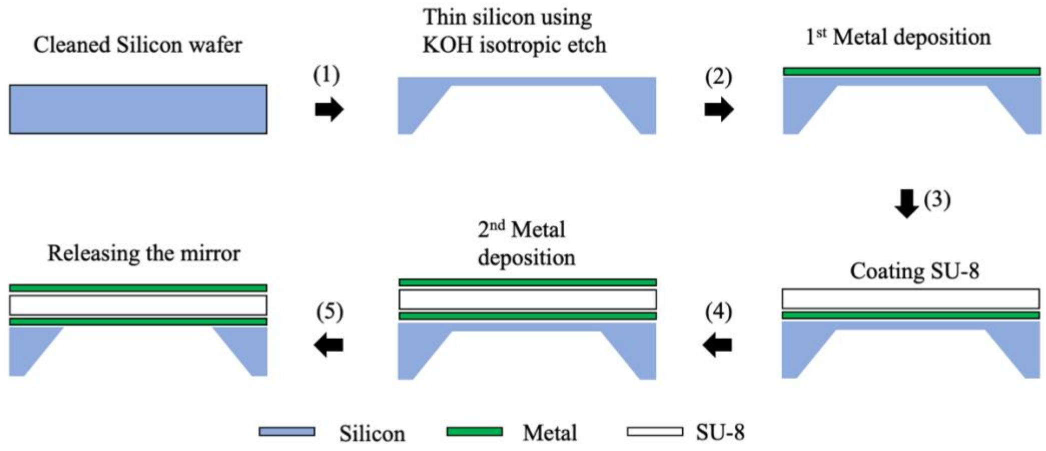

Figure 6.10. The tri-layer mirror fabrication on a 3-inch silicon wafer (1) Thinning the silicon wafer using KOH isotropic etch, (2) deposition of the first metal (Al/Cr) using thermal evaporation, (3) coating SU-8, (4) deposition of the second metal using sputtering and (5) releasing the mirror using RIE plasma etch and XeF_2 silicon etch.

Wet Oxidation

The cleaned 3-inch wafers were put in an oxidation furnace at 1100 °C for 16 hours. The wafers were exposed to water vapour (wet oxide growth) during the oxidation to form the thicker oxide. Wafers were loaded in a quartz wafer carrier in a row and moved from back to front along with 180˚ rotation every four hours to have uniform oxide growth across the surface. The oxidized wafers are shown in figure 6.11.

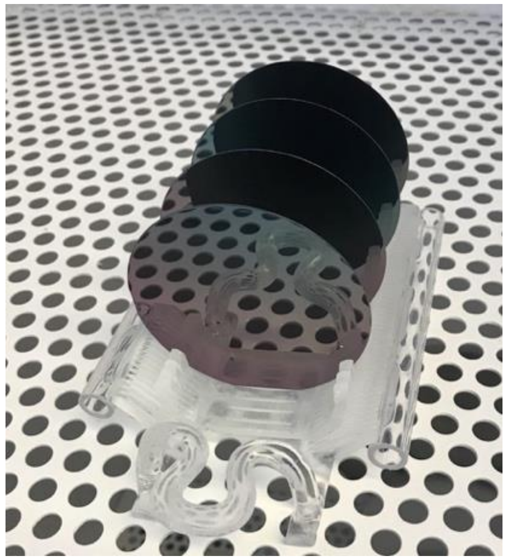

Figure 6.11. Four oxidized silicon wafers on the quartz tray after unloading from the hot furnace.

Patterning the oxide

Following the oxidation, the wafers were cut in square shape sizes using the wafer saw. Then, a dehydration bake was done at 115 °C for 3 minutes using hot plate to remove the humidity from the surface of the sample. Dehydration is necessary to increase the adhesion of the photoresist. Following this, HMDS curing was done for 5 min at 150 °C to improve the adhesion between forms SiO_2 and the photoresist. HMDS (hexamethyldisilane) is a chemical compound used as an adhesion promoter in lithography. HMDS curing is a common method used to enhance surface adhesion before spinning the photoresists. This treatment helps removing the absorbed humidity mostly from the hydrophilic substrates such as silicon and silicon dioxide. The hydrophobicity of the substrate is not desired as it causes the coated photoresist easily delaminated during developing or during the subsequent wet etch steps. The hot HMDS gas makes bonds with the remaining OH groups (after dehydration) of the substrate surface and removes them, then the substrate becomes hydrophobic. Following this, HPR 504 positive photoresist was used to pattern the oxide. However, the positive PR did not adhere to the sample appropriately, even with baking the samples and doing HMDS curing. The problem was due to the weak adhesion between the coated PR and the oxide surface. The sample after spin coating the photoresist is shown in figure 6.12a, and we can see that the photoresist is not well adhered. Therefore, a very thin 50 nm layer of Cr was coated on the oxide using sputtering to increase the adhesivity of the photoresist. The experiment results showed that the added Cr layer resolved the adhesion problem. The only problem with the new Cr layer is that the extra sputtering and etching steps are added to the entire fabrication process. As the pattern should be done on one side of the sample, the other side also is covered with PR. The final recipes are as follows:

Cr sputtering recipe:

- Base pressure: 1.7 μTorr.
- Argon gas flow: 12 SCCM.
- Deposition pressure: 1.8 mTorr.
- Thickness: 50 nm.
- Power: 150 W.

Lithography recipe:

Front side:

- Cr deposition: sputtering 50 nm of Cr.
- Spin speed: 500 rpm for 10 sec of spread mode and 1500 rpm for 30 sec of spin mode.

- Soft bake using hotplate: 115 °C for 120 sec.
- Developing: Using HPR 504 developer for 30 sec.
- Hard Bake (HB) using hotplate: 125 °C for 120 sec.

Back side:

- Cr deposition: Sputtering 50 nm of Cr.
- Spin speed: 500 m for 10 sec of spread and 1500 rpm for 30 sec of spin coating.
- Soft bake using oven: 120°C for 20 min.
- UV exposure: 30mW/cm2 for 5 sec.
- Developing: Using HPR 504 developer for 60 sec.
- Hard Bake (HB) using oven: 12 °C for 30 min.

The thickness of the photoresist after hard bake was 0.71 µm. Figure 6.12b shows the sample coated with photoresist after sputtering Cr.

After coating and patterning the photoresist on both sides, the Cr was etched with Cr etchant for 6 min to expose the oxide. Then, after rinsing the sample with DI water and drying with N_2, the oxide was etched on the patterned area using buffered hydrofluoric (BHF) acid (ammonium fluoride and hydrofluoric acid (HF) with a ratio of 10:1) for 60 min. In the next step, the sample was cleaned with DI water, and the photoresist was removed using Acetone and IPA. Again, we etched the Cr for 6 min to have only oxide on the silicon. The backside patterned oxide is shown in figure 6.12c, the front side is also covered with oxide, to protect the silicon from being etched in the next KOH silicon etch step.

KOH anisotropic etch:

A 30 % KOH solution was employed to etch the silicon. The 30% KOH is a mixture of solid potassium hydroxide in a specific amount of DI water. A few samples were utilized in order to avoid repeating the entire procedure due to the probable damages such as over-etch or broken samples. The samples were etched in two different procedures to have different silicon thicknesses in the cavity. In the first round, 260 µm of two samples were etched for 4 hours and 50 minutes at 80 °C. The remaining silicon thickness inside the etched cavity was almost 120 µm. In the next round, another sample was etched in three steps of 150 min, 180 min, and 22 min to be able to measure the exact thickness of silicon in each step and have the more uniform etched cavity by rotating the sample each time. The thickness of silicon after these steps was 55 µm. Etching was stopped because the remaining oxide thickness was almost 75 nm, and it was not wanted to expose the front side to the etching solution. The front side should be protected to have its original smoothness quality for the mirror. The sample after etching in KOH solution is shown in figure 6.12d. In the next step the remaining oxide mask was removed using BHF acid.

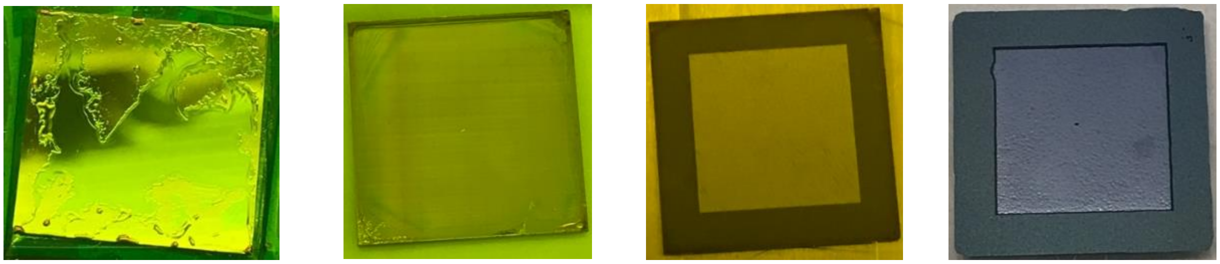

(a) (b) (c) (d)

Figure 6.12. Square mirror after (a) spin coating the positive HPR 504 photoresist (week adhesion), (b) Cr coating then spin coating the positive HPR 504 photoresist (strong adhesion and uniform coating), (c) patterning and etching oxide and (d) etching silicon with KOH etchant to thin the silicon.

The roughness of the silicon inside the etched cavity was measured after the KOH etch and also after the plasma etch, as illustrated in figure 6.13 with 5x magnification (location #6 of figure 6.14). The measurements were carried out to compare the impact of two different etch methods. The roughness was measured using the equation below:

$$R_a = \frac{1}{L_S} \int_0^{L_S} |Y_S| \, dx \,, \qquad (6.2)$$

where L_S is the length of scan and Y_S is the vertical displacement. The roughness was measured at six points on the cavity, shown in figure 6.14, and summarized in tables 6.3 and 6.4. The roughness profile was measured at the center of the cavity (location # 5) using Tencor Alphastep 500 profilometer, as shown in figure 6.15. It can be seen from the tables that the average roughness for both scan length of L_S = 1, 0.5 mm are larger after plasma etch than after KOH etch.

(a) (b)

Figure 6.13. The cavity surface after (a) KOH etch and (b) plasma etch.

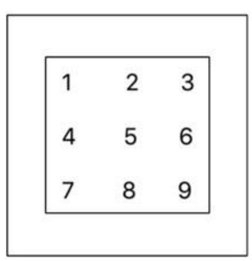

Figure 6.14. The locations where the roughness is measured.

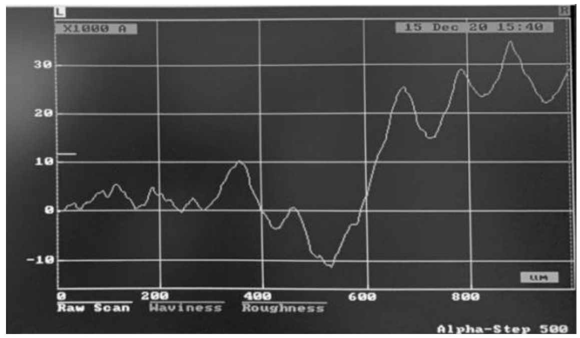

(a)

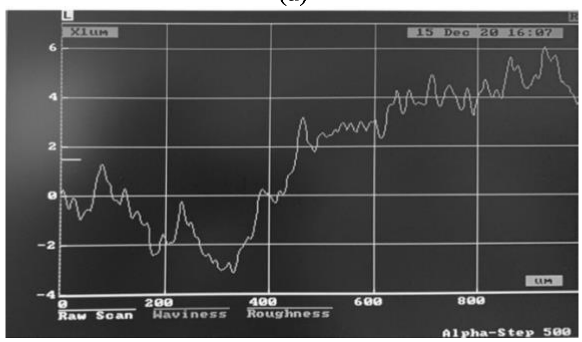

(b)

Figure 6.15. Roughness scan at the center of the cavity (location #5) of a 1 mm scan length for both cases of after (a) KOH etch and (b) plasma etch.

Table 6.3. The measured roughness (R_a) in µm at nine locations for three different scan lengths (2, 1, 0.5 mm) after KOH etch. The calculated roughness unit is µm.

		Scan length		
		2 mm	1 mm	0.5 mm
Locations	1	1.2113 µm	1.4121 µm	1.4052 µm
	2	1.030 µm	0.783 µm	1.0854 µm
	3	1.1769 µm	1.1549 µm	0.4771 µm
	4	0.7017 µm	0.7534 µm	0.2999 µm
	5	1.1454 µm	0.6271 µm	0.24 µm
	6	1.0387 µm	1.0941 µm	0.7181 µm
	7	0.7808 µm	0.6398 µm	0.354 µm
	8	1.2378 µm	0.8394 µm	0.938 µm
	9	1.2353 µm	1.1218 µm	0.8393 µm
Average		1.062 µm	0.9362 µm	0.7063 µm

Table 6.4. The measured roughness (R_a) in µm at nine locations for three different scan lengths (1, 0.5, 0.05 mm) after plasma etch. The calculated roughness unit is µm.

		Scan length		
		1 mm	0.5 mm	0.05 mm
Locations	1	0.8557 µm	0.5548 µm	0.3199 µm
	2	1.348 µm	1.4989 µm	0.4673 µm
	3	1.1939 µm	1.0797 µm	0.3494 µm
	4	0.854 µm	0.7555 µm	0.3908 µm
	5	1.0689 µm	1.2173 µm	0.3032 µm
	6	0.8328 µm	0.9868 µm	0.2614 µm
	7	1.15 µm	1.1723 µm	0.2263 µm
	8	0.9421 µm	0.4895 µm	0.3929 µm
	9	1.043 µm	0.7091 µm	0.194 µm
Average		1.032µm	0.9404µm	0.3228 µm

Following the KOH etch step, the three layers of 1st Al, SU-8 and the 2nd Al were coated on the other side of the sample using the recipe of the previous section (table 6.2). The last step of the mirror fabrication was to use RIE plasma etch to thin the silicon from almost 50 to 10 µm and remove the remaining silicon using the XeF_2 silicon etch. The recipe was already developed by B. Park [89].

6.4.2 Fabrication of a 4.4 × 4.4 cm^2 mirror

A glass lithography mask was designed and built, in order to make a 4.4 × 4.4 cm^2 mirror, as shown in figure 6.16a. This is based on the mask designed for the 20 × 20 array of actuators. The fabrication steps are similar to the previous mirror. Here, the details of the fabrication steps are reported.

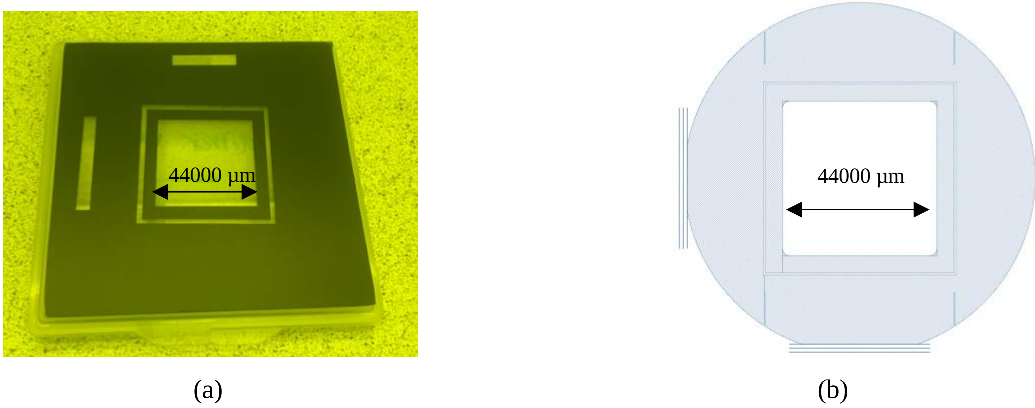

Figure 6.16. (a) Mask made in the cleanroom with black tape and a 5-inch glass and (b) the designed GDSII format mask design.

The fabrication of the mirror includes two main steps of thinning the silicon wafer for the mirror membrane and coating the three metal/SU-8/metal layers. The first step is summarized in figure 6.17, and the fabrication details are reported in table 6.5. The second step is shown in figure 6.18 and reported with its details in table 6.6.

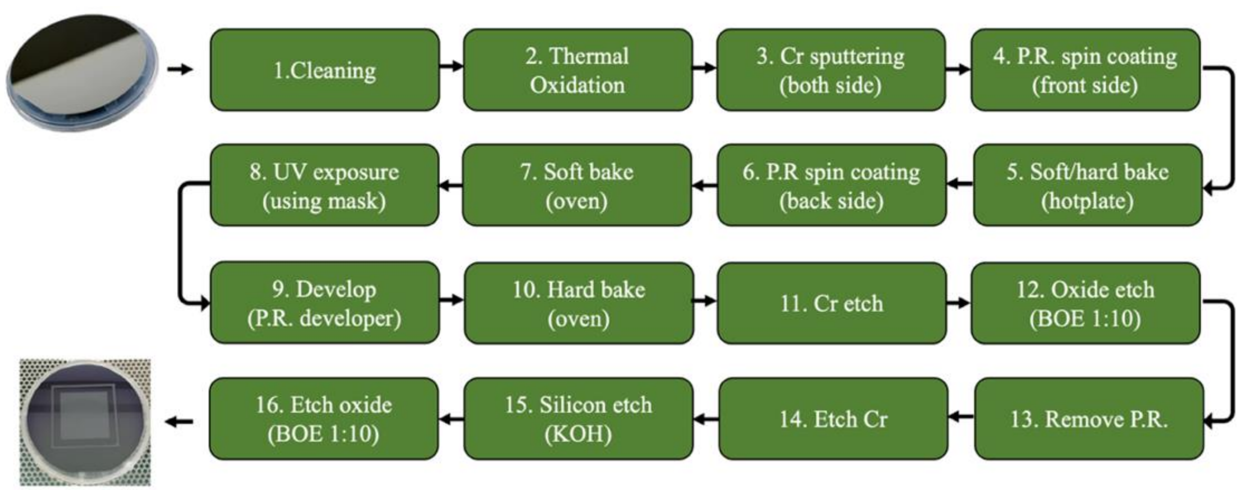

Figure 6.17. Flowchart of the first fabrication step of the tri-layer polymer-based metal/SU-8/metal mirror.

Table 6.5. First step of tri-layer polymer-based metal/SU-8/metal mirror.

	Process	**Time**	**Thickness**	**Comments**
1	Clean wafer	10 min	-	Piranha clean (1100 ml H_2SO_4 and 300 ml H_2O_2)
2	Thermal oxidation	22 hrs	2.5 µm	Wet oxidation at 1100 °C
3	Sputtering (DC) Cr	-	200 nm	Ar flow: 12 SCCM, P_{base}: 2.5 µTorr, $P_{working}$:1.1 mTorr, Power: 150W
4	Spinning Photoresist (HPR 504)	40 sec	1-2 µm	HPR 504 photoresist spread at 500 rpm (10 sec) and spin at 2000 rpm (30 sec)
5	Soft/hard bake	2 min	-	Baking on the hot plate at 125 °C
6	Spinning Photoresist (HPR 504)	40 sec	1-2 µm	HPR 504 photoresist spread at 500 rpm (10sec) and spin at 2000 rpm (30 sec)
7	Soft bake	20 min	-	Bake in oven at 120 °C
8	UV exposure	5 sec	-	Expose with UV light at 265 mW/cm^2
9	P.R. Develop	120 sec	-	Develop in photoresist 504 developer
10	Hard bake	30 min	-	Bake in the oven at 120 °C
11	Etch Cr	3 min	200 nm	Etch Cr in Cr etchant (patterning)
12	Etching oxide	45 min	2.5 µm	Etch oxide in BOE 10:1
13	Remove resist	2 min	-	Remove photoresist with acetone and IPA
14	Etch Cr	3 min	200 nm	Etch Cr in Cr etchant
15	Etch silicon	270 min	260 µm	Etch silicon in KOH to etch 260 µm silicon. The remaining silicon membrane is 40-50 µm.
16	Etching oxide	45 min	2.5 µm	Etch the thermal oxidation oxide mask

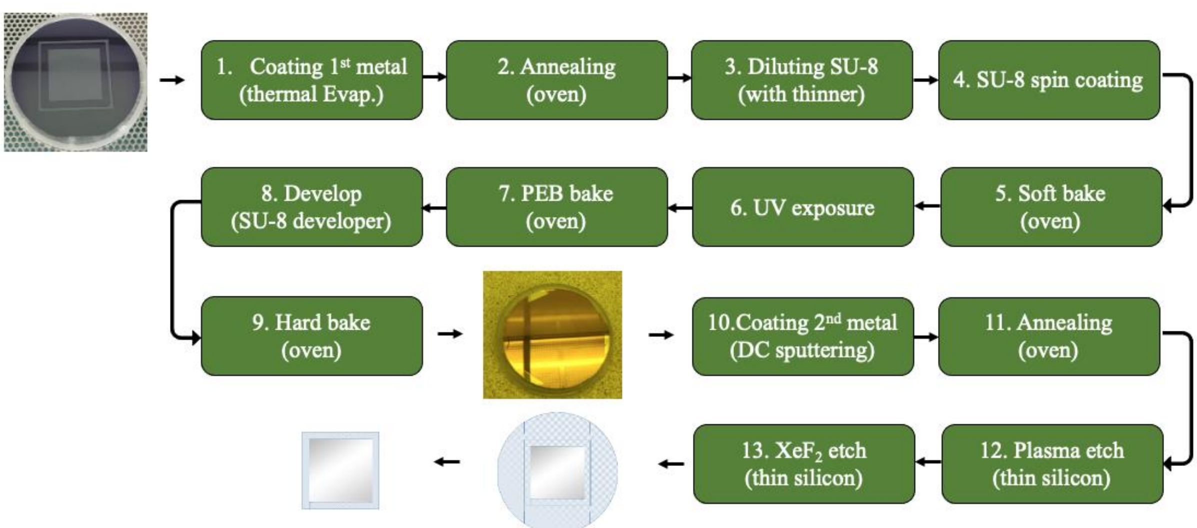

Figure 6.18. Flowchart of the second fabrication step of the tri-layer polymer-based metal/SU-8/metal mirror.

Table 6.6. First step of tri-layer polymer-based metal/SU-8/metal mirror.

	Process	**Time**	**Thickness**	**Comments**
1	Coating Al/Au	2 min	250 nm	Thermal evaporation P_{base}:0.46 µTorr, $P_{working}$: 2 µTorr
2	Annealing	3hrs	-	Bake in oven at 275 °C
3	Diluting SU-8	-	-	Diluting SU-8 with thinner (1:1 ratio)
4	Spinning SU-8	45 sec	4-5 µm	SU-8 spread at 600 rpm (15sec) and spin at 1800 rpm (30 sec)
5	Soft bake	12 min	-	Baking on the hot plate at 65 °C (2 min) and again baking at 95 °C (10 min)
6	UV exposure	15 sec	-	Expose the UV light at 265 mW/cm^2
7	PEB bake	12 min	-	Post Exposure Bake (PEB) on the hot plate at 65 °C (2 min) and again baking at 95 °C (10 min)
8	SU-8 Develop	120 sec	-	Develop in SU-8 developer
9	Hard bake	3 hrs	-	Bake in oven at 275 °C
10	Coating Al/Au	30 min	250 nm	Sputter (DC) the 2nd metal
11	Annealing	2hrs	-	Bake in oven at 275 °C
12	Plasma etch	3hr	35 µm	Etch the 35 µm of the thin 40 µm silicon membrane
13	XeF_2 etch	N/A	5 µm	Etch the remaining 5 µm of the thin 40 µm silicon membrane

The mirrors after coating three layers and ready to release are shown in figure 6.19. The final step of the mirror fabrication, which is releasing, is planned to be carried out at Nanotechnology Research Centre, National Research Council of Canada (Edmonton), and Nano Fab - Fabrication & Characterization lab, at the University of Alberta.

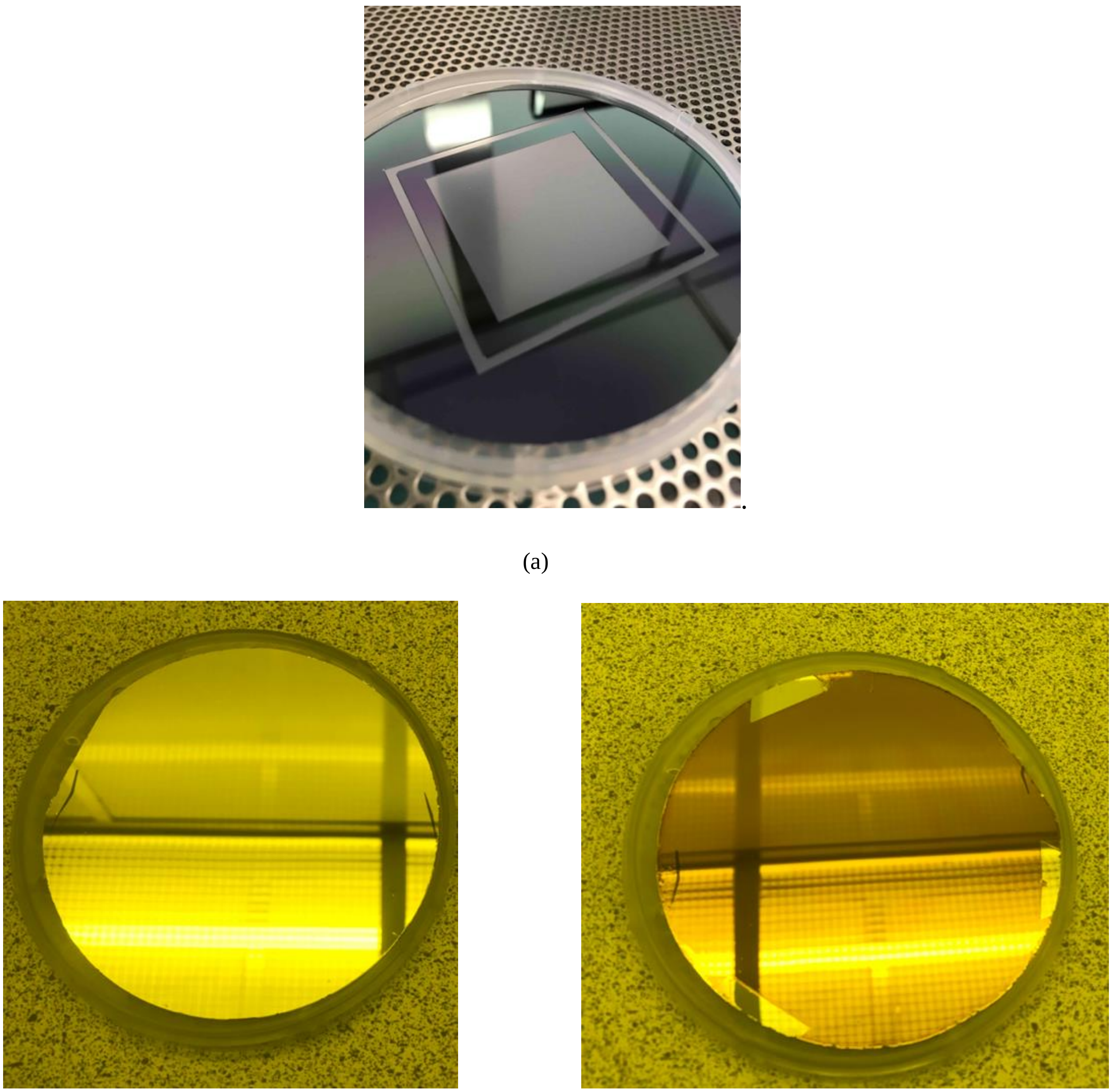

(a) (b) (c)

Figure 6.19. 4-inch wafers after (a) KOH etch, (b) coating first Al and (c) coating SU-8.

6.5 Conclusions

Investigations showed that having a flat and smooth flexible mirror is a necessity for a DM operation. A process was developed to enable a tri-layer polymer-based flexible mirror for DMs, in order to solve the issue of material stress and to produce a mirror with adequate flatness and stable thermal structure. In this work, the effect of a high-temperature fabrication on the stress of a mirror was studied. A controlled level of tensile stress is required to have a wrinkle and buckle-delamination-free mirror surface. To do so, the SU-8 HB temperature and the baking time for having a thermally resistant flexible layer were studied. Two different metals Cr and Al were used to see the impact of different thermal expansion coefficients, and both sputtering and thermal evaporation methods were investigated for metal deposition. The results are summarized as follows:

- Baking SU-8 at 275 °C for almost two hours increases the tensile stress.
- Thermal evaporation is preferred over the sputtering for the first metal in terms of having smaller compressive stress or higher tensile.
- Cr has a very higher tensile stress than Al, but Al also provides an acceptable level of tensile stress with higher reflectivity that is required for a mirror.
- Annealing metals after coating helps to stabilize the metal stress, and also increases its tensile stress.
- The results were employed to build 1.2 × 1.2 cm^2 and 4.4 × 4.4 cm^2 mirrors for ongoing DM design and fabrication at Nanotechnology Research Centre, National Research Council of Canada (Edmonton), and Nano Fab - Fabrication & Characterization lab, at the University of Alberta.

7

Conclusions and Future work

Contents

7.1 Summary

Adaptive Optics (AO) is a method used to correct the received distorted wavefronts. A deformable mirror (DM) is one of the building blocks of an AO system. Various technologies of magnetic, thermal, piezoelectric, and electrostatic actuators were utilized to control the deformation of a DM. MEMS technology has been vastly used to develop DMs over the last few decades. Electrostatic actuators are one of the preferred technologies compared to the other three technologies (magnetic, thermal, and piezoelectric) due to the low voltage and simple existing batch microfabrication techniques already developed for IC technology.

This thesis focused on studying a MEMS tri-electrode electrostatic actuator. The newly developed tri-electrode configuration is highly useful for applications in need of arrays of actuators. Thus, the tri-electrode topology can be a great actuator for DMs. Also in this thesis, the issue of the fabrication of a flexible mirror was studied by examining the impact of different materials and deposition techniques.

The study in this thesis began by looking at the theory of electrostatic actuators and the applications of single and multiple electrostatic actuators. Arrays of electrostatic actuators have been used for many applications and their issues might be different from using a single one. The Pull-in effect is the phenomenon that limits the actuator's range of motion to one-third of the initial gap. To increase the range, the initial gap should be larger which results in an even larger controlling voltage. Therefore, the large controlling voltage is another major problem of electrostatic actuators. Several techniques which used to overcome the pull-in effect were studied in this work.

Following this, the tri-electrode actuator and the RSFM modeling method were introduced to study the actuator's performance. It was shown that the controlling voltage could be reduced up to four times smaller than a conventional actuator controlling voltage. It was also shown that the travel range could be increased by 70% larger than the conventional actuator for a specific design. Following, the impact of the materials different than air between fixed electrodes was investigated and it was concluded that the larger the dielectric constant of the material, the larger fixed controlling voltage was required.

An extended electrode tri-electrode actuator was also introduced to increase the range of motion as high as 2.5 times that of a conventional actuator. In this design, the fixed primary electrode of the tri-electrode actuator was extended to the sides and the corresponding fringing fields were used to control the displacement of the mobile electrode in both directions. The extended electrode actuator is a bidirectional actuator which is beneficial as opposed to the conventional electrostatic actuator which can only be controlled in one direction.

Two silicon-based moving MEMS electrodes were designed and built in cleanroom and were employed to test the performance of the tri-electrode actuator. The experiments showed a close agreement between the FEM numerical analysis and the measurements.

In addition to the studies which were performed to investigate the performance of the electrostatic actuators, a polymer-based flexible mirror fabrication was studied for its flatness problems when used in a DM. A previously developed metal/SU8/metal mirror had significant wrinkles and nonuniformities after release. Stress analysis studies were performed to investigate the possible microfabrication techniques, materials and parameters influencing the final product. The results were very promising and sample mirrors were built using the developed new fabrication technique.

7.2 Concluding Remarks

The tri-electrode actuator was studied in this thesis and the research studies showed the following features:

- Compact MEMS:

  The tri-electrode actuator has only an extra perforated electrode added between two electrodes of a conventional parallel plate actuator for the same original size. This topology can be applied to the existing actuators.

- Low controlling voltage:

  The tri-electrode actuator is an appropriate actuator with low controlling voltage. The lower control voltage is feasible by having a large, fixed voltage at a further distance and the lower controlling voltage at a close distance from the moving electrode. The controlling voltage is a function of the distance between the fixed electrodes. The larger the gap, the smaller the controlling voltage. However, the fixed voltage is larger which can be accepted considering the system design limitations.

- Large displacement range:

  The tri-electrode actuator can be used to increase the range of motion compared to the conventional actuator. The mode is called maximum displacement and occurs at a different background fixed voltage than when a smaller controlling voltage is required.

- Low volume wiring:

  The tri-electrode is specifically compatible with array-based applications. In array implementations, the wiring is a critical issue when hundreds and thousands of actuators are required. The high-voltage wirings are very bulky and sometimes not compatible with integrated systems. Tri-electrode topology with one common high voltage disregard the need of high voltage wiring and only one high voltage wire is enough when the controlling voltage is provided with integrated circuits.

- The extended displacement range:

  The extended tri-electrode is useful for very extensive bidirectional motion control. This feature is not available in many electrostatic actuators. Therefore, the actuator can be employed for a wider range of applications.

The thermal stress analysis of the polymer-based flexible mirror showed that:

- Baking the SU-8 negative polymer photoresist after developing an increase in the tensile stress.
- Thermal evaporation is a preferred method in coating metal as reaching to higher tensile stress and less winkle mirror.
- Baking after coating metals also helps to increase the final stress.

7.3 Future Work

The tri-electrode actuator was primarily designed for the purpose of using it for array implementations. The studies were validated by designing and building two single actuators for different intermediate electrode gap spacings. However, the ultimate goal of the design and fabrication of this actuator is to build a DM. Therefore, as future work the following studies can be performed:

- Design and study the performance of a 5 × 5 array of actuators and study the effect of each actuator on the adjacent actuators.
- Fabrication of the designed actuator array and testing its performance according to the requirements of DM.
- Study the flexibility of the face sheet mirror which will be used as the reflective layer in the DM.
- Investigating the bonding techniques for attaching the actuator array and the flexible mirror.
- Design and analysis of the performance of an extended tri-electrode actuator. A MEMS moving electrode should be designed such that the springs are not affected by underlying electrostatic forces.
- Fabrication and testing of the designed extended tri-electrode actuator. The tested actuator is not only applicable to array-based applications. The extended controlling range can be used in applications of extended range and in the use of bidirectional control.

Appendices

Appendix A. Tri-electrode models

The tri-electrode actuator was studied using various models. The unit-cell is the most efficient one for studying the topology. However, the actuator was studied using various other models as some are reported here.

Figure A.1 shows the full 2D front view schematic of the tri-electrode topology which was primarily used in the studies. The response curves are plotted for $W_E > W_S$, $W_E = W_S$ and $W_E < W_S$ at the same primary voltages (V_P = 0, 10, 20, 30 V), as illustrated in figures A.2, A.3 and A.4. When the electrode width (W_E) is larger than the gaps (W_S), the response curves do not show a noticeable improvement in voltage reduction. However, the tri-electrode characteristics (described in section 3.4.3) improvements can be seen as the gap spacings are wider. The curves displayed here are not normalized to show how exactly gap spacing affects the background and control voltages.

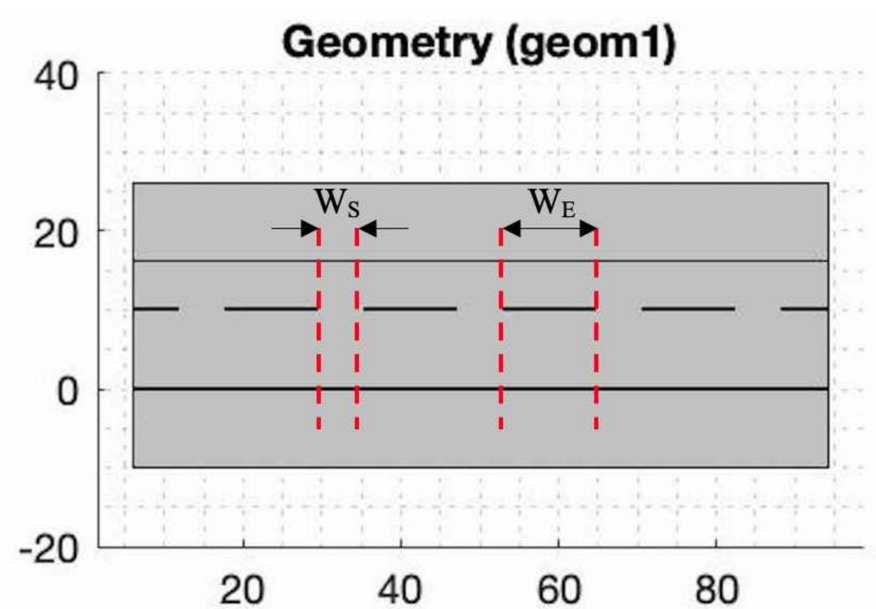

Figure A.1. The 2D schematic of the tri-electrode topology, $W_E > W_S$ (W_E = 2 W_S) and the rest of the dimensions are chosen arbitrarily.

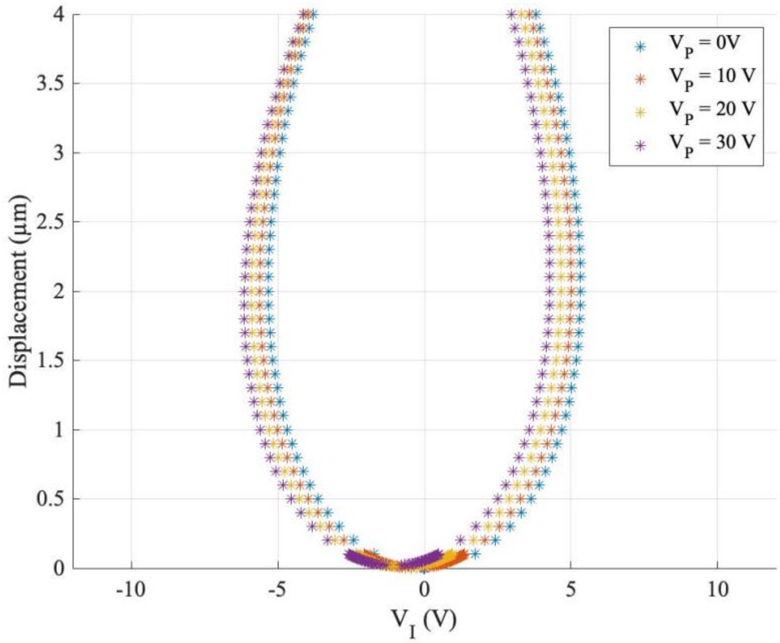

Figure A.2. Tri-electrode response curves for $W_E > W_S$ ($W_E = 2\ W_S$) at V_P = 0, 10, 20, 30 V.

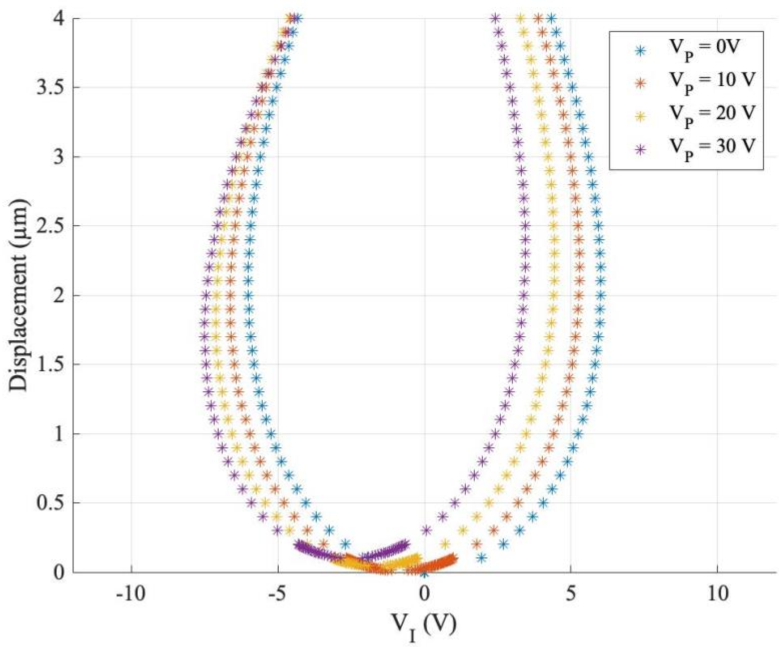

Figure A.3. Tri-electrode response curves for $W_E = W_S$ at V_P = 0, 10, 20, 30 V.

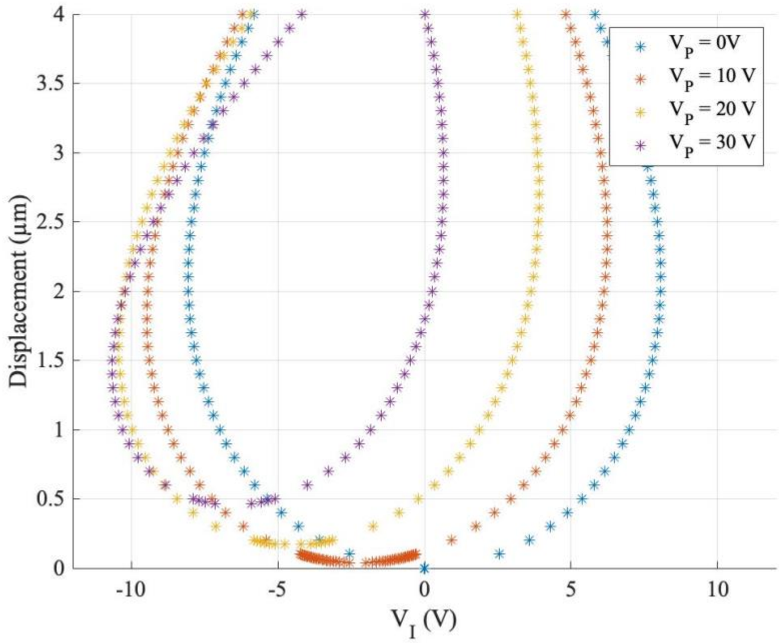

Figure A.4. Tri-electrode response curves for W_E =1/3 W_S at V_P = 0, 10, 20, 30 V.

Another point in modeling the tri-electrode is to place a various number of the electrodes (W_E) at a certain space. Thus, models with the same electrode width (W_E) and a different number of electrodes were studied as one example is displayed in figure A.5.

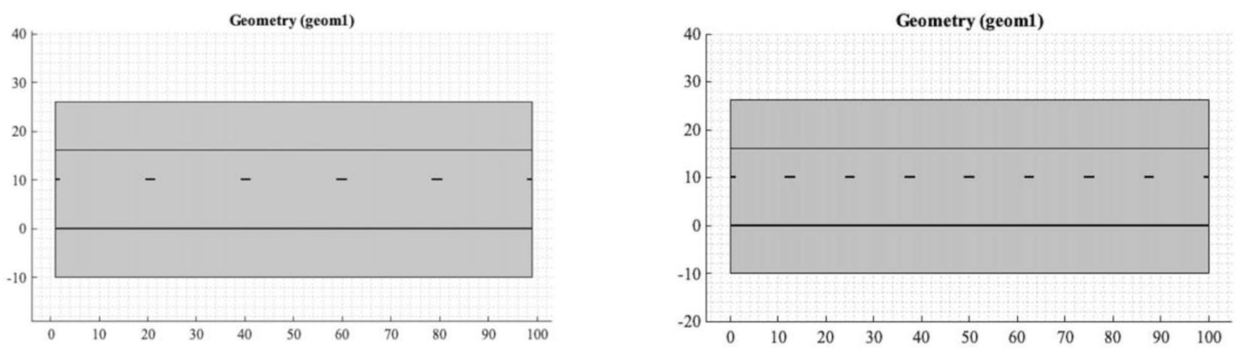

(a) (b)

Figure A.5. 2D schematic of tri-electrode topologies with the same W_E and different W_S with (a) 6 electrodes and (b) 9 electrodes.

The response curves for the tri-electrode configurations are illustrated in figure A.6. The difference between the curves with the same V_P are apparent.

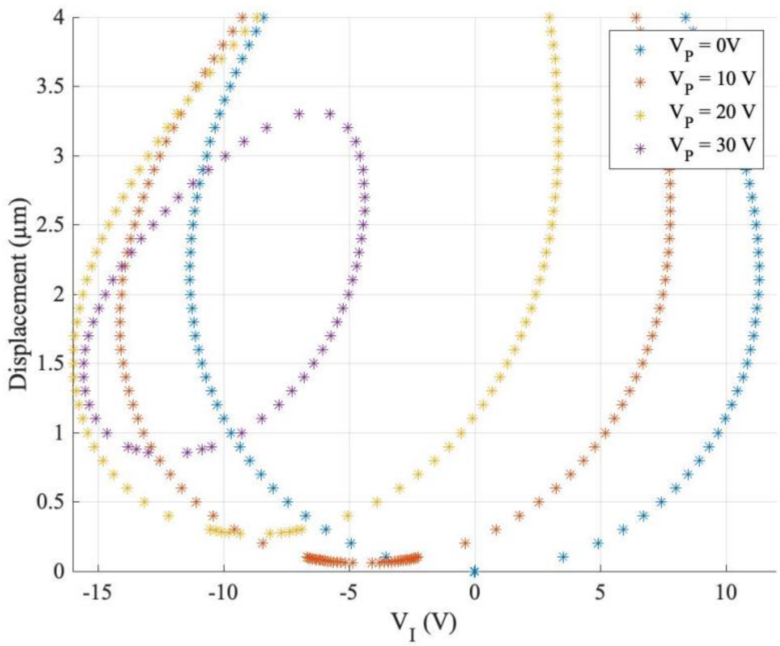

Figure A.6. Tri-electrode response curves at V_P = 0, 10, 20, 30 V, with 6 electrodes.

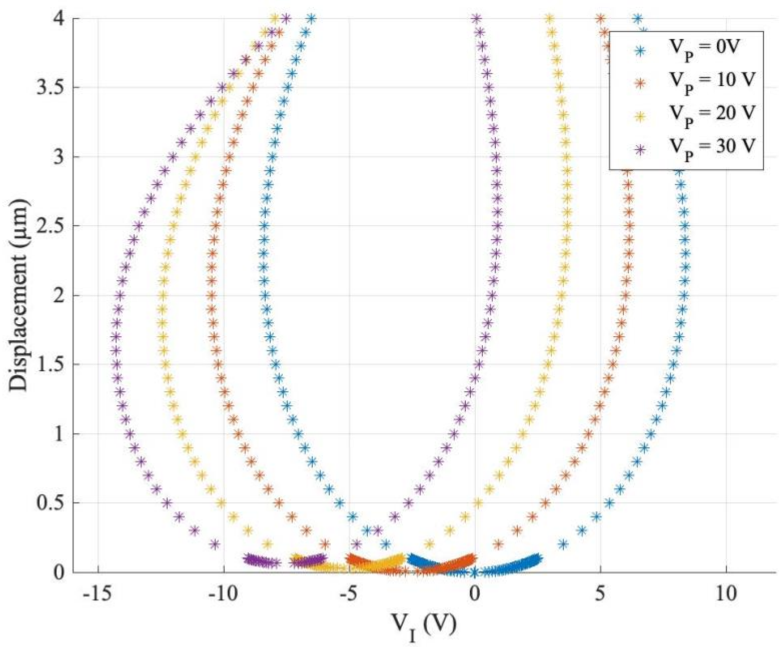

Figure A.7. Tri-electrode response curves at V_P = 0, 10, 20, 30 V, with 9 electrodes.

Similar to the responses reported here, several more simulations were performed, and their response curves were compared. Therefore, it was realized that each of tri-electrode parameters (D_2, W_E, W_S) should be studied independently. To do so, the unit-cell was utilized to study the tri-electrode topology.

Appendix B. MEMS FEM studies

B.1 MEMS electrode – nonlinearity

The above studies are based on a linear spring supporting the MEMS. Therefore, we need to ensure that the springs operate in their linear range. The gap spacing is equal to D_1 which are 120, 140 and 155 µm for different cases (based on the measurements from fabrication). Therefore, for the best-case scenario, the supporting springs should be highly linear at those D_1 values. Figure B.1 shows the electrostatic force vs. displacement for the square MEMS for both FEM simulations and analytical solutions. It can be seen that the supporting springs are highly linear with a nonlinearity error of 0.66%. Even though, the nonlinearity error at the first 180 µm of the displacement is smaller than after traveling 1000 µm, the difference is negligible (from 0.663% to 0.668%).

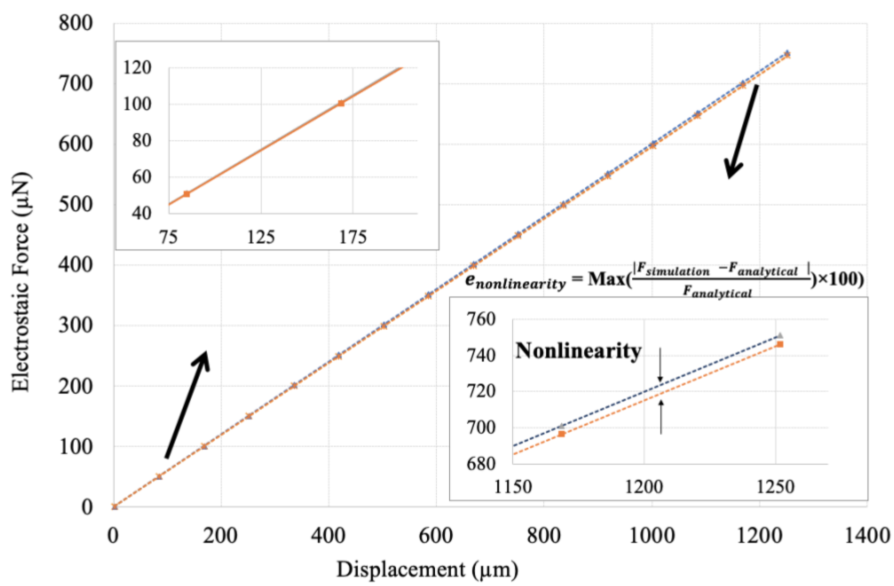

Figure B.1. Force vs. displacement showing the nonlinearity of the square MEMS for 0 – 1200 µm displacement.

B.2 Spring – mesh size

One important parameter in FEM analysis is the mesh sizes uses to solve an equation. Different meshing shapes were tried according to the designed MEMS. However, the larger the mesh the lower the accuracy of the study's results in return of finishing the studies faster. Therefore, to achieve an acceptable error in the simulations, the size of the meshes were refined in several steps and in each step the force was extracted. The change in the value of the force is negligible at sizes smaller than a specific value. Therefore, this is the point mesh refinement was stopped. There is another method using COMSOL called adaptive mech refinement. In this method, the model is solved with one mesh then the error is estimated, then a refined mesh is used, and the model is revaluated, and error is estimated. In this method the most optimum mesh with lowest error can be explored. The mesh refinements in two sample steps are illustrated in figure B.2. The mesh refinement was stopped at a minimum element size of 20 µm, as the calculated electrostatic force does not change meaningfully.

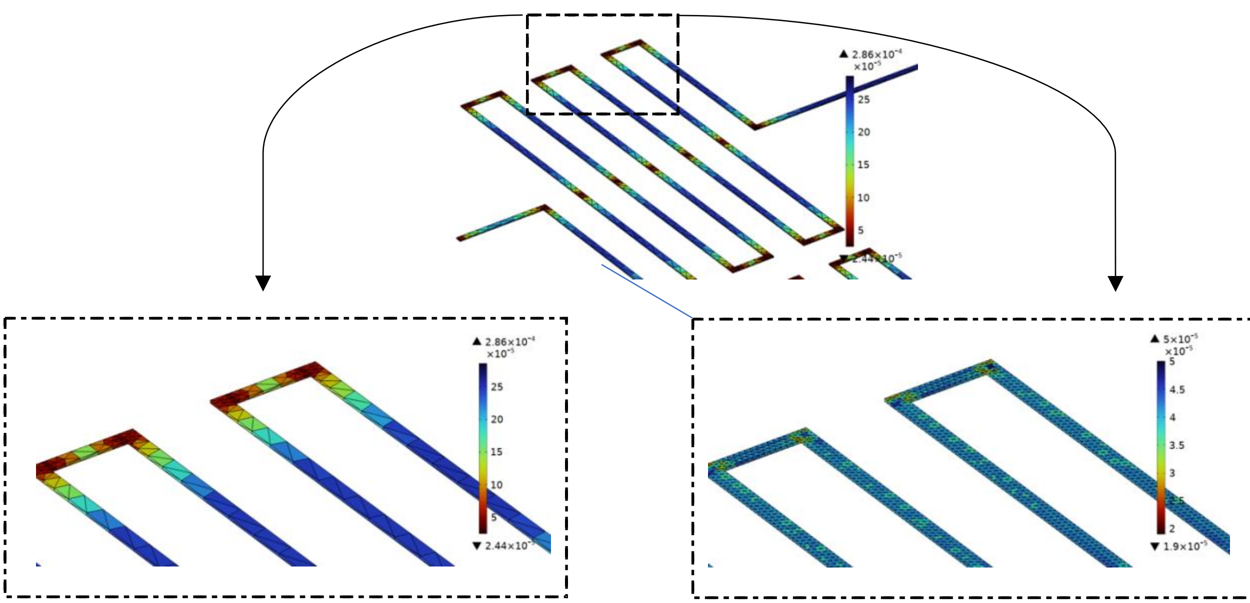

Figure B.2. Meshing of the springs at different mesh and quality sizes. The mesh size with a low quality (left) has the maximum element size of 286 µm while the higher quality mesh has the maximum size of 50 µm.

B.3 MEMS Platform

There is the possibility of bending the MEMS platform if it is relatively thin and wide upon attraction toward the underlaying electrode. Therefore, a series of simulations were performed at a wide range of forces as the bent platforms are shown in figure B.3. In the square MEMS, the platform was bent maximum about 0.3 µm at centers with respect to the corners. This bending is more for the rectangle MEMS as the platform is narrower and the spring is softer. In this case the maximum bending is 0.45 µm. In both cases the bent platform will not affect the actuator performance significantly (below 1 µm and less than the measurement error) as the range of movement is submicron while the actuator should be able to travel at least 40 µm.

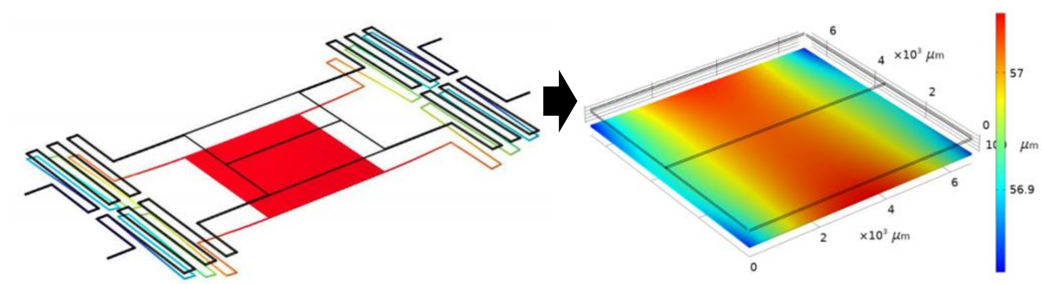

(a)

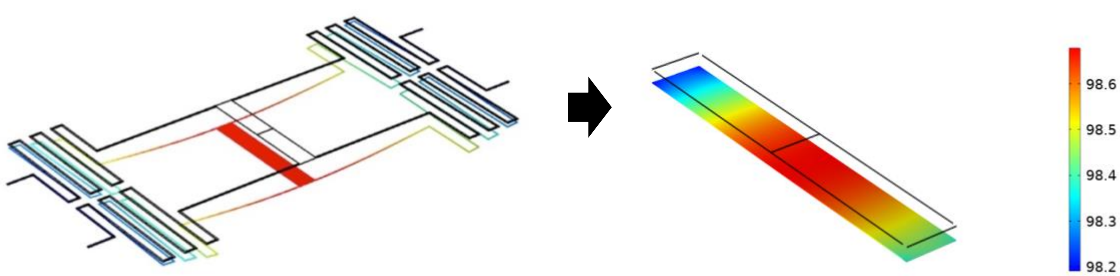

(b)

Figure B.3. The MEMS electrodes bending and moving vertically under the applied force to the platforms. (a) The square MEMS electrode showing the bent platform in right. (b) The rectangular MEMS electrode showing the bent platform in right.

Appendix C. Silicon wafers oxide thickness

The thicknesses of the grown oxides were measured using ellipsometry after unloading from the oxidation furnace. The measured thickness of each wafer is summarized in table C.1. The wafers flipped after each step of oxidations. The entire grown oxide occurred during multiple oxidation steps.

Table C.1. The measured grown thermal oxide on six silicon wafers.

Wafer No.	side	Thickness (nm)	wavelength (nm)	MSE (%)	angle scan
1	1	2623	500-1000	20	60
	2	2690	500-1000	19.3	60
2	1	2694	500-1000	19.9	60
	2	2690	500-1000	19.5	60
3	1	2719	500-1000	20.6	60
	2	2715	500-1000	20	60
4	1	2700	500-1000	21	60
	2	2700	500-1000	22	60
5	1	2646	500-1000	19	60
	2	2651	500-1000	18.8	60
6	1	2517	200-1000	93	60
	2	2510	200-1000	88	60

Appendix D. PETS machine plasma etch rate

Different recipes were tested for the etch rate of silicon in the release step. The recipes and the etch rates are summarized in table D.1.

Table D.1. Five recipes of etching silicon.

	Recipe #1	Recipe #2	Recipe #3	Recipe #4	Recipe #5
Base Pressure (Torr)	0.04	0.02	0.008	0.015	0.015
CF_4 Flow (SCCM)	45	-	-	-	-
CHF_3 Flow (SCCM)	-	-	-	-	-
O_2 Flow (SCCM)	4.5	4.5	9	13.5	-
SF_6 Flow (SCCM)	-	45	45	45	45
Ar Flow (SCCM)	-	-	-	-	-
Work Pressure (Torr)	0.207	0.22	0.2	0.21	0.17
Power (Watt)	100	100	100	100	100
Throttle Angle (%)	75	75	75	75	75
Time (min)	20	20	20	25	20
Thickness (μm)	2	1.6	1.4	1.4	1.3
Etch rate (nm/min)	100	80	70	56	65

The same flow rate of recipe 1 was used in etching HPR 504 and the results are reported in table D.2.

Table D.2. The recipe and the etch rate of PR HPR 504.

	Recipe 1
Base Pressure (Torr)	0.001
CF_4 Flow (SCCM)	45
CHF_3 Flow (SCCM)	-
O_2 Flow (SCCM)	4.4
SF_6 Flow (SCCM)	-
Ar Flow (SCCM)	-
Work Pressure (Torr)	0.156
Power (Watt)	100
Throttle Angle (%)	75
Time (min)	20
Thickness (μm)	1.8
Etch rate (nm/min)	90

References

[1] H. Babcock, “The possibility of compensating astronomical seeing,” Publ. Astron. Soc. Pac., vol. 65, pp. 229–236, 1953.

[2] T. Bifano, “Adaptive imaging: MEMS deformable mirrors,” Nat. Photonics, vol. 5, no. 1, pp. 21–23, Jan. 2011.

[3] J. M. Geary, Introduction to Wavefront Sensors. Bellingham, WA: SPIE, 1995, pp. 22–24, (ISBN 9780819417015).

[4] M. A. Helmbrecht, M. He, C. Kempf, and P. Rhodes, “Scaling up of the Iris AO segmented DM technology for atmospheric correction,” in Proc. 10th Adv. Maui Opt. Space Surveillance Technol. Conf., 2009, p. E72.

[5] T. Bifano, J. Perreault, P. Bierden, and C. Dimas, “Micromachined deformable mirrors for adaptive optics,” in Proc. SPIE Int. Soc. Opt. Eng., 2002, pp. 10–13.

[6] R. K. Tyson, Principles of Adaptive Optics, CRC Press, 3rd edition, 2010.

[7] M. Chen, C. Liu, D. Rui, and H. Xian, “Performance verification of adaptive optics for satellite-to-ground coherent optical communications at large zenith angle,” Opt. Express, vol. 26, no. 4, pp. 4230–4242, Feb. 2018.

[8] Hamelinck, R.F.M.M. Adaptive deformable mirror: based on electromagnetic actuators. PhD thesis Technische Universiteit Einhoven, 2010.

[9] D. J. Schroeder, Astronomical Optics, 2nd ed. New York, NY, USA: Academic Press, 1999, p. 433.

[10] J. D. Mansell, S. Sinha, and R. L. Byer, “Deformable mirror development at Stanford University,” In International Symposium on Optical Science and Technology, Society for Optics and Photonics, 2002, pp 1-12.

[11] P. Weilbacher, “Neptune from the VLT with MUSE/GALACSI Narrow Field Mode adaptive optics,” eso.org. https://www.eso.org/public/images/eso1824a (accessed Nov.30, 2022)

[12] Y. P. Madec, “Overview of deformable mirror technologies for adaptive optics and astronomy,” Proc. SPIE, vol. 8447, Sep. 2012, Art. no. 844705.

[13] T. G. Bifano, J. Perreault, R. K. Mali, and M. N. Horenstein, “Microelectromechanical deformable mirrors,” IEEE J. Sel. Topics Quantum Electron., vol. 5, no. 1, pp. 83–89, Jan./Feb. 1999.

[14] M. A. Helmbrecht, M. He, C. J. Kempf, and P. Rhodes, "The Iris AO S163-X, a 489 actuator, 163-piston/tip/tilt-segment MEMS DM," Proc. SPIE, vol. 7466, 2009, p. 74660E.

[15] M. A. Helmbrecht, M. He, C. Kempf, and P. Rhodes, "Scaling up of the Iris AO segmented DM technology for atmospheric correction," in Proc. 10th Adv. Maui Opt. Space Surveillance Technol. Conf., 2009, p. E72.

[16] M. A. Helmbrecht, M. He, C. J. Kempf, and M. Besse, "MEMS DM development at Iris AO, Inc." in Proc. SPIE 7931, MEMS Adaptive Optics V, vol. 793108, February 14, 2011.

[17] M.A. Helmbrecht, T. Juneau, M. Hart, et al., "Segmented MEMS deformable mirror technology for space applications," On Proc. SPIE, vol.6223, p. 622305, 2006.

[18] M. J. Lin and K. W. Wu, "Design and fabrication of an electrostatically actuated micro deformable focusing mirror," J. Micro/Nanolithogr., J. Microelectromech. Syst., Micro-Opto-Electro-Mech. Syst., vol. 10, no. 1, pp. 011504-1–011504-7, Jan.–Mar. 2011.

[19] E. H. Yang et al., "Design and Fabrication of Electrostatic Actuators with Corrugated Membranes for MEMS Deformable Mirror in Space," SPIE Int'l Symp. on Opt. Sci. & Tech., 2000.

[20] Wang, W., Hu, F., Wang, Q., Qiu, C., Chen, Z. and Yao, J., "A 45-element continuous facesheet surface micromachined deformable mirror for optical aberration correction," AIP Advances, vol. 4, no. 3, p. 31317, 2014.

[21] (OKO technologies, Delft, Netherland). 37 (19) - channel micromachined deformable mirror system: technical passport. Accessed: Dec. 19, 2022. [Online]. Available: http://www.okotech.com/images/pdfs/passport37chMMDM.pdf.

[22] T. Weyrauch, M. A. Vorontsov, T. G. Bifano, A. Tuantranont, V. M. Bright, J. Karpinsky, and J. Hammer, "Performance evaluation of micromachined mirror arrays for adaptive optics," Proc. SPIE, vol. 4124, pp. 32–41, 2000.

[23] S.A. Cornelissen, T.G. Bifano and P.A. Bierden, "MEMS deformable mirror actuators with enhanced reliability," Proc. SPIE, vol. 8253, pp. 47–53, 2012.

[24] Y. Zhou and C. Shafai, "Reduction of Electrostatic Control Voltage with a Tri-Electrode Actuator," In Multidisciplinary Digital Publishing Institute Proceedings, vol. 1, no. 10, p. 282, 2017.

[25] Y. Zhou, C. Shafai, L. Shafai, and G. Burley, "Study of Electrostatic Actuator Voltage Reduction with a Tri-Electrode Actuator with Varying Pull-Down Voltage," In Multidisciplinary Digital Publishing Institute Proceedings, vol. 2, no. 13, p. 928, 2018.

[26] B. Park, E. Afsharipour, D. Chrusch, C. Shafai, D. Andersen and G. Burley, "A low voltage and large stroke Lorentz force continuous deformable polymer mirror for wavefront control," Sensors and Actuators A, pp. 197-204, 2018. https://doi.org/10.1016/j.sna.2018.07.047.

[27] X. Xu, B. Li, Y. Feng, and J. Chu, "Design, fabrication and characterization of a bulk-PZT-actuated MEMS deformable mirror," Journal of Micromechanics and Microengineering, vol. 17, no. 12, pp. 2439-2446, 2007.

[28] P. Lin, H. Hsieh, and G. Su, "Design and fabrication of a large-stroke MEMS deformable mirror for wavefront control," Journal of Optics, vol.13, no. 5, p. 055404, 2011.

[29] HD MicroSystems, Parlin, NJ. PI-2600 Series – Low Stress Applications technical information (2009). Accessed: Dec. 20, 2022. [Online]. Available: https://www.hdmicrosystems.com.

[30] C.-M. Ho and Y.-C. Tai, "Micro-electro-mechanical-systems (MEMS) and fluid flows," *Annu. Rev. Fluid Mech*., vol. 30, no. 1, pp. 579–612, Jan. 1998.

[31] J. W. Judy, "Microelectromechanical systems (MEMS): Fabrication, design and applications," Smart Mater. Struct., vol. 10, pp. 1115–1134, 2001.

[32] D. J. Bell, T. J. Lu, N. A. Fleck, and S. M. Spearing, "MEMS actuators and sensors: Observations on their performance and selection for purpose," J. Micromech. Microeng., vol. 15, no. 7, pp. S153–S164, Jul. 2005.

[33] D. Niarchos, "Magnetic MEMS: Key issues and some applications," Sens. Actuators A., vol. 109, no. 1, pp. 166–173, Dec. 2003.

[34] D. Girbau, A. Lázaro, and L. Pradell, "RF MEMS switches based on the buckle-beam thermal actuator," in Proc. 33rd Eur. Microw. Conf., Oct. 2003, vol. II, pp. 651–654.

[35] H. Sehr, I. Tomlin, B. Huang, S. Beeby, A. Evans, A. Brunnschweiler, G. Ensell, C. Schabmueller, and T. Niblock, "Time constant and lateral resonances of thermal vertical bimorph actuators," J. Micromech. Microeng., vol. 12, no. 4, pp. 410–413, 2002.

[36] F. Ceyssens, S. Sadeghpour, H. Fujita, and R. Puers, "Actuators: Accomplishments, opportunities and challenges," Sens. Actuators A., vol. 295, pp. 604–611, 2019.

[37] H.M. Ouakad, "Simple and accurate analytical solution to the post-buckling response of an electrostatically actuated MEMS curled cantilever," Microsyst. Technol. Vol. 22, pp. 2251–2258, 2016.

[38] M.I. Younis, "Simple and accurate analytical solutions of the electrostatically actuated curled beam problem," Proceedings. ASME Design Eng. Technical Conf. 4, 2014.

[39] I. Morkvenaite-Vilkonciene, V. Bucinskas, J. Subaciute-Zemaitiene, E. Sutinys, D. Virzonis, and A. Dzedzickis, "Development of Electrostatic Microactuators: 5-Year Progress in Modeling, Design, and Applications," Micromachines, vol. 13, no. 8, 2022.

[40] M. Patrascu, J. Gonzalo-Ruiz, M. Goedbloed, S.H. Brongersma, M. Crego-Calama, "Flexible, electrostatic micro fluidic actuators based on thin film fabrication," Sens. Actuators A., vol. 186, pp. 249-256, 2012.

[41] A. Machauf, Y. Nemirovsky, "A membrane micropump electrostatically actuated across the working fluid.," J. Micromech. Microeng. vol. 15, pp. 2309-2316, 2005.

[42] J. J. Yao, "RF MEMS from a device perspective, " J. Micromech. Microeng., vol. 10, pp. R9–R38, Dec. 2000.

[43] Z. J. Yao, S. Chen, S. Eshelman, D. Denniston, and C. Goldsmith, "Micromachined low-loss microwave switches," J. Microelectromech. Syst., vol. 8, no. 2, pp. 129–134, 1999.

[44] R. K. Mali, T. G. Bifano, and M. N. Horenstein, "Development of microelectromechanical deformable mirrors for phase modulation of light," Opt. Eng., vol. 36, no. 2, pp. 542–548, 1997.

[45] E. Thielicke and E. Obermeier, "A fast switching surface micromachined electrostatic relay," in Int. Transducers, Solid-State Sens., Actuators, Microsyst. Conf., 2003, vol. 1, pp. 899–902.

[46] R. R. Mansour, "RF MEMS-CMOS device integration: An overview of the potential for RF researchers," IEEE Microw. Mag., vol. 14, no. 1, pp. 39–56, Jan./Feb. 2013.

[47] J. I. Siddique, R. Deaton, E. Sabo, and J. A. Pelesko, "An experimental investigation of the theory of electrostatic deflections," J. Electrostat., vol. 69, no. 1, pp. 1–6, 2011.

[48] J. I. Seeger and S. B. Crary, "Stabilization of electrostatically actuated mechanical devices," in Proc. Int. Conf. Solid-State Sensors Actuators, 1997, pp. 1–4.

[49] T. Sugimoto, K. Nonaka, and M. N. Horenstein, "Bidirectional electrostatic actuator operated with charge control," J. Microelectromech. Syst., vol. 14, no. 4, pp. 718–724, Aug. 2005.

[50] J. Su, H. Yang, P. Fay, W. Porod, and G. H. Bernstein, “A surface micromachined offset-drive method to extend the electrostatic travel range,” J. Micromech. Microeng., vol. 20, no. 1, Jan. 2010.

[51] M. A. Rosa, D. D. Bruyker, A. R. Völkel, E. Peeters, and J. Dunec, “A novel external electrode configuration for the electrostatic actuation of MEMS based devices,” J. Micromech. Microeng., vol. 14, no. 4, pp. 446–451, Apr. 2004.

[52] E. S. Hung and S. D. Senturia, “Extending the travel range of analog tuned electrostatic actuators,” J. Microelectromech. Syst., vol. 8, no. 4, pp. 497–505, Dec. 1999.

[53] Da-Yong Qiao, Wei-Zheng Yuan, Xiao-Ying Li, “A two-beam method for extending the working range of electrostatic parallel-plate microactuators,” J. Electrostat., Vol. 65, pp. 256-262, 2007.

[54] J. C. Chiou and Y. J. Lin, “A novel large displacement electrostatic actuator: Pre-stress comb-drive actuator,” J. Micromech. Microeng., vol. 15, no. 9, pp. 1641–1648, Sep. 2005.

[55] T. Fukushige, S. Hata, and A. Shimokohbe, “A MEMS conical spring actuator array,” J. Microelectromech. Syst., vol. 14, no. 2, pp. 243–253, Apr. 2005.

[56] S. Braun, J. Oberhammer, and G. Stemme, “Single-chip MEMS 5 × 5 and 20 × 20 double-pole single-throw switch arrays for automating telecommunication networks,” J. Micromech. Microeng., vol. 18, no. 1, p. 015 014, Dec. 1–11, 2007.

[57] Y. Fukuta, Y.-A. Chapuis, Y. Mita, and H. Fujita. “Design, fabrication and control of mems-based actuator arrays for air-flow distributed micromanipulation,” IEEE Journal of Microelectromechanical Systems, 15(4):912–926, 2006.

[58] Arpys Arevalo, David Castro, David Conchouso, Jurgen Kosel, and Ian G. Foulds, “MEMS digital parametric loudspeaker,” In 2016 IEEE 29th International Conference on Micro Electromechanical Systems (MEMS), pages 1098–1101, Shanghai, January 2016. IEEE.

[59] K.-F. Bohringer, B. R. Donald, and N. C. MacDonald, “Single-crystal silicon actuator arrays for micro manipulation tasks,” In IEEE Int. Workshop on Micro Electromechanical Systems, pages 7–12, 1996.

[60] M. Canonica, F. Zamkotsian, P. Lanzoni, W. Noell, and N. de Rooij, “MEMS-based programmable reflective slit mask for multi-object spectroscopy,” MOEMS Miniaturized Syst. X, vol. 7930, p. 79300N, 2011.

[61] S. A. Cornelissen, “4096-element continuous face-sheet MEMS deformable mirror for high-contrast imaging,” J. Micro/Nanolithography, MEMS, MOEMS, vol. 8, no. 3, p. 031308, 2009.

[62] H. Schenk, A. Wolter, U. Dauderstaedt, A. Gehner, and H. Lakner, “Micro-opto-electro-mechanical systems technology and its impact on photonic applications,” Journal of Micro/Nanolithography, MEMS, and MOEMS, vol. 4, pp. 041501-041501-11, 2005.

[63] C. Pollock, L. K. Barrett, P. G. del Corro, A. Stange, T. G. Bifano, and D. J. Bishop, “PWM as a low cost method for the analog control of MEMS devices,” J. Microelectromech. Syst., vol. 28, no. 2, pp. 245–253, Apr. 2019.

[64] C. Pollock et al., “Engineered PWM drives for achieving rapid step and settle times for MEMS actuation,” J. Microelectromech. Syst., vol. 27, no. 3, pp. 513–520, 2018.

[65] S. Dai, R. W. Knepper, and M. Horenstein, “A 300 LDMOS analog multiplexed drive for MEMS devices”, IEEE Trans. Circuits Syst. I, Reg. Papers, vol. 62, no. 12, pp. 2806–2815, Dec. 2015.

[66] COMSOL Multiphysics Reference Manual. 5.5 784–786 [Online]. Available: https://doc.comsol.com/5.5/doc/com.comsol.help.comsol/COMSOL_ReferenceManual. Pdf.

[67] M. Allameh, C. Shafai, “Tri-electrode electrostatic actuator with lower control voltage and high stroke for actuator array implementations,” journal of Electrostatics, vol. 114, p. 103635, 2021.

[68] S.T. Patton, J.S. Zabinski, “Effects of dielectric charging on fundamental forces and reliability in capacitive microelectromechanical systems radio frequency switch contacts,” J. Appl. Phys. vol. 99, pp. 094910, 2006.

[69] K. B. Lee, “Non-contact electrostatic microactuator using slit structures: Theory and a preliminary test,” J. Micromechanics Microengineering, vol. 17, pp.2186–2196, 2007.

[70] J. Su, H. Yang, P. Fay, W. Porod and G.H. Bernstein, “A surface micromachined offset-drive method to extend the electrostatic travel range,” J. Micromechanics Microengineering, vol. 20, pp. 015004, 2010.

[71] M.A. Rosa, D. De Bruyker, A.R. Völkel, E. Peeters and J. Dunec, “A novel external electrode configuration for the electrostatic actuation of MEMS based devices,” J. Micromechanics Microengineering, vol. 14, pp. 446–451, 2004.

[72] M. Allameh, B. Park and C. Shafai, “Enhanced travel range bipolar tri-electrode electrostatic actuator using extended background electrode,” MOEMS and Miniaturized Systems XXI Conf. pp. 120130-120130 ,2022.

[73] M. Allameh, B. Park and C. Shafai, “Performance study of MEMS tri-electrode electrostatic actuator with glass and SU-8 between intermediate and primary electrodes,” MNE euro-sensors conference, Leuven, 2022.

[74] A. V. Narasimha Rao, V. Swarnalatha and P. Pal, “Etching characteristics of Si{110} in 20 wt% KOH with addition of hydroxylamine for the fabrication of bulk micromachined MEMS,” Micro and Nano sys Lett., vol. 5, no. 23, pp. 1-9, 2017. https://doi.org/10.1186/s40486-017-0057-7.

[75] Microchemicals, “WET-CHEMICAL ETCHING OF SILICON AND SIO_2,” Retrieved from https://www.microchemicals.com/technical_information/silicon_etching.pdf.

[76] S. C. Vitkavage, E. A. Irene, H. Massoud,” An investigation of Si-SiO2 interface charges in thermally oxidized (100), (110), (111), and (511) silicon,” J. applied Phys., vol. 68, no. 10, pp. 5262-5272, 1990.

[77] Microchemicals, “Aluminium Etching,” 2013. Retrieved from https://www.microchemicals.com/technical_information/aluminium_etching.pdf.

[78] Y. Zhou, “Investigation of a Micromachined Electric Field Mill to Maximize the Electrostatic Field Sensitivity,” M.Sc dissertation, Dept. Elec. & computer Eng., Uni. of Manitoba, Winnipeg, Manitoba, 2012.

[79] Rui Huang, Christopher M. Stafford and Bryan D. Vogt, “Effect of Surface Properties on Wrinkling of Ultrathin Films”, Journal of Aerospace Engineering, vol. 20, no.1, pp. 38-44, 2007. https://doi.org/10.1061/(ASCE)0893-1321(2007)20:1(38).

[80] P. Flinn, D. Gardner, and W. Nix, “Measurement and interpretation of stress in aluminum-based metallization as a function of thermal history,” IEEE Transactions on Electron Devices, vol. 34, no.3, pp. 689-699, 1987. 10.1109/T-ED.1987.22981.

[81] S. Injeti and R. Annabattula, “Extending Stoney's equation to thin, elastically anisotropic substrates and bilayer films,” Thin Solid Films, vol.598, pp. 252-259, 2016. https://doi.org/10.1016/j.tsf.2015.12.015.

[82] T. Morikaku, Y. Kaibara, M. Inoue, T. Miura, T. Suzuki, F. Oohira, Sh.Inoue, and T. Namazu, “Influences of pretreatment and hard baking on the mechanical reliability of SU-8

microstructures," Journal of Micromechanics and Microengineering, vol. 23, no. 10, p. 105016, 2013. 10.1088/0960-1317/23/10/105016.

[83] S. Chung and S. Park, "Effects of temperature on mechanical properties of SU-8 photoresist material," Journal of Mechanical Science and Technology, vol. 27, no. 9, pp. 2701-2707, 2013. https://doi.org/10.1007/s12206-013-0714-6.

[84] SU-8 Photolithography and Its Impact on Microfluidics, chapter 8. Retrieved from https://www.taylorfrancis.com/books/oa-edit/10.1201/b11188/fabrication-implementation-applications-sushanta-mitra-suman-chakraborty?refId=929114bc-49f3-40ba-87f6-1a5f73f838a4&context=ubx.

[85] Microchem, "SU-8 2000 Permanent Epoxy Negative Photoresist," 5th volume, 2015. Retrieved from https://kayakuam.com.

[86] N. C. LaBianca and J. D, Gelorme, "High-aspect-ratio resist for thick-film applications," Proc. SPIE Symposium on Microlithography, pp. 846-52, 1995. https://doi.org/10.1117/12.210413.

[87] P. Flinn, D. Gardner, and W. Nix, "Measurement and interpretation of stress in aluminum-based metallization as a function of thermal history," IEEE Transactions on Electron Devices, vol. 34, no.3, pp. 689-699, 1987. 10.1109/T-ED.1987.22981.

[88] M. Allameh, S. Ramezanzadehyazdi, B. Park, C. Shafai, "Thermal Stress Analysis and Stabilization of Metal and SU-8 Coatings for Tri-Layer Mirror," IEEE Canadian Conf. on Elec. and Comp. Eng. 2021. 10.1109/CCECE53047.2021.9569127.

[89] B. Park, "Development of a Low Voltage and Large Stroke MEMS-based Lorentz Force Continuous Deformable Polymer Mirror System," Ph.D. dissertation, Dept. Elec. & Computer Eng., Uni. of Manitoba, Winnipeg, Manitoba, 2018.